COHERENT BACKSCATTER AND ITS USE IN MEASURING THE OPTICAL PROPERTIES OF BIOLOGICAL TISSUES.

Miles H. Eddowes, B.A. M.Sc.

Thesis submitted for the Degree of
Doctor of Philosophy (Ph.D)
of the University of London.

Department of Medical Physics and Bioengineering
University College London.

June 1995

ABSTRACT.

This thesis is concerned with the measurement of the scattering and absorption properties of biological tissues using the technique of Coherent Backscatter (also known as Coherent Enhancement or Weak Localization). The Coherent Backscatter method offers a remote sensing technique that may be superior to conventional alternatives through its applicability to *in vivo* measurements, its sensitivity at the relatively high values of scattering often found in biological media, the small volumes of tissue that can be interrogated, and its low equipment costs.

A Monte Carlo approach is used to accurately evaluate the spatial characteristics of light that is backscattered from biological media and an important prediction is made on the likely depth to which the technique probes. The phenomenon of Coherent Backscatter is introduced in the context of tissue optics and the development of a numerical method based on the Monte Carlo results is reported that predicts the coherent enhancement peaks that are likely to be recorded from biological media. This includes accurate predictions of the effects of scattering anisotropy, refractive index mismatches, and certain illumination geometries that have not, as yet, been achieved exactly by any analytical methods. A neural network has been implemented to provide a very fast and robust method for processing an experimental reading in order to extract the reduced scattering and absorption coefficients. The experimental data presented evaluates the accuracy of the technique and demonstrates its use on a variety of media including an *in vivo* human hand. The technique is also used to investigate the possible dependence of the optical properties on the polarization state of the probing light and the orientations of fibres in certain media.

TABLE OF CONTENTS.

CHAPTER 2

CHAPTER 3

CHAPTER 4

CHAPTER 5

CHAPTER 6

CHAPTER 7

LIST OF FIGURES.

LIST OF TABLES.

ACKNOWLEDGEMENTS.

For the day to day running of this project I am indebted to Dr. Tim Mills for his continual friendship, support, and attention to detail, particularly at times when his workload has been so large. Professor Dave Delpy has yet again proved his well deserved reputation of having a seemingly inexhaustible supply of references and scientific knowledge at hand and I am thankful for the many times he helped me from straying down any blind alleys. The guidance I received in the first couple of months from Matthias Essenpreis can not be understated. The treasure trove of papers and Monte Carlo codes proved to be as useful and inspiring as it was initially daunting.

Paul Beard, Mark Cope, Clare Elwell, Mike Firbank, Jem Hebden, Mutsu Hiraoka, Matthias Kohl, Dave Kirkby, Steve Matcher, Martin Schweiger, and Rebecca Simpson have given help with tissue optics matters and contributed in a significant way, as has Gio Buonaccorsi who has always been on hand to enthusiastically offer his assistance with the lasers and subject us to his Scottish humour at times of crisis. The departmental phone directory for the last three years provides a concise list of those additional people who have kept me amused and sane over the last few years. My most personal thanks go to Susan, my parents, and the rest of my family for their support. I must also acknowledge the British taxpayer who, through the Engineering and Physical Science Research Council, have made some contributions towards the expenses incurred during this study.

CHAPTER 1

APPLICATIONS OF LASERS IN MEDICINE.

This chapter gives a brief introduction to the variety of uses that lasers have been put to within clinical medicine. It is interesting to note the timescale over which the rapid development has occurred, particularly compared to the development of a regular surgical technique; the first laser was only demonstrated back in 1960 by T. H. Maiman at the Hughes Research Laboratory. It is all the more remarkable considering the early belief expounded within medicine that the laser was nothing more than a solution looking for a problem.

This chapter is split into two parts discussing the basis of therapeutic and diagnostic applications with a few of the more well known techniques being taken as examples and discussed in greater detail. The chapter concludes with a discussion on the benefits of having accurate measurements for the optical properties when developing therapeutic applications.

1.1 THERAPEUTIC APPLICATIONS.

A rough classification separates laser interaction into four classes of at times dubious distinction; Photochemical, Photothermal, Photomechanical, and Photoablative. General reviews on these topics are available within many texts[1-4]. A 12 part series of highly detailed review articles is currently in press which covers the use of lasers in a variety of surgical disciplines. The areas that have been covered to date are Neurosurgery[5], Otolaryngology[6], Cardiovascular surgery[7], Dermatology[8], and Dentistry[9].

1.1.1 Photochemical.

In photochemical interactions the absorbed photon energy is used to produce a chemical change in certain photo-active compounds. The main example of this phenomenon in medicine is Photodynamic Therapy (PDT)[10] where a photosensitive drug is administered intravenously to a patient with superficial or hollow organ tumours[11]. On illumination by certain wavelengths characteristic of the particular drug[12] (usually red), the photoactivation results in fluorescence and the production of singlet oxygen which acts as a strong toxin and induces cell death. After a period of hours from administration there is often a higher concentration of the drug within tumours compared to healthy tissue. This means that with the additional control of the illumination geometry and timing, selective tumour treatment can be achieved. This selective retention within tumours also enables fluorescence by the photosensitive drug to aid tumour identification. Current research is centred around improving the light dosimetry[13,14], the production of more selective drugs, and the use of drugs which can be activated at more deeply penetrating wavelengths. A very important and often unstated advantage of PDT is that tissues tend to be regenerated rather than replaced with scar tissue.

1.1.2 Photothermal.

In photothermal interactions the photon energy is absorbed directly as heat which creates a temperature rise in the tissue;

1.1.2.1 *Photothermal ablation.*

If there is a high amount of absorption for laser light within a tissue, it is possible to take a reasonably low power laser and deposit all the energy as heat within a very small volume. The result is a high local temperature (up to 1000 °C once the water has boiled off) which will fall off quickly once thermal diffusion dissipates the heat away. The rapid thousand fold expansion of the boiling water within the illuminated volume can rip it apart causing the so called 'laser scalpel effect'. A commonly used laser that produces this effect is the CO_2 laser acting at 10.6 µm where the absorption by water is very high[15] and the effects have been carefully analyzed[16,17].

An alternative to using a CO_2 laser is to take one of the newer solid state lasers operating at one of the other infra-red water absorption peaks (Nd:YAG at 1.44 µm[18], Ho:YAG at 2.1 µm[19-21], and Er:YAG at 2.94 µm[21-23]). The benefit of a more highly absorbed wavelength is that a shallower volume can be treated, whilst a shorter pulse time prevents an appreciable amount of the thermal energy from being lost via conduction before the desired damage is done. Both these effects can reduce the size of the heat-affected zone around the periphery of the cut[24]. The main advantage of these particular wavelengths is that the light can propagate down optical fibres[25] (fused silica fibres with low OH bond density for 2.1 µm and zirconium fluoride fibres for 2.94 µm), unlike the 10.6 µm CO_2 laser which is guided to the target via mirrors mounted on cumbersome and expensive articulated arms.

An example of photothermal ablation is the minimally invasive technique of Laser Angioplasty. The conventional angioplasty technique used to treat arterial occlusions involves passing balloon catheters up from a small arterial incision to the blockage site and then inflating the balloon to stretch the surrounding wall of the vessel. A variation on this technique is to thermally ablate the obstruction with a laser operating at for example 249 nm (KrF, but see next section on photoablation), 308 nm (XeCl)[26] or 1064 nm (Nd:YAG). The success of laser angioplasty has been placed in doubt by statistics from clinical trials[27] which identify accidental perforation of the arterial wall and restenosis as being significant problems. More recent experiments have suggested that the effects of restenosis following angioplasty could be offset by treating the site with PDT[28,29].

1.1.2.2 *Coagulation.*

Some thermal effects on protein structures cause the original long strands of polypeptides to tangle up as globules. As well as causing irreparable cell damage, this can produce a shrinkage of the collagen which in vascular tissue tends to induce haemostasis. This explains the use of the ancient technique of hot iron cautery as well as its modern equivalents which within the realms of laser medicine includes the widespread use of the Nd:YAG laser. The applications of this laser coupled with fibre optic delivery systems are numerous and often the preferred treatment for gastrointestinal bleeding[30] and tumour palliation eg. within the bronchus[31], oesophagus[32], colon[33] and rectum. These minimal invasive procedures have the advantage over scalpel surgery of limited structural/cosmetic damage, with reduced amounts of blood loss, reduced needs for anaesthesia, a much quicker recovery time and hence lower treatment costs[34].

The use of the low power Nd:YAG 1064 nm laser, and its recent rival the high power laser diode, can be used to deliver heat energy for treating tumours in solid organs, e.g. within the breast and liver[35-38], and also conditions such as benign prostatic hyperplasia[39]. The gentle heating effect damages the cell structures which can eventually produce cell death. The subsequent necrosis, sloughing, and replacement by scar tissue results in a minimal amount of cosmetic/structural damage[40], as well as reduced patient trauma. If any charring effects can be avoided then a possible cause of post operative cysts is also eliminated.

Photo-induced thermal coagulation has, since the pioneering work of Meyer-Schwickerath[41] on detached retinas, become a first choice treatment for many conditions[42] within Ophthalmology, e.g retinal detachment, macular degeneration, and proliferative diabetic retinopathy.

All humans suffer to some degree from imperfections in the shape of the cornea and eye ball which results in a refractive error of the eye. In most cases it is possible to provide sufficient corrective compensation by placing external lenses in the line of sight e.g spectacles or contact lenses. A modern alternative to using compensation lenses is to correct the imperfections themselves by reshaping the corneal surface with a computer controlled ArF excimer laser (193 nm); Photorefractive Keratectomy[43,44]. At this wavelength it is now generally agreed that the cutting action is performed by a photothermal process where the intermolecular bonds are shaken apart by the intense heat, rather than being bombarded with photons with sufficient energies to part the bonds directly (photoablative)[45]. The correction obtained can either obviate the need to wear the spectacles or contact lenses, or significantly reduce the task external correction lenses need to do. Despite recent worries over the instability of the laser optics used[46] and the long term effects[43,44], it has found regular use in the treatment of myopia[47,48]. Additional research is currently being conducted with masks to try and improve the performance in correcting for other conditions such as astigmatism and hyperopia[49]. An alternative to the excimer lasers is the use of the Ho:YAG[50] laser which deforms the corneal surface via the tissue shrinkage effect induced by heating (Laser Thermokeratoplasty)[43].

One of the most common uses of lasers in medicine is for the cosmetic treatment of Port Wine Stains (dermal vascular lesions). The wavelength of light used is matched to be selectively absorbed by the blood in the vessels which then allows the deposited heat to thermally damage the vessel walls. A wide selection of papers[51-55] have been published in this field with the result that standard routines have emerged for optimal treatments[56] (585 nm, 0.5 msec flashlamp pumped dye laser). Recent work on this area has involved extensive Monte Carlo modelling of the light transport around the capillary network and the subsequent heat transport. This has allowed recent treatments to include the use of a pulsed cryogen jet which is applied to the surface of the skin just prior to the laser irradiation. The result is a cooling thermal wave front which propagates into the skin at the same time as the heating wave front generated within the capillaries travels out towards the surface. The result is a reduction in the temperature of the superficial dermal layers thus allowing larger laser powers to be used[57]. It is interesting to note the benefit this development obtained from the theoretical studies which were subsequently put into practice[58,59].

As explained earlier, it is possible to alter the structures of proteins through thermal denaturation. This means that if two collagen fibres are in contact with each other during heating it is feasible to get them to fuse together in a manner termed as Tissue Welding. The resulting connection can then be reinforced with scar tissue during the healing process. This is sometimes performed on arterial walls with Ar^{+1} lasers operating at 480 or 514 nm, CO_2 at 10.6 μm, or Nd:YAG at 1064 nm[60,61].

1.1.2.3 *Photoablation.*

Photoablation is a debatable regime where it is believed that the bombarding photons have an energy that is sufficient to directly part the intramolecular bonds without using a thermal action. It has been suggested that this mechanism is present when using a ArF (193 nm) or KrF (249 nm) laser in Photorefractive Keratectomy or Laser Angioplasty respectively. However, the exact differences between photo-thermal ablation and photoablation are very difficult to distinguish experimentally.

1.1.2.4 *Photomechanical.*

In photomechanical interactions the photon energy is indirectly transferred to acoustic waves via a thermal expansion or the formation of a plasma bubble. A recent and financially rewarding procedure has been the blanching of tattoos. A variety of techniques have been tried for this of which the most successful has been using a Q-switch ruby laser. The particular wavelength of the light is selectively absorbed by the tattoo pigments and the light intensity and pulse duration optimised to create fragmenting shockwaves. The standard body response of scavenging the foreign particles by macrophages is then exploited to remove the small pigmented fragments leaving negligible amounts of scar tissue behind[62].

When short intense laser pulses, such as from Q-switched Nd:YAG lasers or flashlamp dye lasers, are fired at a target, optical breakdown may be achieved on the surface which results in a plasma formation. If the target is a stone and the wavelength optimally chosen to produce the desired effect, an intense shock wave can be generated which propagates through the stone with a destructive force. The resulting fragmentation is called Laser Lithotripsy. Removal of these fragments can then be achieved without external incisions by purging the cavity with water or by using the conventional body fluid flows. For cases such as ureteral stones[63] the method has been as successful as the standard extracorporeal lithotripsy technique of generating acoustic waves outside of the body and then focusing them down onto the target. The big advantage of using the optical method is its ability to select the target accurately with a minimal amount of surgery[64-67].

1.2 DIAGNOSTIC APPLICATIONS.

1.2.1 Blood flow.

The phenomenon of doppler shifting where the apparent wavelength of a wave is dependent on the relative velocities of the emitter, the detector and the interacting particles was first shown to exist for photons bouncing off red blood cells by Stern in 1975[68]. Since then many commercial instruments have been developed for monitoring blood flow velocities in skin non-invasively, or in deeper channels via implanted probes.

1.2.2 Imaging.

The desire to produce relatively cheap techniques to give tomographical information without using harmful ionising radiation dosages is very strong (Magnetic Resonance Imaging may have a high resolution performance but is not cheap). Two particular applications would be for tumour detection in breasts, and brain imaging. The techniques involve measuring the attenuation spectrum and path length distribution for deep penetrating infrared light within a scattering medium, and then interpreting the data recorded at several positions for several photon launching sites, as an image. The latter problem of producing an image reconstruction routine with acceptable performance for a scattering medium is far from trivial[69-74].

1.2.3 Oximetry.

The fact that haemoglobin and oxy-haemoglobin have different optical absorption spectra has been known from the general visual appearance of arterial and venous blood since medicine first started. The first attempt to use this property to measure the degree of oxygenation in blood was by Nicolai in 1932 with his experiments on the optical transmission through a hand. Since then it has had a significant impact on the science of oxygen monitoring[75]. The realisation that a pulsatile component within a transmission recording of light propagating through tissue is likely to be the result of the fluctuating volume of blood found mainly in the arteries, led directly to the development of Pulse Oximetry[76]. This technique, which can only measure the ratio between the oxygenated and deoxygenated haemoglobin concentrations, has since become a widespread requirement for most intensive therapy units and surgical procedures requiring anaesthesia.

If more of the spectrum is analyzed than the standard two wavelengths used in pulse oximetry, it is possible to determine the relative concentrations of oxidised cytochrome aa_3 as well as the two haemoglobin states[77-79] (cytochrome aa_3

is an enzyme used in the respiratory chain, its concentration is indicative of the oxygen utilisation that is going on in cell metabolism). It is possible to determine from transient information, data such as cerebral blood volume[80] and cerebral blood flow[81], whilst direct knowledge of the optical path lengths taken by the photons yields quantitative information on concentration changes.

1.2.4 Photoacoustic spectroscopy.

The pattern of thermal energy deposited by a laser pulse is characteristic of the optical parameters of the tissue. This in turn affects the shape of the induced acoustic wave according to the composition and geometry of the target tissue. Analysis of an acoustic wave generated by a short laser pulse in a biological medium can therefore yield anatomical information of clinical importance. Applications include the identification of arterial blockages prior to laser angioplasty[82,83] and the monitoring of blood glucose levels[84-86].

1.3 THE ROLE OF PHYSICS IN PREDICTING LASER TREATMENTS.

The modelling of laser treatments such as interstitial laser photocoagulation and photodynamic therapy are all based on an accurate knowledge of the physical properties of the biological media concerned. For photothermal ablative[4] mechanisms the models are relatively straightforward for the initial stages. The thermal energy from the laser is deposited in a volume defined by the illuminated spot size and the depth of light penetration which is in turn almost exclusively dependent on the high absorption coefficient found at the wavelengths normally used (ultra violet or far infra red > 2 μm)[2]. From here the problem increases in complexity as it involves knowledge of the thermal properties of charred tissues and the mechanisms involving the removal of the destroyed tissue which is often

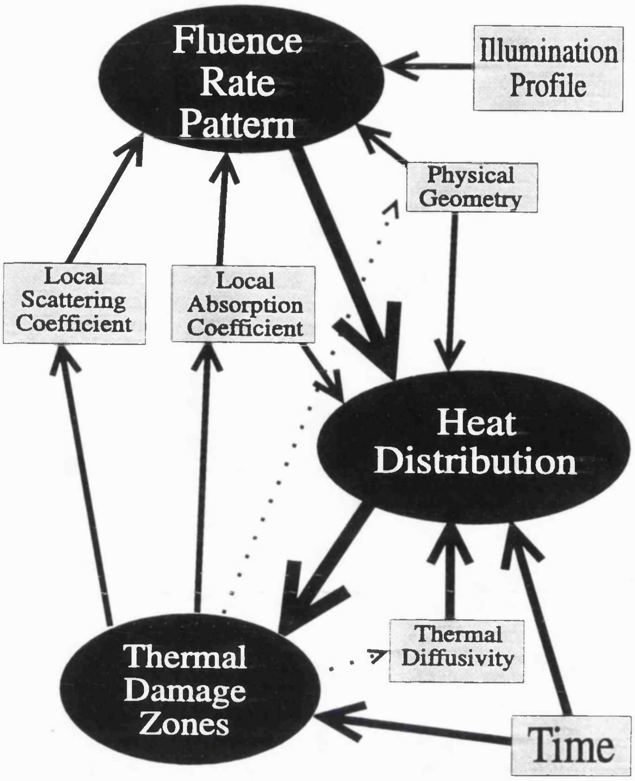

Figure **1.1** Flow diagram showing the interplay of processes involved with laser coagulation.

a propulsion effect from boiling water. Without accurate measurements of these properties it is difficult to make any prediction as to the degree of peripheral heat damage which is so often of interest.

When dealing with more deeply penetrating light, the important optical properties are the reduced scattering and absorption coefficients. For coagulating treatments the issue is complicated by the fact that there are large changes in these coefficients as the treatment progresses and the protein denatures[87]. This is in addition to a general temperature dependence of the absorption coefficient in water which is discussed later in the review of optical properties (chapter 3, section 2.1). It is also necessary to have accurate details on the thermal properties of the medium. This includes the heat transport methods which in the presence of blood perfusion[88] vary according to the degree of haemostasis induced by the treatment. A simple model of this is contained within the bio-heat equation[89,90].

Once the model of heat flow has been predicted[91], the zones of thermal damage and cell death may be deduced using a rate process theory[87,92]. The flow diagram in fig. 1.1 shows the interplay between the different variables involved in the overall modelling of the fluence rate and includes the weaker associations that may be present such as between the degree of damage and its effects on the thermal properties and physical geometries (the tissue shrinks on coagulation). An attempt has been made to provide a time dependent model for laser coagulation of the prostate which incorporates some of the more elemental processes outlined here[93].

CHAPTER 2

LIGHT TRANSPORT THEORY.

This chapter sets out the conventions used in this thesis placing emphasis only on those areas of particular interest, i.e the use of near infra-red (NIR) light when applied for therapeutic (thermal) use, or for diagnostic purposes when limited to the measurements of elastic scattering or absorption parameters.

2.1 ABSORPTION.

Absorption is the effective termination of a photon's propagation; energy is transferred to states other than that of light. The amount of absorption is determined by the particular molecules or groups of atoms within the molecules known as chromophores. Each chromophore is sensitive to particular wavelength bands which are in turn influenced by the surrounding environment; e.g. temperature, pH, and neighbouring molecules. The absorption parameter is a global measure representing the average conditions a photon can expect to encounter.

If the medium is an absorbing, homogenous non-scatterer, then light transport can be fully described by the Lambert-Bouguer law;

$$\frac{I_{out}}{I_{in}} = e^{-\mu_a d} \tag{2.1}$$

Where μ_a is the ***absorption coefficient*** and ***d*** the depth into the medium. The inverse of this coefficient is the ***absorption length***, l_a, or the depth for the signal to be attenuated by *e*. The ***specific absorption coefficient***, α, (mm^{-1} $mmol^{-1}$) is the absorption coefficient per unit of concentration in Molar and the ***Absorbance***, ***A***, or ***Optical Density, OD,*** the logarithmic ratio;

$$OD = \log_{10}\frac{I_{in}}{I_{out}} \tag{2.2}$$

If the medium is heterogenous, with time variant concentrations c_i, the overall absorption coefficient is written as;

$$\mu_a = \sum_i \alpha_i(\lambda)c_i(r,t) \tag{2.3}$$

where the parameters ***r*** and ***t*** specify the position in space and time respectively.

2.2 SINGLE SCATTERING.

The alteration of a photon's direction is termed a scattering event. There are two types of scattering, elastic and inelastic, differentiated by the possibility of the photon's energy being altered.

2.2.1 Inelastic Scattering.

This energy-altering case encompasses amongst others fluorescence, phosphorescence, Raman scattering and Brillouin scattering. They can all be considered to have a negligible effect on the overall fluence rate at IR wavelengths[94-96] and are thus given no further consideration here.

2.2.2 Elastic Scattering.

This dominant case is given an extensive treatment in many texts including Bohren and Huffman 1983[97] and summarised here for completeness.

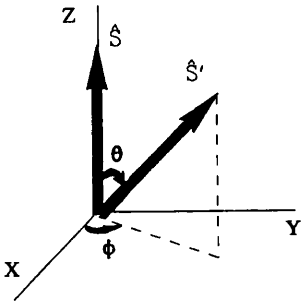

Figure **2.1** Coordinate system for scattering theory.

In fig. 2.1, the photon following path $\hat{s}$ is scattered into direction $\hat{s}'$. The probability function describing the angle between these two directions is given by the differential scattering cross-section;

$$\frac{d\sigma(\hat{s},\hat{s}')}{d\hat{s}} = r^2 \frac{I_s(\hat{s}')}{I_{in}(\hat{s})} \tag{2.4}$$

Where $d\hat{s}' = \sin\theta . d\theta . d\phi$ and r is the distance from scattering centre to the observer. The integral of this expression over all angles is termed the ***total scattering cross-section***;

$$\sigma_s = \int_{4\pi} \frac{d\sigma}{d\hat{s}} d\hat{s} \qquad (2.5)$$

The differential cross-section term in this equation may be replaced by the term $\sigma_s f(\hat{s},\hat{s}')$, where $f(\hat{s},\hat{s}')$ is the normalised ***single scattering phase function***. If all the scattering centres are identical in effect and evenly distributed throughout the medium with a particle density of ρ then the ***scattering coefficient*** is;

$$\mu_s = \rho \sigma_s \qquad (2.6)$$

The total scattering coefficient used for a mixture of multiple scattering types is a simple extension;

$$\mu_s = \sum_i \rho_i \sigma_{si} \qquad (2.7)$$

whilst the equivalent for the phase function produces the ***average single scattering phase function***;

$$f_{mean}(\hat{s},\hat{s}') = \frac{\sum_i \rho_i(r,t)\sigma_{si}(\lambda) f_i(\hat{s},\hat{s}')}{\sum_i \rho_i(r,t)\sigma_{si}(\lambda)} \qquad (2.8)$$

If we define θ as being the angle between incident and scattered light and $\upsilon = \hat{s}.\hat{s}' = \cos\theta$ then within the spherically symmetric case we have the relationship $f_{mean}(\hat{s},\hat{s}') = f(\lambda,r,t,\hat{s},\hat{s}') = f(\lambda,r,t,\upsilon)$. A single parameter used to quantify the directionality of scattering is the first moment of this equation; the ***mean cosine of the angle***, or the ***anisotropy factor, g;***

$$g = 2\pi \int_{-1}^{1} \upsilon f(\upsilon) d\upsilon, \qquad \upsilon = \cos\theta \qquad (2.9)$$

This coefficient is +1 when the scattering is totally forward, -1 when totally backward, and zero when isotropic. A relatively simple approximation to the scattering phase function for Mie scatterers is the popular Henyey-Greenstein[98] phase function shown as;

$$p(\upsilon) = \frac{1 - g^2}{4\pi\,(1 + g^2 - 2g\upsilon)^{\frac{3}{2}}} \tag{2.10}$$

g can be used in the so called ***reduced scattering coefficient***, ***modified scattering coefficient***, or the ***transport scattering coefficient***, μ'_s, used to express the distance over which a multiple of anisotropic ($g \neq 0$) scattering events has the equivalent effect as a single isotropic event;

$$\mu_s' = \mu_s(1-g) \tag{2.11}$$

It is possible to combine the absorption and scattering parameters to give transport parameters such as the ***extinction coefficient*** or ***total attenuation coefficient***, μ_t;

$$\mu_t = \mu_s + \mu_a \tag{2.12}$$

or the ***transport coefficient***, μ'_t;

$$\mu_t' = \mu_s' + \mu_a \tag{2.13}$$

These parameters should not be confused with the ***effective attenuation coefficient***, μ_{eff}, and its inverse the ***effective penetration depth***, δ, applicable only to diffuse light and derived from the so-called diffusion theory;

$$\delta = \frac{1}{\mu_{eff}} = \frac{1}{\sqrt{3\mu_a(\mu_a+\mu_s(1-g))}} \tag{2.14}$$

The ratio of the scattering coefficient to the extinction coefficient is termed the **albedo**, *a*;

$$a = \frac{\mu_s}{\mu_s + \mu_a} = \frac{\mu_s}{\mu_t} \tag{2.15}$$

whereas the **reduced albedo** takes the form;

$$a' = \frac{\mu_s'}{\mu_s' + \mu_a} = \frac{\mu_s'}{\mu_t'} \tag{2.16}$$

The inverses of the coefficients are the photon mean free paths defined as;

The ***absorption mean free path***;

$$l_a = 1/\mu_a \tag{2.17}$$

The ***scattering mean free path***;

$$l_s = 1/\mu_s \tag{2.18}$$

The ***reduced scattering mean free path***;

$$l_s' = 1/\mu_s' \tag{2.19}$$

The ***extinction mean free path***;

$$l_t = 1/\mu_t \tag{2.20}$$

The ***transport mean free path***;

$$l_t' = 1/\mu_t' \tag{2.21}$$

The ***scattering efficiency,*** Q_{SCA} is defined as the ratio between the scattering cross section and the area of a disk with the same radius as the scattering particle;

$$Q_{SCA} = \frac{\sigma_s}{\pi a^2} \tag{2.22}$$

where $\boldsymbol{a}$ is the particle radius.

Terminology for the Stokes parameters follows that of Bohren and Huffman[97];

$$\begin{aligned} I &= \langle E_{\|}^2 + E_{\perp}^2 \rangle \\ Q &= \langle E_{\|}^2 - E_{\perp}^2 \rangle \\ U &= \langle 2E_{\|}E_{\perp}\cos(\delta) \rangle \\ V &= \langle 2E_{\|}E_{\perp}\sin(\delta) \rangle \end{aligned} \tag{2.23}$$

where $\boldsymbol{E}_{\|}$ is the electric field in the observation plane whilst the component perpendicular to it is $\boldsymbol{E}_{\perp}$ delayed by a phase shift of δ. As can be seen from the above equations, $\boldsymbol{I}$ is the total intensity, $\boldsymbol{Q}$ the measure of polarization along 0° or 90° lines, $\boldsymbol{U}$ of polarization along -45 ° or +45° lines, and $\boldsymbol{V}$ of circular polarization. The ***Degree of Polarization*** is defined as;

$$P = \sqrt{\frac{Q^2 + U^2 + V^2}{I^2}} \tag{2.24}$$

Meuller ~~amplitude~~ scattering matrices are often used to express the relationship between the Stokes vectors of incident and scattered light;

$$\begin{pmatrix} I_s \\ Q_s \\ U_s \\ V_s \end{pmatrix} = \frac{1}{k^2r^2} \begin{pmatrix} S_{11} & \cdots & S_{14} \\ S_{21} & \cdots & S_{24} \\ S_{31} & \cdots & S_{34} \\ S_{41} & \cdots & S_{44} \end{pmatrix} \begin{pmatrix} I_i \\ Q_i \\ U_i \\ V_i \end{pmatrix} \tag{2.25}$$

Here the distance between observer and the scattering centre is defined as $\boldsymbol{r}$ and the ***wave number,*** $k = 2\pi n/\lambda$, where $\boldsymbol{n}$ is the refractive index of the medium.

The scattering of interest can be split into two categories; Rayleigh and Mie, depending on the relative size of the scatterers to the wavelength.

Rayleigh Scattering.

This is in theory applicable to particles of any shape with a dimension comparable to or smaller than the wavelength of the light. In the case of spherical particles it is possible to write the Mueller Matrices as[99];

$$\begin{pmatrix} I_s \\ Q_s \\ U_s \\ V_s \end{pmatrix} = \frac{8\pi^4 N a^6}{r^2\lambda^4} \begin{pmatrix} (1+\cos^2\theta) & (\cos^2\theta-1) & 0 & 0 \\ (\cos^2\theta-1) & (\cos^2\theta+1) & 0 & 0 \\ 0 & 0 & \cos\theta & 0 \\ 0 & 0 & 0 & \cos\theta \end{pmatrix} \begin{pmatrix} I_2 \\ Q_2 \\ U_2 \\ V_2 \end{pmatrix} \left|\frac{m^2-1}{m^2+2}\right|^2 \qquad (2.26)$$

where N is the particle density, $\boldsymbol{a}$ the particle radius, and $\boldsymbol{m}$ the refractive index of the scatterer.

The three general points that can be made about Rayleigh scattering for all shapes of particles are;

i) The scattering is almost isotropic.

ii) There is a strong dependence for the scattering cross section on $1/\lambda^4$.

iii) The scattering efficiency is << 1.

Mie scattering.

The solving of Maxwell's equations for perfect spheres was first attributed to Gustav Mie in 1908. This gave, using the same terminology as for Rayleigh scattering, the result[97];

$$\begin{pmatrix} E_{\parallel s} \\ E_{\perp s} \end{pmatrix} = \frac{e^{ikr}}{-ikr} \begin{pmatrix} S_2 & 0 \\ 0 & S_1 \end{pmatrix} \begin{pmatrix} E_{\parallel i} \\ E_{\perp i} \end{pmatrix} \qquad (2.27)$$

where the two-by-two ***amplitude scattering matrix*** has components;

$$S_1(\theta) = \sum_{n=1}^{\infty} \frac{2n+1}{n(n+1)}(a_n\pi_n + b_n\tau_n) \tag{2.28}$$

$$S_2(\theta) = \sum_{n=1}^{\infty} \frac{2n+1}{n(n+1)}(a_n\tau_n + b_n\pi_n) \tag{2.29}$$

and a_n and b_n are coefficients dependent on the size of the particle, its relative refractive index and the wavelength. The other terms are defined with Legendre polynomials P_n^m;

$$\pi_n = \frac{P_n^1}{\sin\theta}, \qquad \tau_n = \frac{dP_n^1}{d\theta} \tag{2.30}$$

This leads to the Mueller scattering matrix;

$$\begin{pmatrix} I_s \\ Q_s \\ U_s \\ V_s \end{pmatrix} = \frac{1}{k^2r^2} \begin{pmatrix} S_{11} & S_{12} & 0 & 0 \\ S_{12} & S_{11} & 0 & 0 \\ 0 & 0 & S_{33} & S_{34} \\ 0 & 0 & S_{34} & \underset{33}{S_{\cancel{44}}} \end{pmatrix} \begin{pmatrix} I_i \\ Q_i \\ U_i \\ V_i \end{pmatrix} \tag{2.31}$$

where

$$S_{11} = \frac{1}{2}(|S_2|^2 + |S_1|^2) \qquad S_{12} = \frac{1}{2}(|S_2|^2 - |S_1|^2)$$

$$S_{33} = \frac{1}{2}(S_2^*S_1 + S_2S_1^*) \qquad S_{34} = \frac{1}{2}(S_2^*S_1 - S_2S_1^*) \tag{2.32}$$

These equations form a powerful tool which can be used to predict the scattering performance for spheres with dimensions larger than the wavelength of the light. Interesting features are summarised below;

i) Unpolarized light is slightly polarized by the interactions.

ii) The angular distribution of scattered photons is forward peaked with an oscillating feature resulting from superimposed interference effects, and then a slight increase directly in the back scatter direction.

iii) The anisotropy factor approaches unity (highly forward) as the particle gets larger.

iv) The differential scattering cross-section shows little variation with wavelength but a large dependence on the dimensions; small particles give small cross-sections, whilst big particles present large cross-sections.

v) Scattering efficiency drops dramatically as the particle size falls (N.B. Rayleigh scattering can then become dominant).

Non-spherical particles.

An exceedingly large variety of approximations is available to predict the scattering behaviour of non-spherical particles (one such example[100]), but none can be exact. Although much effort has gone into testing the approximations, it can be proved that the only valid results are for those shapes close to spheres[101].

The following points form a summary of the differences arising from the scatterer not being a perfect sphere[102];

i) For large particles, the behaviour is similar to spheres of an equal surface area.

ii) With non-polarized light there is less of an angular dependence for light scattered backwards.

iii) All differences get less with increasing absorption in the surrounding medium.

iv) For small randomly oriented particles the average scattering coefficient can be obtained by averaging the individual contributions.

2.3 PHOTON BEHAVIOUR FOR MULTIPLE SCATTERING EVENTS.

From a theoretical point of view there are many possible ways of producing exact solutions for the optical coefficients used to describe multiply scattered photon behaviour. None of them, however, are feasible due to the excessive amount of information required on the scattering structure and the computer power needed to process it. A practical model is that of Radiative Transfer (for review see Patterson *et al.*[103]).

2.3.1 Equation of radiative transfer.

Consider the elemental volume shown in fig. 2.2. An incident beam radiance, $L(r,\hat{s})$, is attenuated by the total attenuation coefficient, μ_t , over the infinitesimal length **ds**;

$$dL(r,\hat{s}) = -\mu_t L(r,\hat{s})ds \qquad (2.33)$$

Adding on the source term, $S(r,\hat{s})$, and the contribution of light scattered from all directions $\hat{s}'$ onto $\hat{s}$ according to the spatial phase function we get;

$$dL(r,\hat{s}) = -\mu_t L(r,\hat{s})ds + \int_{4\pi} d\mu_s(r,\hat{s}',\hat{s})d\Omega' L(r,\hat{s}')ds + S(r,\hat{s})ds \qquad (2.34)$$

There is no general analytical solution to this equation, and most of the approximate solutions postulated[98,104-107] tend to fail somewhere under the complicated boundary conditions found within tissues.

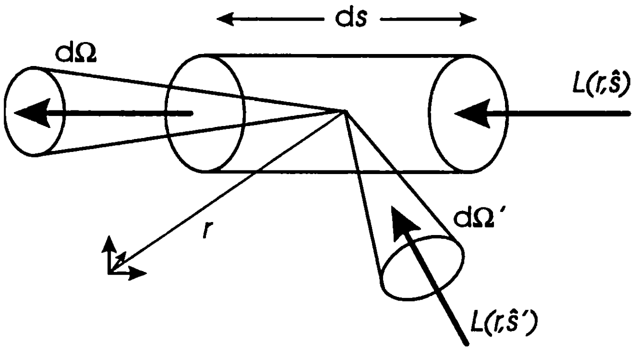

Figure **2.2** Elemental volume for Equation of Radiative Transfer.

2.3.2 The diffusion equation.

In the case of an infinite, homogenous slab, it is possible to expand the spatial phase function and the radiance in terms of a series of Legendre polynomials, $P(\hat{s}',\hat{s})$ and $P(\mu)$, where $\mu = \cos\vartheta$, with b_n derived from the orthonormality of P_n $(b_1{=}g)$;

$$f(\hat{s}',\hat{s}) = \frac{1}{4\pi}\sum_{n=0}^{\infty}(2n+1)b_n P_n(\hat{s}',\hat{s}) \qquad (2.35)$$

and

$$L(z,\mu) = \frac{1}{4\pi}\sum_{n=0}^{\infty}(2n+1)L_n(z)P_n(\mu) \qquad (2.36)$$

In the so called P_1 approximation[108,109] it is assumed that $L(z,\mu)$ is terminated after only two terms. This is only valid for materials where the effect of absorption is very much less than that of scattering, and even then only when used far away from the boundary regions[110,111]. The result is the general diffusion equation of the form;

$$D\nabla^2\psi(r) - \mu_a\psi(r) + s(r) = 0 \qquad (2.37)$$

where the ***diffusion constant*, *D*,** is equal to $(3(\mu_a + \mu_s(1 - g)))^{-1}$ and ψ denotes the radiant energy fluence rate. Through its ability to be solved analytically, this approximation has found extensive use in tissue optics[112,113] whilst a few laborious attempts have been made to include higher orders as well[114]. The applicability of the P_1 approximation to Finite Element analysis was first postulated by Keijzer *et al.*[115] and applied more recently to time-dependent problems by Schweiger[72] and Arridge *et al.*[116]. Finite Element's main advantages over analytical methods are its ability to handle complicated boundary geometries and inhomogeneities. These had previously only been dealt with by Monte Carlo models[117-126] and their associated long computation times. Monte Carlo methods still play an important role in modelling due to their ability to closely describe the propagation history of a photon and to handle arbitrarily complex geometries.

2.4 CHAPTER SUMMARY.

This chapter has defined the terminology used to describe light transport within this thesis which was derived from the two different languages that tend to be used in the literature bases of coherent backscatter and tissue optics. The section began with absorption and was followed by single scattering in a general sense and then within the Rayleigh and Mie regimes. The final section introduced multiple scattering and the equation of Radiative Transfer with a brief discussion on the diffusion approximation.

CHAPTER 3

CONVENTIONAL DETERMINATION OF OPTICAL TRANSPORT COEFFICIENTS.

The aim of this chapter is to review the methods that have been used to measure the various optical properties of biological tissues that are of interest to this study. Although little successful work has been achieved using *in vivo* samples, a few techniques apart from that of coherent backscatter are given consideration. The second section presents a literature survey of the relevant optical properties that have been published from previous studies and discusses the use of possible phantom materials for the validation work needed in chapter 7.

3.1 METHODS FOR MEASURING OPTICAL PROPERTIES.

3.1.1 Anisotropy factors and the Single Scattering Phase Function.

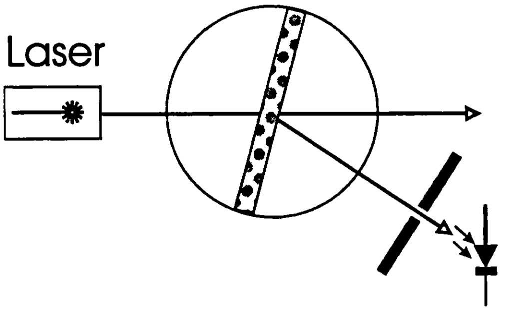

Figure 3.1 Goniometer arrangement for measuring the scattering phase function.

As mentioned in chapter 2, section 2.1.1, the angular distribution of light being deflected by scattering particles is normally far from uniform, particularly for tissue where generally the scattering is highly forward peaked. Measurement of this angular profile for photons that have been scattered only once can be achieved using a standard goniometer[127], see fig. 3.1. This apparatus uses samples that are sufficiently thin to ensure that there is an almost zero probability that any photon will be scattered more than once[92,128-133]. Once the angular profile has been obtained and the assumption of spherical symmetry made, then a simple numerical integration weighted by the cosine of the scattering angle gives the anisotropy factor. Comparison of the Henyey-Greenstein[98] analytical expression with the experimentally measured scattering phase function (Jacques *et al.*[129]) is then possible, but so far the fit has been poor. Significant equipment artifacts have still to be eliminated, particularly the refractive index mismatches that occur between the sample holder and air causing re-illumination of the sample. Additional causes of error result from the need to compress the sample within the holder thus deforming the cellular shape and structure, and the general instability of the biological material that plagues all photon transport measurements made *in vitro*. It is inconceivable that this technique can ever be used for *in vivo* measurements because of the sample mounting methods.

3.1.2 Refractive index of tissue.

Despite being a fundamental measurement this parameter has received only a small amount of consideration. Its implications within tissue optics are relatively minor for non interference effects when the artifacts are reduced to those of boundary reflections and refraction. When phase shifts have to be considered then the effect of the refractive index is crucial due to its inverse proportionality dependence on the total phase difference.

The only significant paper to try and come up with experimental values has been Bolin *et al.* (1989)[134], the values used previously had been chosen to be arbitrarily close to that of water. In this study a quartz optical fibre had its cladding removed and was placed in tissue. A measurement of the numerical aperture relative to a standard then gave the refractive index but the technique was fraught with contact problems between the tissue cells and the optical fibre. The refractive index values were found to be around 1.4 with a further slight increase for denatured protein and significant sample to sample variations.

Essenpries[92] (1992) measured the refractive index by exploiting the phenomenon of total internal reflection on samples compressed between the glass hemicylinders in a goniometer. The tissue sample and detector were aligned to record the specular reflection from the tissue/glass boundary. The angle of incidence was increased until no further changes in signal was seen above the critical angle. From the critical angle and refractive index of the glass, the calculation of tissue refractive index is trivial but inspection of the sample when mounted close to the critical angle showed a regional variation dependent on the degree of compression as well as the composition of the tissue. Despite this, measurements taken on native and coagulated rat liver again demonstrated that the refractive index increases with the denaturation of the tissue proteins (1.42 versus 1.38).

3.1.3 Absorption and Scattering.

These are by far the most important parameters needed for the models of light dosimetry and have received a proportionate amount of attention (for review see Wilson *et al.*[135,136]). It is unfortunate, but understandable, that no single method has become a conclusive standard, although for *in vitro* samples the most popular method has been the use of integrating spheres combined with the iterative adding-doubling, or inverse Monte Carlo methods, for extracting the reduced scattering and absorption coefficients from diffuse reflectance and transmission measurements.

As with all forms of measurements there are direct and indirect methods, distinguishable by the way in which the final quantity is determined. With a direct method the measurements themselves are of the final microscopic quantity, whereas the indirect method involves measurements of macroscopic quantities which are then translated using a mathematical model to the desired microscopic parameters.

3.1.3.1 *In vitro* methods.

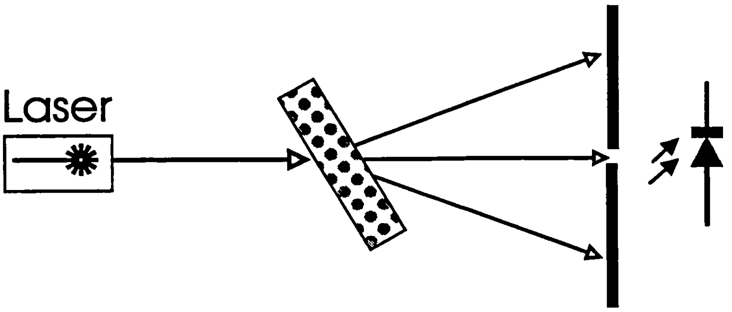

Figure 3.2 Collimated transmission apparatus for measuring the extinction coefficient.

The simplest direct method for measuring a transport parameter consists of taking a relatively thin sample and using a collimated light source aligned with a collimated detector. A reading is taken without and then with a sample present, see fig. 3.2. The ratio of the two readings is by definition the extinction coefficient. The inherent problems with this technique include those of specular reflections off the tissue boundaries, and to a lesser extent, the chance of multiply scattered photons behaving like unscattered ones.

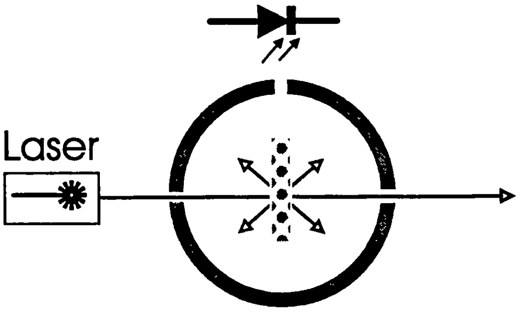

Figure 3.3 Single integrating sphere arrangement for measuring the scattering coefficient.

A direct method for determining the scattering coefficient could be to take the readings for the spatial phase function, integrate over the complete spherical surface, and then express as a proportion of the collimated detection. An almost insurmountable problem with this method is achieving the normalisation as the collimated detection is so large compared to that of the scattered light. An alternative is to place the sample within an integrating sphere as shown in fig. 3.3 but again the problems of multiply scattered and reflected light can exist.

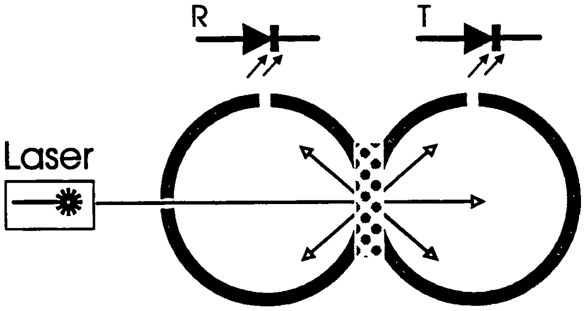

Figure 3.4 Double integrating sphere arrangement for simultaneous measurement of diffuse reflectance and transmission.

Use of indirect methods where reflection and transmission measurements are taken have been far more successful, despite not being model independent like the direct methods. The samples used can be suitably thick to prevent dynamic range problems and mounted in ways that are less likely to influence their optical behaviour e.g. compression.

Fig. 3.4 shows the general arrangement of integrating spheres used for determining reflectance and transmittance. The outputs of the photo diodes are compensated for the multiple re-illuminations of the samples from reflections off the wall, the non-perfect reflectivity of the walls, and the effects of the port sizes[137,138]. The readings are then normalised with respect to those obtained on reflectance standards and processed by the chosen model[139]. Each model is restricted to certain geometries and within certain ranges of dimensions; a brief revue of the main methods are summarised below:

1) Kubelka-Munk:

The Kubelka-Munk theory of light propagation considers diffuse radiation travelling through a one-dimensional homogenous slab with no reflection at the boundaries[140,141]. This is equivalent to the diffusion model for the case where the phase function is forward and backward peaked[105]. The reflection and transmission equations for the restrictive case of a diffuse illumination are;

$$T = \frac{y}{x\cosh(S_{KM}yt) + y\sinh(S_{KM}yt)} \qquad (3.1)$$

$$R = \frac{\sinh(S_{KM}yt)}{x\cosh(S_{KM}yt) + y\sinh(S_{KM}yt)} \qquad (3.2)$$

Where *t* is the thickness of the slab and

$$S_{KM} = \frac{1}{yt}\ln\left[\frac{1 - R(x - y)}{t}\right] \qquad (3.3)$$

$$A_{KM} = (x - 1)S_{KM} \qquad (3.4)$$

$$x = \frac{1 + R^2 - T^2}{2R}; \qquad y = +\sqrt{x^2 - 1} \qquad (3.5)$$

The major draw-backs of this model are the unavailability of a strong and perfectly diffuse light source, and the infinitely extending slab that theory demands.

2) *Kubelka-Munk translation:*

The same restriction applies to a method devised by van Gemert *et al.*[142] where the Kubelka-Munk coefficients are transformed into transport coefficients and then combined with a collimated transmission result to produce the scattering and absorption coefficients as well as the anisotropy factor[143].

3) *Iterative Adding-Doubling:*

This iterative procedure[144] offers increased accuracy over the previous methods by accurately modelling refractive index mismatches in conjunction with a model suited to the anisotropy, absorption, and scattering ranges found in tissues. Its drawbacks are those of being entirely numerical and suited to a sample geometry that consists of being an infinitely extending slab.

The underlying equation for the adding-doubling method is the radiative transport equation given earlier with the Henyey-Greenstein approximation of the phase function. The restrictions the theory places are:

a) The distribution of light can not change with time.
b) Samples are in the form of an infinite plane-parallel slab of finite thickness.
c) Samples are uniformly illuminated with each layer being optically homogenous.
d) All light is unpolarized.

The doubling method, first introduced by van der Hulst[105], assumes that the transmission and reflection parameters can be calculated for one slab. Two of these slabs can be considered to be placed side by side and the combined reflection and transmission calculated by summating the multiple paths that would be taken. If the first slab was so thin that only single scattering was taking place, then multiply scattering layers can be modelled by successively placing identical slabs on top of each other. The initial layer is modelled by using the diamond initialization method[145,146]. The adding method uses different layers with different properties to simulate laminated media and refractive index mismatches at the surface.

The iterative procedure consists of;

1) Guessing a set of optical coefficients.
2) Using the adding-doubling method to calculate from the coefficients, values for the reflection and transmission.
3) Comparing the results of stage (2) with experimentally measured values and using the difference to influence a change in the coefficients.

Stages (2) and (3) are then repeated until a match is found between the predicted and experimental values.

4) Inverse Monte Carlo:

The Inverse Monte Carlo method is an alternative to the iterative adding-doubling which reduces the constriction of having to have an infinitely extending slab modelled. The method[147-149] consists of taking an experimentally measured spatial phase function and performing a Monte Carlo simulation of light incident on the sample configuration. The configuration is fully described including the geometry, dimensions, refractive index and even the optical properties of the holder. As computation time makes an iterative procedure implausible, a whole series of samples are modelled with different absorption and scattering coefficients. Each simulation gives a predicted value for the diffuse reflectance and transmittance of the sample. An interpolation algorithm compares these simulated results with the experimentally measured values and the corresponding coefficients deduced. The only draw-back of the method is the large amount of computing time required but this is rapidly decreasing with the advent of faster and faster computers.

3.1.3.2 *In vivo methods.*

The Perturbation method which was used *in vitro*[95,150], and suggested for use *in vivo*[151] on tissue samples, consists of measuring the fluence rate distribution before and after the administration of certain light absorbing dyes. Computation of the optical coefficients can then be achieved through the induced optical attenuation and diffusion theory. This unfortunately requires an accurate knowledge of the absorbing dye concentration which could be achieved clinically using radiolabelling but is highly undesirable from considerations of both the cost and the ionising radiation dosage.

Photo-acoustic interaction involves the production of a pressure wave from the rapid thermal expansion of tissue following its exposure to a very short, high powered laser pulse. The shape of the acoustic transient immediately after its formation is dependent on the spatial profile of the illuminating light beam, the volume within which it was absorbed, and then the thermal and acoustic properties of the medium. A theoretical treatment suggests that by analysing the axial component of a laser induced shock wave, it is possible, with suitable knowledge of the thermal and acoustic properties of the tissue, to extract the absorption coefficient from the amplitude of the acoustic wave, and the effective attenuation coefficient from its profile. This latter coefficient is combined with the former to derive the reduced scattering coefficient. The technique was found to produce effective attenuation coefficients that are comparable to those obtained from integrating sphere measurements, but gave absorption coefficients that were up to a factor of 2.5 in error. This error produces further inaccuracies when extracting the reduced scattering coefficient[152].

The use of low coherence reflectometry has recently benefited from the production of high quality interferometers for use in fibre-optic communication industries[153]. The method is based on the assumption that for a light source with a short coherence length, any interference effects seen through an interferometer can only arise from light that has been scattered once at an optical depth equivalent to the path taken by light in the reference arm of the interferometer. Analysis of single scattering under various assumptions concludes that the reflected power is proportional to the product of the backscattering coefficient of the sample medium and the coherence length of the light source. The reflected power also decays exponentially at a rate equal to twice the attenuation coefficient of the medium when measured as a function of the translation distance of the interferometer's reference mirror (the backscattering coefficient is related to the so-called 'radar backscattering cross section' by particle density and is not the desired actual, or reduced, scattering coefficient). The method requires accurate data on the source coherence length, the incident power, and the divergence of the fibre-optic probe. Although significant noise problems exist requiring high quality instrumentation, the method has been used to gain interesting qualitative information on the laminar structures of tissues (e.g. skin) in terms of their optical coefficients. It is hoped that future work in this area may lead to reliable quantitative optical coefficients.

A thermal imaging system has been used to monitor temperature rises seen on the surface of tissues following step changes in the incident fluence rate from a high power laser[154]. The technique is strictly for use on *in vitro* human specimens due to laser safety regulations (power used was 0.5 to 5 W) but is included in this section as it is technically feasible for *in vivo* tissues. The rate of temperature rise for an illuminated sample is dependent on its thermal properties (specific heat capacity and diffusion), and the product of the fluence rate and absorption coefficient. As the local fluence rate is dependent on the incident power and the optical diffusion coefficient, the technique can be used to validate the optical properties measured with a conventional technique. The conclusion drawn was that the diffuse reflectance and transmission measurements associated with certain conventional techniques gave significant errors in the optical properties (in this experiment on *in vitro* human aorta at 514.5 nm, the thermal method gave an absorption coefficient that was lower by a factor between two and three, and a scattering coefficient that was around 50% higher than measurements taken using the diffuse reflectance and transmission method with extraction of the coefficients by the adding-doubling algorithm). A combination of the two techniques may yield superior results as the conventional technique has relatively low levels of error in the scattering coefficient.

The use of interstitial optical fibres placed within tissues to launch and detect photons have been used extensively with the diffusion approximation to determine the diffusion or reduced scattering coefficients[10,155-159]. Its main drawbacks includes the disturbing effect the fibres have on the light distribution, the difficulty of predicting the luminance field to the required precision, and actually determining the fibre positions and their orientation. Rather than placing the fibres within the tissue it is possible to place them on the surface and examine the temporal and steady-state radial distribution from collimated sources[136,160-163]. All these measurements are subject to refractive index uncertainties, the general pitfalls of the diffusion approximation (valid only for highly scattering media away from boundaries), and the low signal to noise ratio obtained when dealing with high optical attenuations. Care is also needed when working with inhomogeneous media to make sure particular areas are not dominating the measurement.

The steady state radial distribution of emergent light from a collimated source at the surface of a layered structure has been investigated by Kienle *et al.*[164]. The technique involved training a neural network to process a series of readings representing the intensity at various radial distances away from a collimated source into the optical coefficients of two distinct layers of predetermined thicknesses. The training data was generated with a Monte Carlo model of the experimental situation and proved to be successful up to the limitations imposed by inhomogeneites. The technique, like those associated with time of flight measurements, is also limited by the fact that as the scattering or absorption increases, the sensitivity decreases.

3.1.4 Section Summary.

The following points are listed as a summary of the common problems that are encountered with the methods described above (taken from Cheong *et al.*[139] not all of them are applicable to every method);

1) Physiological condition of the biological sample:- hydration level, homogeneity, species variability, frozen versus unfrozen state, *in vivo* versus *in vitro* state, fixed versus unfixed state, and surface smoothness of the sample slabs.

2) Irradiation geometries:- illuminating spot shape and divergence of the emitted light, diffuse or collimated.

3) Boundary refractive index matching:- presence of internal reflections.

4) Orientation of detecting interstitial fibres with respect to source fibre:- strong dependence for non diffuse light.

5) Numerical apertures of the sensing fibres:- defines the volume from where the detected light comes which in turn may not be representative of the local fluence rate.

6) Angular resolution of the photodetectors.

7) Separation of forward scattered light from unscattered light:- particularly scattering phase function measurements with a goniometer or for diffuse transmission measurements

8) Theory for the inverse problem:- whether the boundary conditions are representative of the real situation, the light is diffuse or collimated, or whether the degree of absorption is adequately accounted for.

3.2 PREVIOUSLY PUBLISHED OPTICAL COEFFICIENTS.

3.2.1 Scattering and absorption.

Within the infrared spectrum it is possible to assume that for most soft tissues the primary chromophore is water and for this reason expect an accurate reading of the absorption coefficient for many tissues to be within only an order of magnitude of that of water. For wavelengths in the visible or near infrared, the absorption is complicated by the presence of haemoglobin and other pigments such as melanin. It is worth noting that the absorption coefficient may be temperature dependent as the value for water at 1064 nm changes by almost 20 per cent between room temperature and its boiling point which is regularly achieved during laser surgery[92,165].

The cause of scattering is predominantly the presence of discontinuities in the refractive index across the medium arising from the cell's internal and external membranes. In the case of grey brain matter, these internal membranes are associated with mitochondria and in the case of white brain matter, with the layers of myelin[78].

The amount of published data on the optical coefficients of biological tissues at 1064 nm is not extensive and in many cases subject to large experimental errors both in the technique used for measuring the coefficients and in the tissue preparation. This is evident from the cases where different authors have measured the same biological material with significantly different results (e.g. Rat liver, Table III.1). The degree of disagreement is beyond what may be expected from inter-sample variations and has major implications in the certainty

Table III.1 Review of the optical coefficients for native biological media at 1064 nm.

Medium	μ'_s (mm^{-1})	μ_a (mm^{-1})	g	Author
Idaho Potato	0.67	0.036		Karagiannes
Sweet Potato	1.3	0.045		Karagiannes
Calf Brain	0.29	0.122		Karagiannes
White Brain	0.55	0.04	0.95	Roggan
Canine Myocardium	0.367	0.007	0.973	Splinter[a]
	0.451	0.04	0.974	Splinter[b]
	0.72	0.04	0.96	Roggan
Bovine Myocardium	0.49	0.03	0.965	Roggan
Human Myocardium	0.639	0.03	0.964	Splinter[b]
	1.25	0.04	0.95	Roggan
Human Aorta	2.39	0.053	0.9	Essenpreis[a]
Porcine Aorta	2.3	0.21		Agah
Porcine Myocardium	0.455	0.03	0.965	Roggan
	0.427	0.044		Derbyshire
Bovine Muscle	0.28	0.12		Karagiannes
Turkey Muscle	0.16	0.04	0.98	Roggan
Bovine Liver	0.176	0.053		Karagiannes
	0.27	0.027		Essenpreis[b]
	1.0	0.04	0.90	Roggan
Porcine Liver	0.24	0.05	0.97	Roggan
Human Liver	1.05	0.03	0.93	Roggan
Rat Liver	0.79	0.2	0.948	Van Hillegersberg
	1.4	0.88	0.93	Pickering
	0.488	0.59	0.92	Parsa
	0.63	0.087	0.94	Essenpreis[c]
	0.825	0.129	0.870	Essenpreis[a]
Canine Prostate	0.44	0.04	0.96	Roggan
Human Prostate	0.4	0.03	0.95	Roggan
	0.643	0.147	0.862	Essenpreis[a]
Human Skull	1.2	0.05	0.9	Roggan

Table III.2 Review of optical coefficients for coagulated biological media at 1064 nm.

Medium	μ'_s (mm^{-1})	μ_a (mm^{-1})	g	Author
White brain	0.91	0.05	0.93	Roggan
Canine Myocardium	0.836	0.01	0.96	Splinter[a]
	1.082	0.035	0.956	Splinter[b]
	2.04	0.03	0.94	Roggan
Bovine Myocardium	1.54	0.03	0.945	Roggan
Human Myocardium	2.4	0.06	0.94	Roggan
Human Aorta	2.93	0.046	0.9	Essenpreis[b]
Porcine Aorta	2.3	0.2		Agah
Porcine Myocardium	1.2	0.03	0.94	Roggan
	1.743	0.051		Derbyshire
Turkey muscle	3.12	0.04	0.88	Roggan
Bovine liver	1.95	0.03		Essenpreis[b]
	3.15	0.05	0.935	Roggan
Porcine liver	1.5	0.06	0.95	Roggan
Human liver	2.15	0.03	0.95	Roggan
Rat liver	1.75	0.074	0.62	Essenpreis[c]
	1.62	0.084	0.885	Essenpreis[a]
Canine liver	0.88	0.05	0.96	Roggan
Human Prostate	0.9	0.04	0.95	Roggan
	1.12	0.080	0.861	Essenpreis[a]

that can be placed in the output of any luminance model using these coefficients. There are regrettably, as yet, no experimental results available for any *in vivo* or polarization dependent optical properties of biological media at 1064 nm. Table III.1 and Table III.2 shows a literature review of the *in vitro* reduced scattering and absorption coefficients at 1064 nm that have been measured and are of interest in this study for native and coagulated tissues respectively.

The references Parsa *et al.*[166], and Karagiannes *et al.*[167] are taken from Cheong *et al.* 1991[139] and the rest from; Derbyshire *et al.*[168], Roggan *et al.*[148] and Essenpreis[a] [92], Essenpreis[b] *et al.*[169], Essenpreis[c] *et al.*[170], Agah *et al.*[171], van Hillegersberg *et al.*[172], Splinter[a] *et al.*[173], Splinter[b] *et al.*[174], and Pickering *et al.*[175]. The Inverse Monte Carlo method was used for parameter extraction in both the Roggan and Essenpreis experiments but with different methods of tissue preparation:- Essenpreis used fresh samples whereas Roggan took shock frozen homogenized samples. Shock freezing the samples was done with the intention of facilitating the sectioning and preservation of the sample without causing any frost damage. Frost damage results from the formation of the large ice crystals that can occur with gentle cooling and is responsible for a large change in the optical coefficients recorded for Rat liver by Essenpreis[92]: freezing decreased μ'_s from 0.825 to 0.168 mm^{-1}, increased μ_a from 0.129 to 0.193 mm^{-1}, and increased g from 0.870 to 0.915. Further variations for the coagulated sample coefficients will exist depending on the precise method used for coagulation. Although the method of placing the tissue in hot water was used in all the studies, the degree of contact with the water and the actual temperature profile of the tissues with time are likely to cause inconsistencies. The data from Splinter uses a 3-flux Kubelka-Monk model with a subsequent transform into the transport coefficients, whilst Parsa and Karagiannes use a 1-dimensional diffusion approximation to the transport equation. Derbyshire uses an analysis method based on the work of Reichman[176] and Egan[177] which is an extension of Kubelka Monk theory.

3.2.2 Refractive index.

Essenpreis[92] measured the refractive index of Rat liver at 1064 nm to be 1.38 and 1.42 respectively for the native and coagulated states. Bolin *et al.*'s 1989 experiments[134] showed that there were few exceptions of tissues with a refractive index outside the range of 1.38 to 1.41 at 633 nm and that the general trend is for the refractive index to decrease with an increase in wavelength as is observed for

Table III.3 Specific refractive index increments for various cellular constituents.

Substance	Specific refractive index increment β
Blood constituents	
Plasma albumin (Bovine)	0.001862
Serum albumin (Human)	0.002862
Serum globulin (Human)	0.001830
Fibrinogen (Human)	0.001880
Haemoglobin (Human)	0.001942
Beta-lipoprotein	0.001700
Nucleic acids	
DNA	0.001810
RNA	0.001940
Diluted inorganic salts	
NaCl	0.001630
KCl	0.001150
$CaCl_2$	0.002100
Carbohydrates	
Sucrose	0.001410
Glucose	0.001430
Starch	0.001330
Amino Acids	
Glycine	0.001790
Alanine	0.001710
Valine	0.001750
Tryptophan	0.002500

most optical materials. The numbers given tend to be the average refractive index of the tissues and do not give any indication of the actual refractive index of the individual constituents. It is after all the variations between the different constituents of the organelles that produces scattering. The main constituent of tissue is water which at 1064 nm has a refractive index, n_w, of 1.326[178] and is slightly temperature dependent. The refractive index of various organelles can be estimated by using the specific refractive index increment, β, in conjunction with the concentration of cellular solids C_s (percentage weight per unit volume; % *w/v*) in;

$$n_c = n_w + \beta C_s \tag{3.6}$$

Table III.3 gives the respective values of β for various cellular constituents taken from Ross[179] for visible wavelengths which may be assumed to be similar to the values in the infra-red due to the relatively weak wavelength dependence.

3.2.3 Polarization effects.

3.2.3.1 *Polarization memory.*

The work of Martinez and Maynard[180,181] has recently shed light on the complex problem of how the polarization of a photon is maintained as it propagates through a turbid medium. A Monte Carlo model of polarized light propagating through a slab geometry of variable length (L) was performed for both Mie and Rayleigh Scattering and the degree of polarization for both circular (P_c) and linear (P_l) light calculated for the emerging wave vector. The degree of polarization versus slab thickness for Mie scattering was shown to follow an exponential decay which fitted experimental results well. The characteristic lengths, l_p , within the equation;

$$P \sim e^{\frac{-L}{l_p}} \qquad 3.7$$

are tabulated in Table III.4. The fact that for the Rayleigh regime, the linear polarization has a greater characteristic length than the circular polarization, whilst the reverse is true for the Mie regime, can be rudimentarily understood from knowing that circularly polarized light has its helicity reversed on a backscattering interaction with a Mie scatterer, whereas a Rayleigh interaction results in only minor changes. The major implication of this is that for backscattered light, with its dominant low orders of scattering, circularly polarized light has a polarization degree tending towards around 0.25 for the non absorbing case of an infinite half space of moderate Mie scatterers[180,181] (514.5 nm light propagating through a weak aqueous suspension of latex microspheres which are 800 nm in diameter). This figure will increase with absorption which by cutting off the higher orders of scatter, increases the contribution made by the lower orders to the total effect. For the linearly polarized case with Mie scatterers, like the situation with either polarization states in the Rayleigh regime, the backscattered light is almost entirely depolarized.

Table III.4 Characteristic lengths of depolarization.

Scattering Regime	**Characteristic length of Depolarization; l_p (units:- l'_s)**	
	Linear Polarization	Circular Polarization
Rayleigh	0.935	0.481
Mie	1.39	2.79

3.2.3.2 *Polarization dependence on transport coefficient.*

Jarry *et al.* 1994[182] have investigated the polarization properties of biological tissues. The measurements were taken using an optical heterodyne technique with an adapted Mach-Zehnder interferometer. The polarization dependent extinction coefficients were measured at 633 nm for bovine liver and muscle samples. The results show a clear dependence on the polarization state and in the case of striated muscle, a variation with orientation. The fact that for liver, the circularly polarized extinction coefficient is higher than the linear one, yet for muscle we have the opposite case, is indicative of a scattering shape or size dependence. This phenomenon ties in with Martinez's work discussed above which shows differences in the polarization state of backscattered light from structures containing either Mie or Rayleigh sized spheres. These dependencies can be considered to make either the measurements from coherent backscatter more ambiguous than the conventional non-polarized/non-orientated techniques, or that on the other hand they yield more information.

The polarization dependent extinction coefficients from Jarry *et al.*[182] are shown in Table III.5 along with the non-polarized coefficients derived with conventional techniques. The references used were Karagiannes *et al.* 1989[167], Marijnissen and Star 1987[183], and Wilson *et al.* 1986[150] and are susceptible to the many experimental errors and inconsistencies already discussed. The order of magnitude disagreements between the results is of concern and discussed by Jarry *et al.* Although the discrepancies exist the trend is still of interest.

Table III.5 Polarization dependent extinction coefficients for various biological media along with non polarization dependent equivalents.

Bovine Tissue	**μ_t (mm^{-1}) from Jarry *et al.* 1994**			**μ_t (mm^{-1}) $= \mu_s + \mu_a$**	**Author**
	Linear Polarization	Circular Polarization	Fibre Orientation	No Orientation	
Liver	1.09	1.21	None	10.04	Roggan 1994
Muscle	2.20	1.81	Vertical	0.83	Marijnissen 1987
	1.78	1.46	Horizontal	12.1	Wilson 1986
	1.00	0.86	Parallel	32.8	Karagiannes 1989

3.3 MATERIALS FOR PHANTOMS.

The choice of a biological phantom is of great importance in this study in order to validate the results obtained with biological tissues. The main requirements are that the absorption and reduced scattering coefficients should be similar in magnitude to real tissues and if possible, with similar degrees of scattering anisotropy. An additional constraint for the work with coherent backscatter is that the refractive index mismatches at the boundaries, and the refractive index of the medium should match those values incorporated in the theory used to analyze the results. One possible scatterer is Intralipid^{TM} (10 % fat emulsion for intravenous use: Pharmacia Ltd, Milton Keynes, U.K.) for which the optical properties are well documented[184,185]. At 1064 nm, the scattering coefficient as a function of dilution is given by Mie theory as being 0.0134 mm^{-1} L mL^{-1} with the anisotropy factor at 0.48. The experimental results show a good agreement[184] with a scattering coefficient of 0.0131 mm^{-1} L mL^{-1} and an extinction coefficient of 0.0136 mm^{-1} L mL^{-1}. A comparison made at 630 nm of these experimental results with other published data gives an agreement that is within only 10%.

Possible phantom absorbers include the use of India Ink[186] or China Ink, both of which are composed of a fine suspension of carbon particles. Care should be taken when choosing an absorbing ink due to the possibility of a chemical reaction with the biological medium. The China Ink (rotring™, Hamburg, Germany) was measured to have an extinction coefficient of around 0.5 mm^{-1} L mL^{-1} at 1064 nm when expressed as a function of dilution (experiments conducted within this department by Dr. Matthias Kohl 1993). Detailed description of the manufacture of solid phantoms is given in the work of Firbank and Delpy[187-189]. It is unfortunate that these stable phantoms can not be used in this study for calibration purposes as the high refractive index mismatch at the surface is unrepresentative of any biological medium (refractive index of plastic substrate = 1.56).

3.4 CHAPTER SUMMARY.

This chapter began with a review of the methods that have been used to date to try and measure the optical properties of biological tissues. These included the refractive index, the scattering anisotropy factor, the absorption coefficient and either the scattering coefficient or the reduced scattering coefficient. The techniques were split into two sections: those that are restricted to *in vitro* samples and those which can in theory be applied *in vivo*. The restrictions of each method were highlighted and a conclusion drawn that no single *in vivo* technique has emerged as a gold standard. None of the techniques described are capable in themselves of simultaneously matching the advantages listed below that the coherent backscatter method offers;

1) Samples low volumes of tissue.
2) Can be used *in vivo*.
3) Increased sensitivity as the scattering coefficient increases.
4) Can handle large amount of absorption in the presence of a large scattering coefficient.
5) Uses relatively cheap experimental equipment.
6) Offers potential of real time data acquisition and parameter extraction.

The second section reviewed a selection of the published data on the optical properties of tissues that are relevant to this study. Comparisons between coefficients for the same kind of material that were extracted in different studies showed a level of disagreement beyond what may be expected from inter-sample variations. The section also reviewed the phantom materials that are used for the validation experiments in this study.

CHAPTER 4

MONTE CARLO METHODS FOR DERIVING PHOTON STATISTICS.

This chapter describes a validated Monte Carlo model that is used to provide statistics for light that is backscattered out of a turbid medium. The simulation is computationally slow but produces results that, unlike those from diffusion theory, are valid for the vast majority of the photons that are backscattered out of biological media. This chapter is split into three sections. The first describes and validates the program that produced the photon statistic data bases that are processed in chapter 5, section 3.1, to predict the coherent backscattering peak line shape. The second section involves estimating some statistics that describe the maximum depth the backscattered photons penetrated, the average depth they propagated at, and an idea of the dimensions for the tissue zones that are interrogated by the coherent backscattering technique. The last section describes a method used in this study to predict the shape of the fluence rate patterns within the tissue that are dependent on the refractive index mismatch at the surface and on the degree of scattering anisotropy.

Monte Carlo models are well established alternatives to the diffusion approximation of the radiative transfer equation for light transport. The main set of advantages are listed as;

1) Diffusion approximation is only valid for a highly scattering medium.
2) Diffusion approximation is not valid near boundaries.
3) Monte Carlo models can simulate scattering and absorption inhomogeneities.
4) Monte Carlo models can cope with geometries other than an infinite half space.

Monte Carlo modelling was first conceived in the eighteenth century in the form of "Buffon's needle" problem which was used to derive π from the number of lines on a grid that a needle would cross if it was randomly dropped. The idea of a formal computer model was then proposed by Metropolis and Ulam in 1949[117] and has since found extensive use in particle, nuclear, and radiation physics as well as atmospheric and tissue optics. The name is derived from the random number sampling associated with gambling. Several books and review articles have been published which deal with the history, optimisation techniques, and methods used for validating the data[118,119,190].

The model used in this study was developed from a validated luminance prediction program used to study the effects of optical coefficients on heat deposition during laser photocoagulation[92,191]. The model has the ability to simulate the interactions of photons in three dimensional infinite half spaces according to any scattering phase function.

4.1 GENERATION OF BACKSCATTER DATA BASES.

The Monte Carlo model used is summarised in the flow diagram shown in fig. 4.1 and describes the backscattering of photons that arose from an infinitesimally wide, collimated illumination profile, perpendicular to the surface which contains a refractive index mismatch.

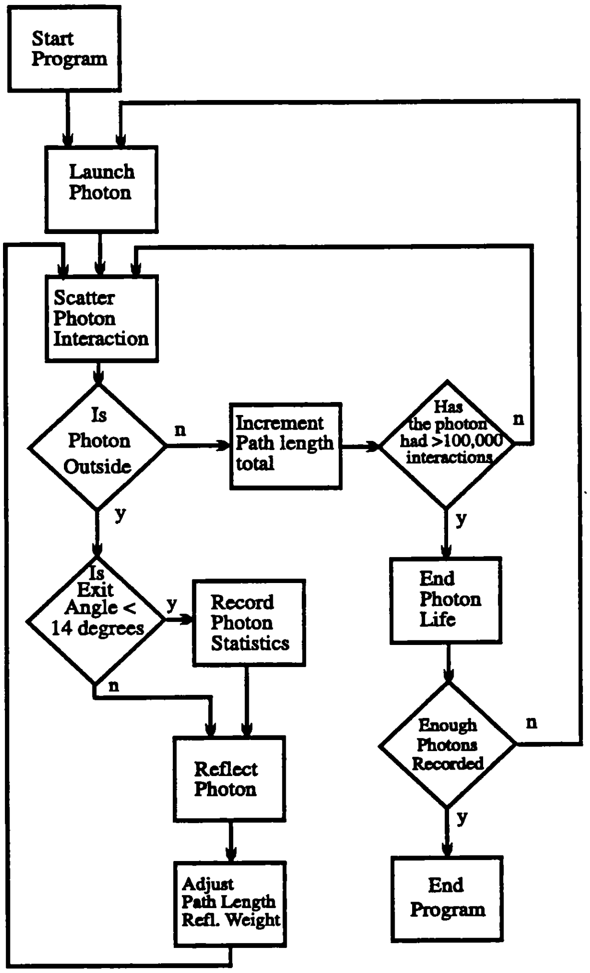

Figure **4.1** The flow diagram for the Monte Carlo program used to generate the backscattering data bases.

The information recorded in the data bases for photons that are backscattered to within around 14° of the incident direction includes;

1) The number of photon scattering interactions.
2) The path length of the photon within the half space.
3) The photon weight having been decreased by reflection (Fresnel losses).
4) The *x*, *y*, and *z* displacement of the last scattering interaction from the initial scattering point.

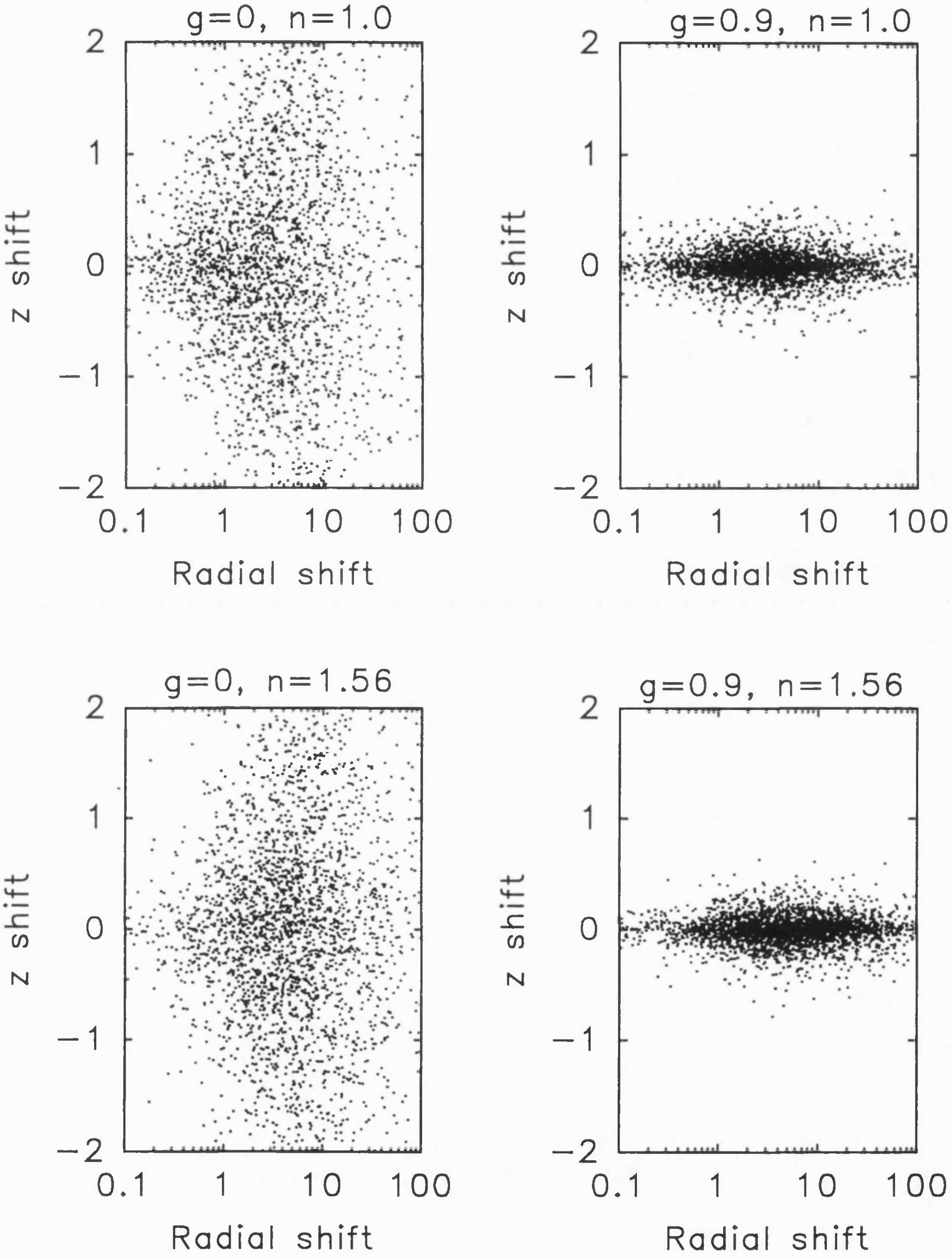

Figure **4.2** Scatter plots of the last scattering position of backscattered photons relative to their initial scattering position. All dimensions are specified in reduced scattering mean free paths.

All spatial distances were recorded in terms of scattering length units. Scatter plots showing sections of four of the data bases are shown in fig. 4.2. The dots represent the last photon scattering positions relative to the first in reduced scattering mean free paths. The photons have either been backscattered without an internal reflection or have suffered only total internal reflections. The data bases were chosen to show the influence of anisotropy and of the refractive index mismatches. The latter manifests itself as an effective shift in the distribution as though the scattering coefficient had been reduced. These effects are shown by analysing the data bases to deduce the median position of all the radial coordinates and the median position of all the z (depth) coordinates as shown in Table IV.1. This table additionally justifies the computationally expensive procedure of modelling all the backscattered photons but only selecting those that exit at a direction close to that of the incident beam. This is achieved by showing the different results obtained from simulations that recorded the characteristics from photons that exited at any angle (full cone).

Table IV.1 Median values of the radial and z coordinate of the last scattering position of exiting photons from an infinite half space, relative to the initial scattering position.

Anisotropy factor	Refractive index mismatch	Narrow cone exiting positions (l'_s)		Full cone exiting positions (l'_s)	
		median radius	median z	median radius	median z
0	1.0	3.193	0.0052	2.812	-0.138
	1.42	4.797	0.0030	--	--
0.9	1.0	2.911	-0.0012	2.700	-0.0168
	1.42	4.326	0.0018	--	--

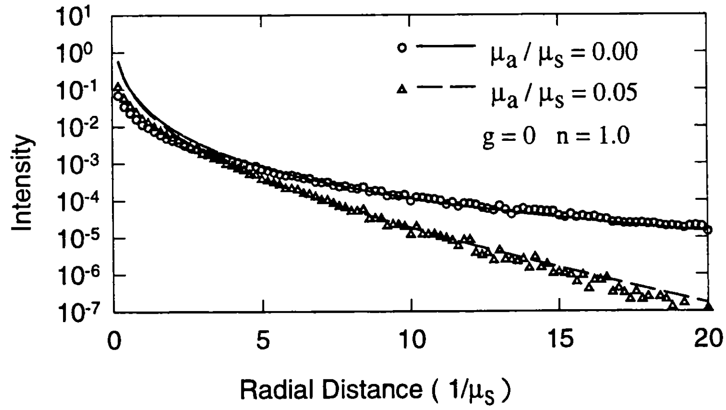

Figure **4.3** The radial distribution of emergent light for the Diffusion Approximation (lines) and Monte Carlo simulations (symbols) for various scattering to absorption ratios.

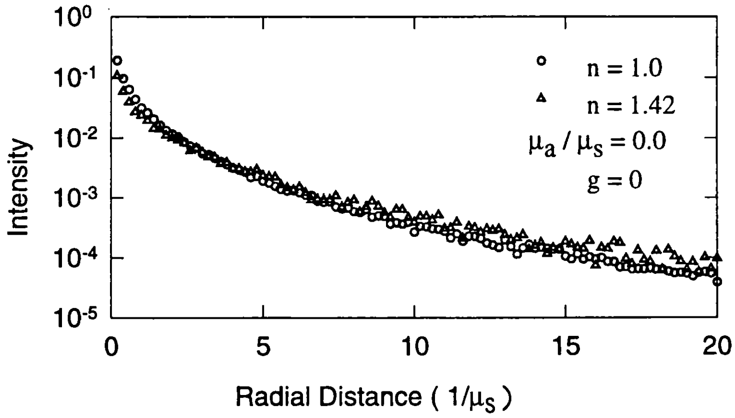

Figure **4.4** The radial distribution of emergent light from Monte Carlo simulations for different refractive index mismatches across an air-medium boundary.

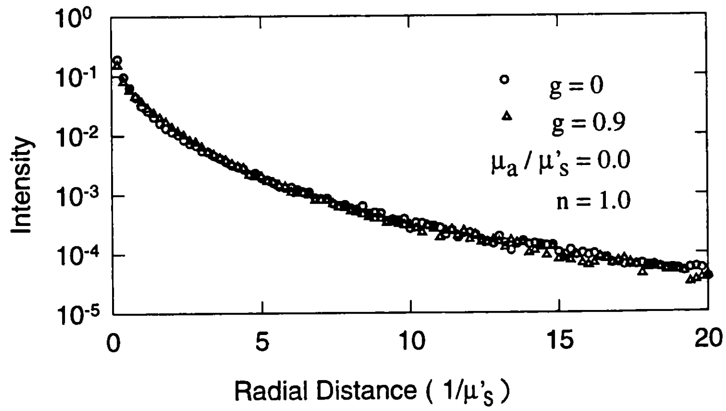

Figure **4.5** The radial distribution of emergent light from Monte Carlo simulations for different anisotropies within the Henyey-Greenstein phase function.

The maximum number of photon interactions was limited to 100,000. The contribution of a photon to the backscattered intensity having exited a biological sample after more than 100,000 interactions can be assumed to be negligible. This figure is justified by the data shown later in fig. 4.9. The scattering lengths used were taken from a Poisson interval distribution with an average of 1 unit whilst the scattering angles were taken from the Henyey-Greenstein[98] phase function with various anisotropy factors. If a photon interacted with the refractive index mismatch then the photon was split into two, one was allowed to exit whilst the other was reflected. The exiting photon would have its reflection weight decreased according to the Fresnel transmission coefficient for unpolarized light and if it satisfied the direction criterion, would have its details recorded. The reflected photon had its direction altered and continued to propagate as before with the reflection weight adjusted according to the Fresnel reflection coefficient at the incident angle.

A series of data bases was created containing in excess of 40,000 photon histories in each, for respective sets of refractive index mismatches and anisotropy factors. The data bases could be processed to simulate the required exiting statistics from any combination of scattering and absorption coefficients by scaling the spatial distances by a factor: l_s ($=1/\mu_s$), and assigning a total photon weight, or the propagator term in equation 5.1, δ_{ij} as;

$$\delta_{ij} = PWR\, e^{-\mu_a d} \tag{4.1}$$

where d is the total path length of the photon having been scaled by l_s, and PWR is the photon weight as decreased by the reflection losses.

The method was validated by processing the data bases to give a radial distribution of exiting light. This was compared to a diffusion approximation for the situation where the incident light is collimated. This model is dependent on the reduced scattering coefficient and the absorption coefficient, and solves the source function by modelling it as a line source with a strength that decreases exponentially along its length[192]. The results in figs. 4.3, 4.4, and 4.5 show that for radial distances in excess of 10 scattering mean free paths from the source, the two curves show similar behaviours. The discrepancies near to the source can be explained by the inability of the diffusion approximation to handle low orders of scattering near to boundaries, plus the fact that the radial position was calculated from the last scattering position rather than the point of exit on the surface.

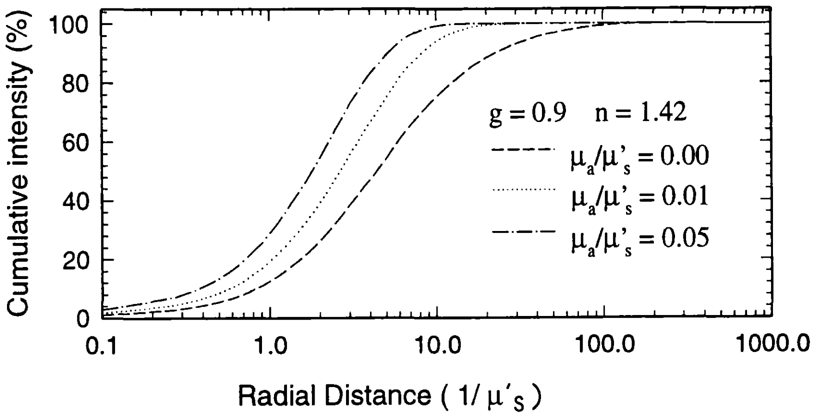

Figure 4.6 The percentage of the total intensity that gets backscattered within the radial distance for different levels of absorption.

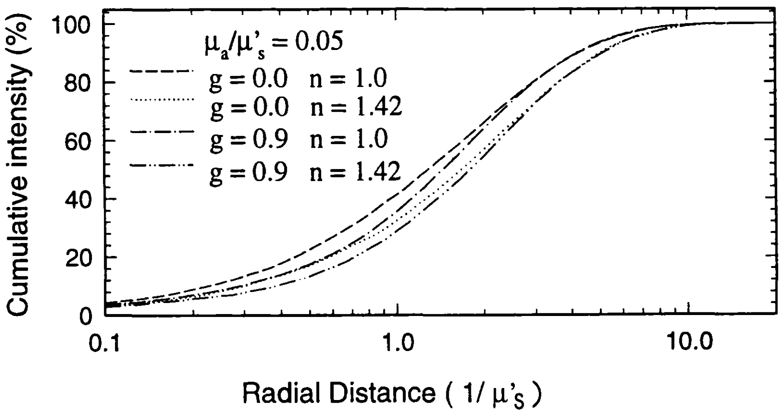

Figure 4.7 The percentage of the total intensity that gets backscattered within the radial distance for a fixed level of absorption but different anisotropies and refractive indices.

When the data bases were analyzed to show the percentage of the total multiply scattered light that emerged within a certain radial distance, then the graphs shown in figs. 4.6 and 4.7 are obtained. These figures show how the majority of the light can be considered to have been backscattered out within 5 reduced scattering mean free paths from the entrance point. When the data bases were analyzed according to the order of scatter then the results shown in figs. 4.8, 4.9, and 4.10 were obtained for backscattered light. Fig. 4.9 shows that for isotropic scattering from media with the ratios of scattering to absorption that are likely to be found in biological media, around fifty per cent of the scattered light comes from the first 5 or so orders of scattering and around 95 per cent from the first 100. This confirms that even with anisotropies in excess of 0.9, we can still expect all the light to have come from photons that have been scattered less than 100,000 times.

Figs. 4.4, 4.7, and 4.10 show that the effect of a refractive index mismatch is to encourage higher orders of scattering by preventing the photons from exiting. The absolute intensity of non-interfering backscattering light was shown to vary with the ratio of scattering to absorption as displayed in fig. 4.11 for the total amount of backscattered light, and then in fig. 4.12 for the total minus the single scatter component. The data representing the incoherent intensities, labelled Chandrasekhar, was predicted by using the incoherent terms in equation 5.4 with the respective -1 term absent for the total backscattered intensity, and then present if the single scatter component was to be ignored. Fig. 4.13 shows how the single scatter contribution to the total backscattered intensity increases as expected with increasing absorption.

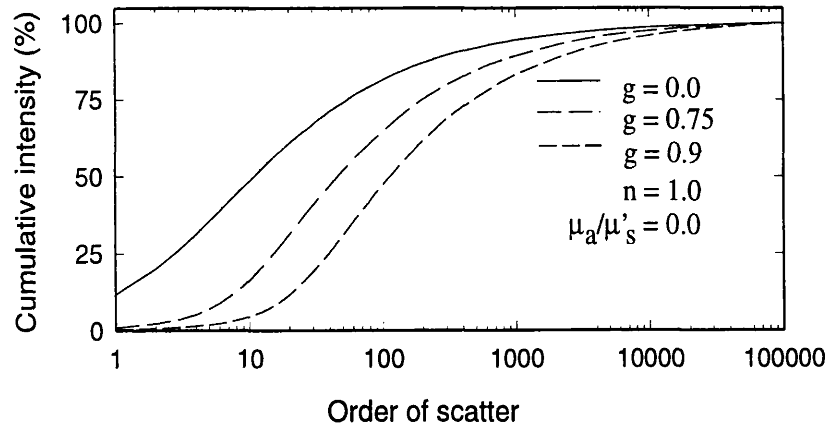

Figure **4.8** The cumulative contribution of scattering order to the backscattered intensity for various anisotropies.

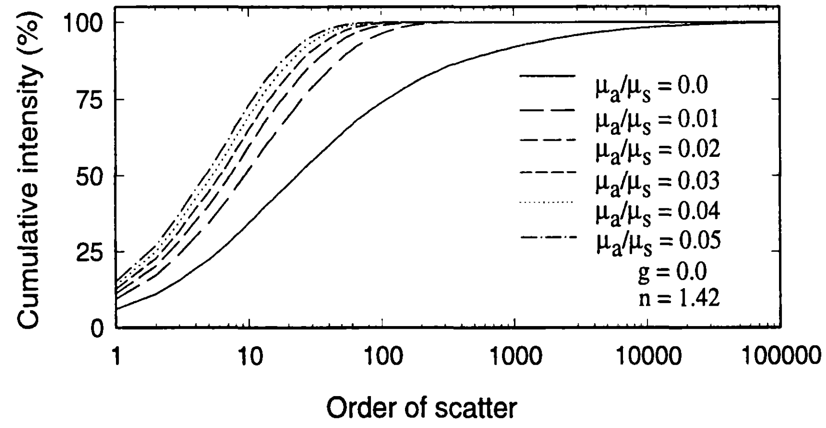

Figure **4.9** The cumulative contribution of scattering order to the backscattered intensity for a selection of absorption to scattering ratios.

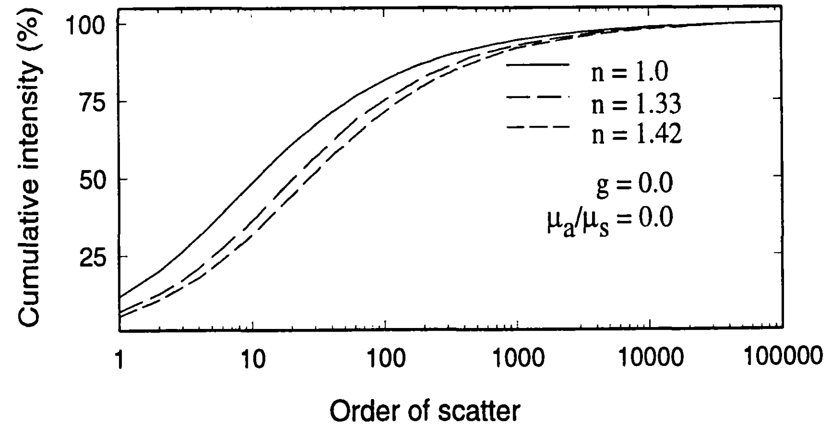

Figure **4.10** The cumulative contribution of scattering order to the backscattered intensity for a selection of refractive index mismatches for medium - air boundaries.

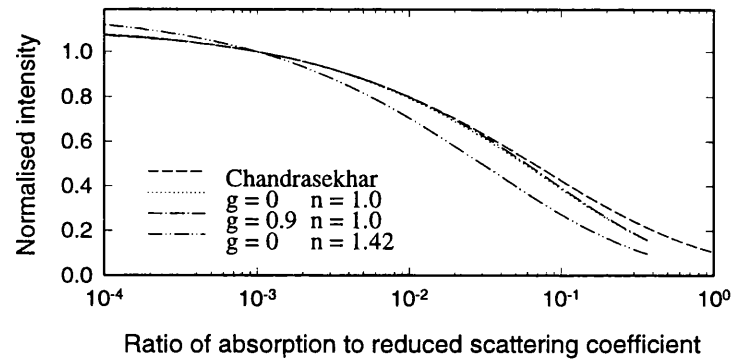

Figure **4.11** Results giving the background intensity level for the total backscattered light as a function of the absorption to scattering ratio, normalised at the ratio 0.001.

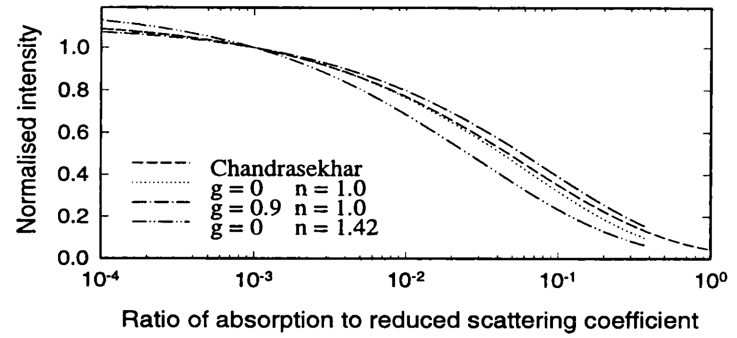

Figure **4.12** The background intensity level for the multiply scattered emergent light as a function of the absorption to reduced scattering ratio, normalised at the ratio 0.001.

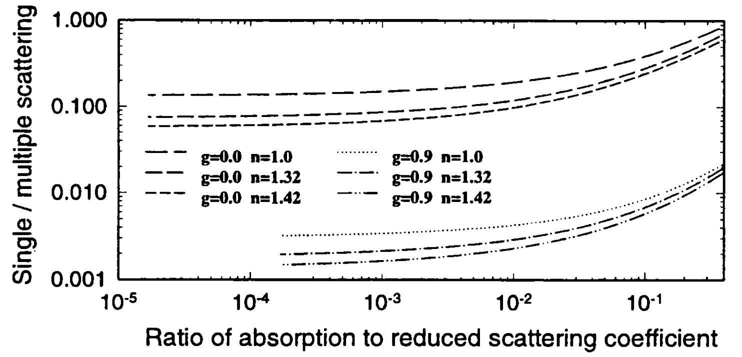

Figure **4.13** The ratio of the single to the multiply scattered contributions to the backscattered intensity as a function of the absorption to scattering ratio.

4.2 PHOTON STATISTICS OF BACKSCATTERED LIGHT

The aim of this section is to investigate the effects of anisotropic scattering and refractive index mismatches on the spatial distributions of light within a backscattering medium. The intention is to give an indication as to the size of the tissue zones that are being interrogated by the coherent backscatter technique. If it is known that the medium is not homogenous then this data will give an indication as to the depth and dimensions an inhomogeneity will have to have to create an artefact. As with the first section of this chapter, the approach taken involves the use of Monte Carlo models to simulate the diffusing light as the diffusion approximation method is not valid for the short paths taken near to the boundary. The data presented provides estimations of the average maximum depth a backscattered photon reaches, the average depth of the photon in its passage, and the shape of the most likely path taken. The data is often restricted to cases of high albedo as the presence of absorption can only reduce the values of the average photon depths by lowering the chance of the long and inherently deeply penetrating photon paths from existing.

4.2.1 Average depths and zones of interrogation.

Previous works published on these parameters[193,194] have been restricted to situations where the scattering is isotropic, the detected light is diffuse, the tissue-air boundary is simulated as an absorbing layer, and the photon source function is modelled as an isotropic source placed one scattering mean free path below the surface. In these two studies the analytical results are favourably compared to the results from a Monte Carlo model, but only for the long photon paths that can be assumed to have behaved diffusively. The works conclude that the average maximum depth a backscattering photon penetrates[193] varies according to $\rho^{2/3}$

where ρ is the radial distance of exit from entrance points, and that the mean depth probed by a backscattered photon[194] varies as $\rho^{1/2}$. This study reports the behaviour of photons that enter the medium from a collimated beam normal to the surface, are scattered through a medium with either an isotropic or anisotropic phase function with path lengths that follow a Poisson distribution. The tissue-air boundary was also modelled with and without a refractive index mismatch. The simulation, when needed, detected only the light that is backscattered into a narrow angular cone centred on the axis of injection. The program used was an adaptation of the simulation used in section 1.1 of this chapter and was programmed to record in a set of radial distance bins the means and variances for the maximum depth that a photon reached, the average depth of the scattering path, and the actual path length taken when performing the multiple scattering sequences that re-emerge. The bins were spread apart by an exponentially increasing distance such that 25 points were contained within each decade, and annotated by the logarithmic centre of the bin.

The results showing the means are displayed in fig. 4.14 and the standard deviations in fig. 4.15. The simulation was terminated once the statistical noise was reduced to a satisfactory degree for the photon mean depths (in general the inter-bin ripple over any 5 consecutive bins was kept below 10% of their average value). The higher levels of statistical noise present in the standard deviation data was reduced by using a 3 point running average filter as further simulation time was considered to be excessive.

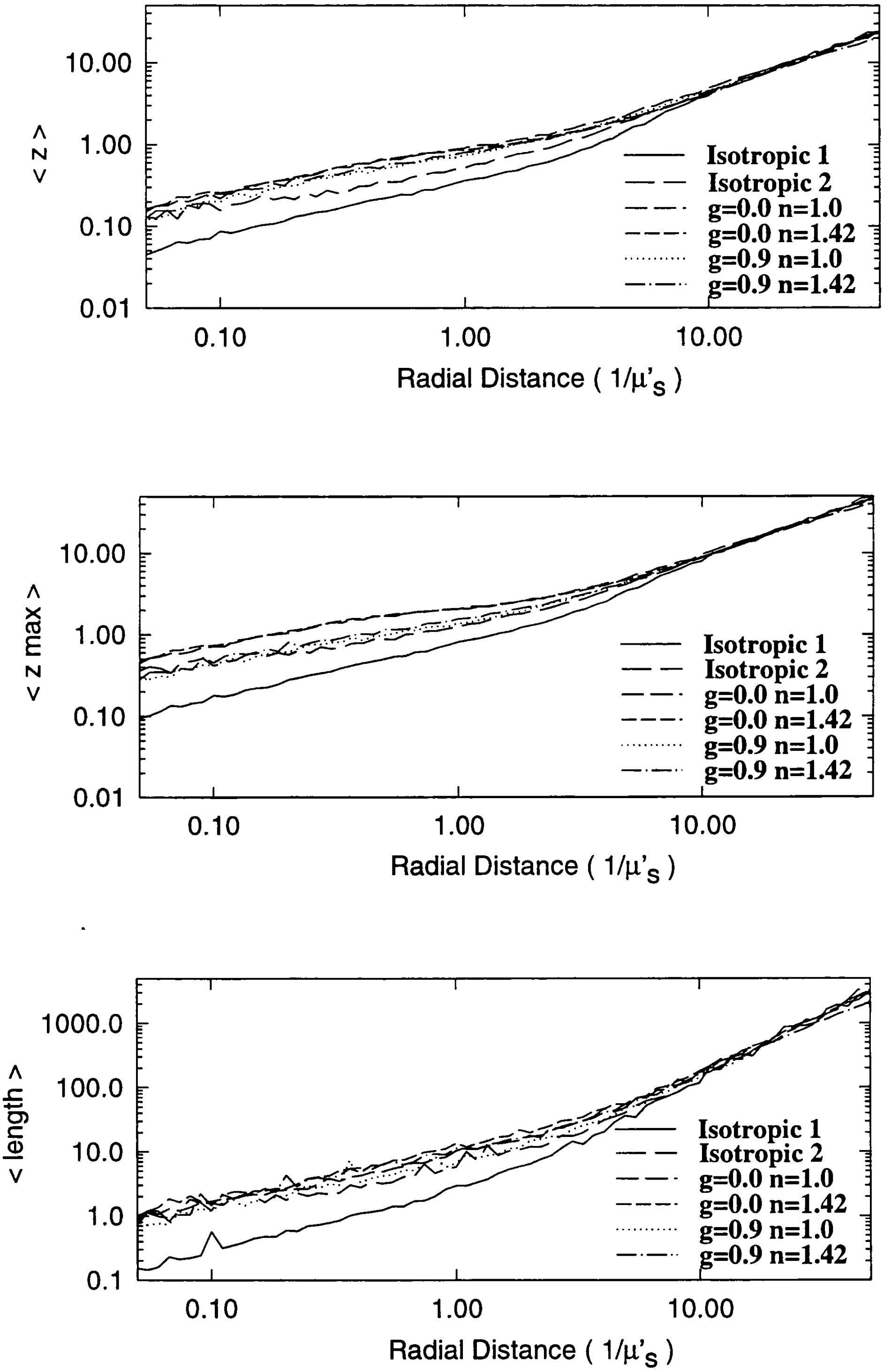

Figure **4.14** The average values for a photon of; the mean depth of travel (top), the maximum depth of penetration (middle), and the path length taken (bottom), versus the entrance-exit distance.

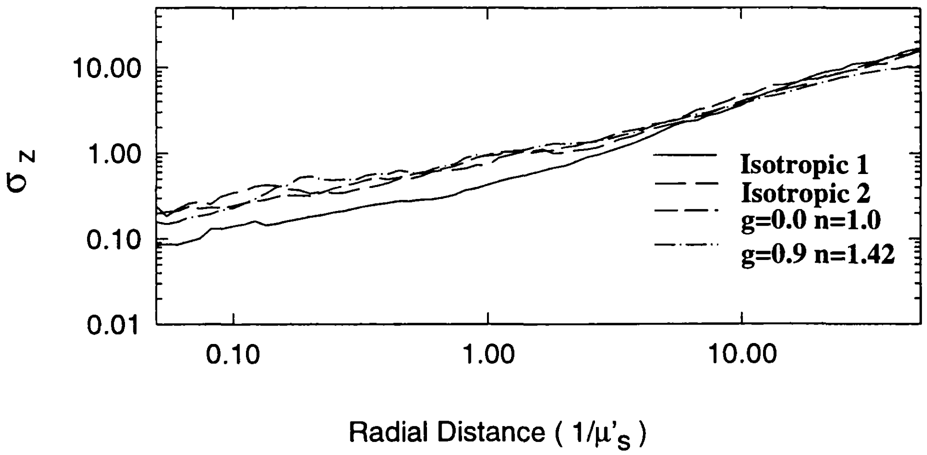

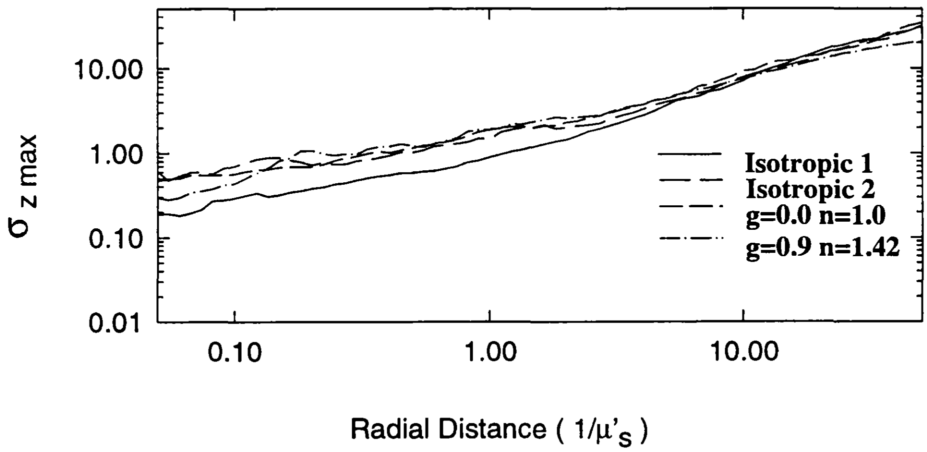

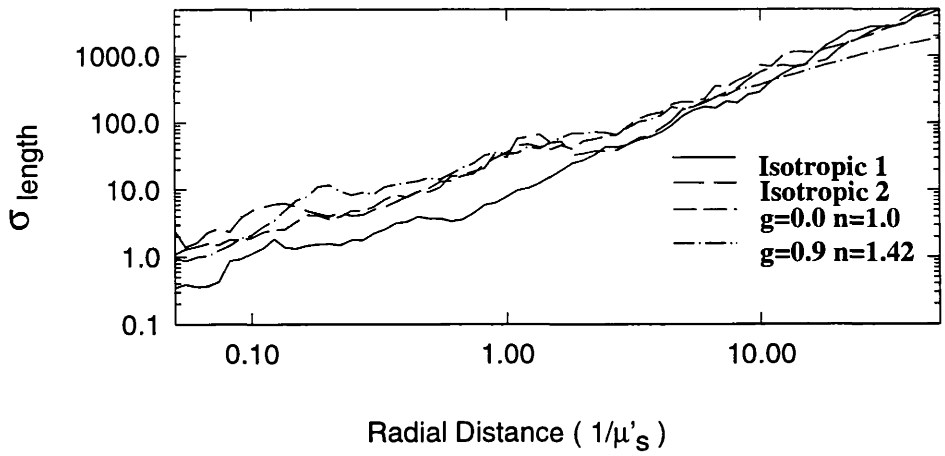

Figure **4.15** The standard deviations for a photon of; the mean depth of travel (top), the maximum depth of penetration (middle), and the path length taken (bottom), versus entrance-exit distance.

Each graph shows data for two particular cases labelled *Isotropic 1* and *Isotropic 2*. The former is for light propagating in the same manner as Bonner's[193] continuum model, ie statistics are recorded for all exiting photons regardless of their exiting angle having been launched from an isotropic point source placed one scattering mean free path below the surface which does not include a refractive index mismatch. The scattering steps were taken from a Poisson distribution with scattering angles obeying an isotropic phase function. The latter case is identical to the former except that the source function was changed to an infinitesimally wide collimated source normal to the surface. A comparison can be made between this case and the one annotated with g=0 and n=1.0 which, like the rest of the data, is derived from simulated photons that were backscattered to within 14 degrees of the surface normal when still in the scattering medium. The presence of a difference in these results justifies the computational cost of the latter and the more realistic simulation of the photon paths that contribute to a coherence peak. The trends in the rest of the data showing the effects of the refractive index mismatches and the scattering anisotropy, indicate that they are all in agreement for the long and diffuse paths. There is, however, a marked change in the statistical means at around 3 reduced scattering free paths where they appear to become sensitive to the scattering anisotropy factor. This region, which was shown in the first section of this chapter to be responsible for a significant proportion of the backscattered intensity, shows photons that are not behaving in a diffuse manner. The effects of the refractive index mismatch are more subtle, particularly as the photon paths were terminated on a partial internal reflection. The contribution of photons that continued to propagate from anything other than a total internal reflection were considered to be insignificant and too computationally demanding to account for. Although the refractive index mismatches seem to make little difference to these statistics it should be noticed that in fig 4.3 they are shown to influence the distribution. One possible conclusion is therefore that a refractive index mismatch influences the chance of a particular route in being taken, more than the shape of the route itself.

So far, two particular sets of data have been obtained; one on the relationship between the average maximum depth a photon penetrates and the

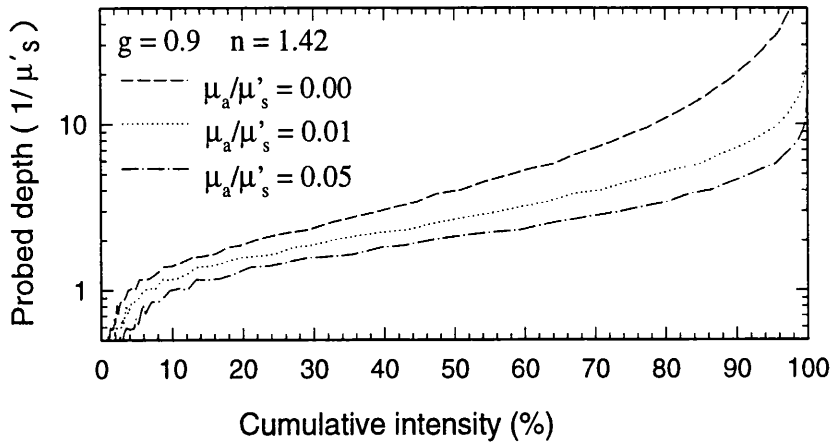

Figure **4.16** Estimates of the probing depth within which the respective percentage of the total backscattered intensity will have been confined during its propagation in the scattering medium.

radial distance at which it exits, and then another describing the radial distribution of the backscattering light. It is possible to combine these to make an estimate of the distribution of the photon penetration depths for all the light that gets backscattered from an infinite half space. This is defined in this study as the probed depth. When absorption data is included, the simplification is made that whilst the absorption influences the chance of a photon propagating and exiting at a particular position, the average maximum depth that the photon penetrates is independent. This argument is clearly invalid for very long paths but can be argued to become less and less important as the paths become shorter and shorter. It is assumed that in the range of albedoes present in biological tissue, this simplification will result in a minimal amount of over estimation. The data shown in fig. 4.16 can be interpreted as the maximum likely depth within which the corresponding percentage of the total backscattered light will have passed in its travels. The results imply that for biological media with values of μ_a/μ'_s between 0.01 and 0.05, 63% of the light is backscattered without having penetrated further than 2.5 to 3.5 reduced scattering mean free paths into the tissue. This range is extended to between 5.5 and 10 reduced scattering mean free paths for 95% of the backscattered light.

4.3 MOST LIKELY PATH PATTERNS.

A comprehensive list of analytical solutions giving the shapes of various photon path distributions (bananas) has been given by Arridge *et al.*[195] 1992. An elegantly simple treatment to solve the same problem for an infinite half space by Monte Carlo simulations and perturbation theory was given by Feng *et al.*[196] 1993. None of these studies however considers the specific behaviour of the very short paths that account for the majority of the light backscattered from a biological medium, which as this work shows, is sensitive to a significant degree on the photon source function, the scattering phase function, and the refractive index mismatch at the boundary.

The approach taken here extensively exploits the cylindrical symmetry of diffusing light and a theory of reciprocity. The process starts with simulating light

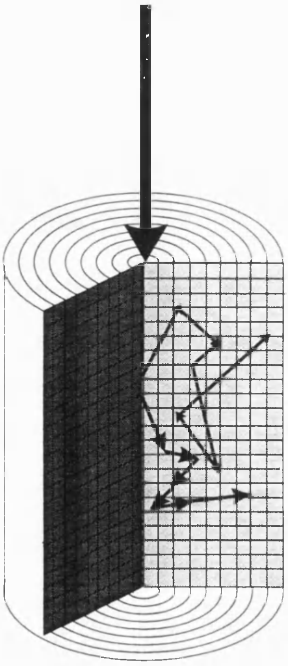

Figure **4.17** Cylindrical coordinate system used to record photons for the fluence rate patterns.

transport from an infinitesimally wide collimated beam, incident on a half space along the surface normal, with a refractive index mismatch. The Monte Carlo model is based on the program described earlier in section 1.1. but is adapted to produce the fluence rate pattern by recording the photon interactions in a picture array representing a cross section of the cylindrical coordinate system, see fig. 4.17. The distance between each photon interaction is taken from a Poisson distribution weighted by the extinction mean free path (in this study the reduced scattering coefficient was set at unity and the absorption coefficient at 0.001. As the absorption is negligible compared to scattering, all photon interactions will be referred to as scattering interactions). The value placed in each radial voxel corresponds to a photon weight that is equal to the term W/V, where V is the volume of the radial voxel and W is the photon weight = $PWR\ a^n$. Here n is the number of photon interactions so far, a is the albedo, and PWR is the photon weight that has been decreased from unity according to the possible reflections at the tissue-air interface. A photon's propagation is allowed to continue until the photon weight term falls below 0.0001 whereupon a Russian Roulette system is played which randomly increases one in ten of the photons weights by a factor of ten, and terminates the path of all the others. Once the pixel values have been ~~summated~~ summed for many simulated photon lives, the value in each pixel is proportional to the density of the photon scattering interactions and the overall picture representative of the intensity distribution. Figs. 4.18 and 4.19 show the intensity distributions on a natural logarithmic scale that arise from an infinitesimally narrow beam incident on a half space for two values of refractive index mismatch and two values of g. The plot shown in the top of fig. 4.18 uses an analytical solution of the diffusion approximation by Eason *et al.*[192] which models the source function as an exponentially distributed line source. The top of fig. 4.19 represents a similar treatment by Cui and Ostrander[197] but using an isotropic source embedded in the medium as the source function. These two approaches can be considered to simulate the situations where g is set at around 0 and 0.9 respectively. The nature of an infinitesimally wide beam is such that none of the pixel values along the axis of injection are truly representative of the exact intensity. The values in each of these figures are normalised with respect to the intensity found in the respective picture at the point 3 reduced scattering mean free paths along the radial axis from the point of illumination and 3 reduced scattering mean free paths below the surface. This normalisation method was chosen as it highlights the differences near the source functions.

If it is assumed that the flux in each pixel is diffuse, then an alternative interpretation of the pixel values is that they are proportional to the probability that having been launched in a collimated beam normal to the surface at the origin, the photon will be scattered at some time within that pixel. As the simulation is concerned with photon paths it is possible to reverse the situation and say that the pixel value is proportional to the probability that the photon, having been scattered within this pixel, continues to propagate until it exits at the origin along the axis normal to the surface. This sink function closely models the real life situation of light that is involved in the production of a coherence peak. If the radial distribution is replicated, the picture shifted across on top of the original and the newly aligned pixels in two pictures multiplied together, then a form of convolution is performed. The result of this convolution is a picture in which a particular pixel value represents the probability that the photon, having been launched along one line normal to the surface, is scattered in that pixel before going on to exit along another line normal to the surface. The overall distribution therefore gives the density of scattering interactions for light that propagates between the two points separated by a distance equal to the shift made in the convolution. The viewing plane is the one that contains the two parallel entrance and exit lines. As with the fluence rate plots, these distributions are not accurate very close to the lines of entrance and exit where the infinitesimal source function has not been truly represented, nor in any other regions where the photon flux can not be considered to be flowing in all directions (e.g. very close to the surface where photon paths will only be in the direction away from the medium) The distributions shown in figs. 4.20 and 4.21 shows the convolution results of the distributions shown in figs. 4.18 and 4.19 with a separation of 3 reduced scattering mean free paths. This distance corresponds roughly to the median exiting distance for light backscattered from a biological medium, see section 1.1 of this chapter.

The results shown for the fluence rate distributions in the middle and bottom of figs. 4.18 and 4.19 indicate that the presence of a refractive index mismatch is to increase the fluence rate just below the surface. This follows intuition if one considers that a photon travelling towards the surface is more likely to be reflected at the surface and carry on its propagation if there is a large refractive mismatch present. The inverse proportionality of the scattering anisotropy factor on the length of the source line is also visible. Comparisons between the path distributions for different values of scattering anisotropy factors show that the isotropic scattering tends to launch the photons quite some way into the medium before the journey towards the exit point starts (a distance equal to a reduced scattering mean free path). This implies that the average maximum depth of penetration and the mean of the average photon depth, are likely to be larger for isotropic scattering than anisotropic scattering, and that for isotropic scattering the means are likely to converge towards 1 scattering mean free path as the entrance to exit distance is reduced. This is contrary to the zero figure implied by diffusion theory if the restriction to highly scattered light is ignored (Feng *et al.*[196] 1993 deduces that the most likely path in a low absorption medium reaches a maximum depth proportional to $\rho/\sqrt{2}$ where ρ is the entrance to exit distance). This phenomenon is also shown in the photon statistics of section 2.1 of this chapter.

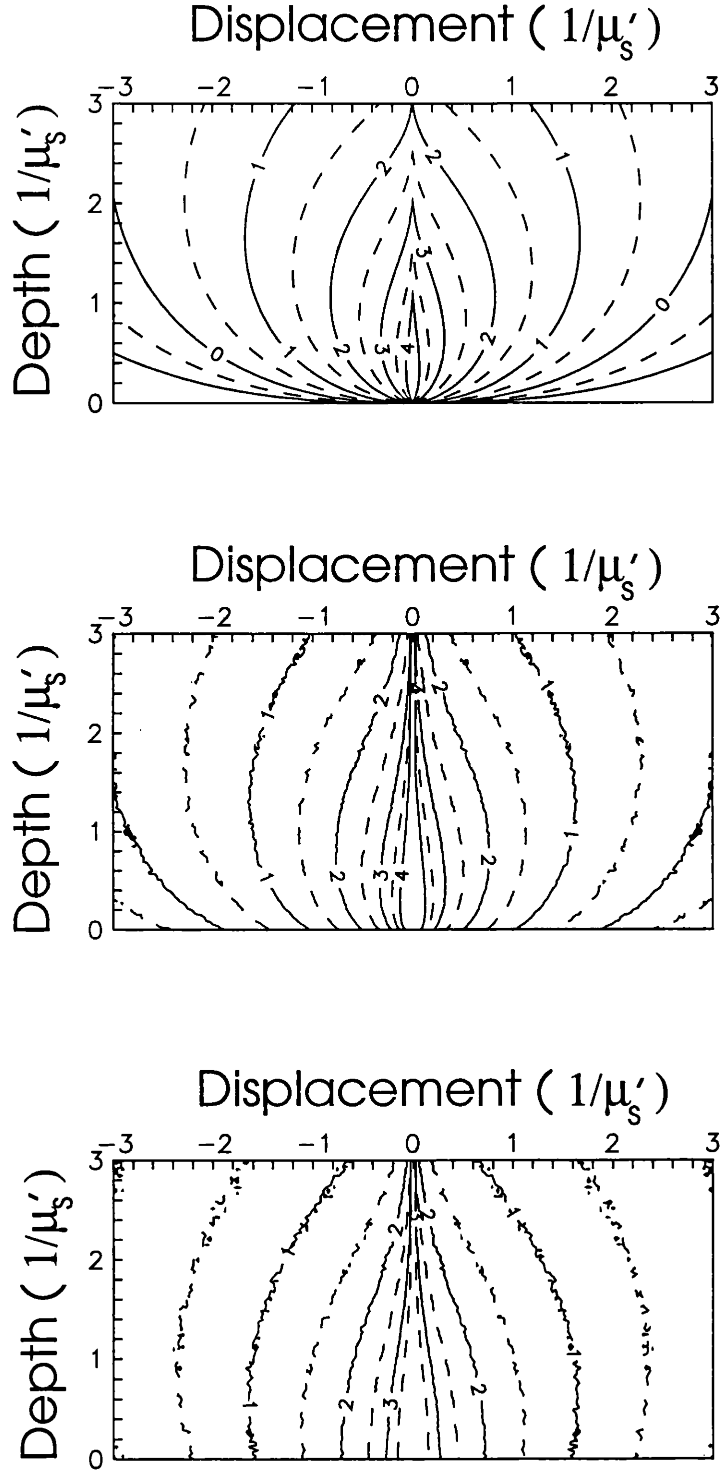

Figure **4.18** Fluence distributions for narrow beams incident on infinite half spaces. top:- Analytical solution by Eason, middle:- Monte Carlo for g=0 & n=1.0, bottom:- Monte Carlo for g=0 & n=1.42. (Ln scale for contours)

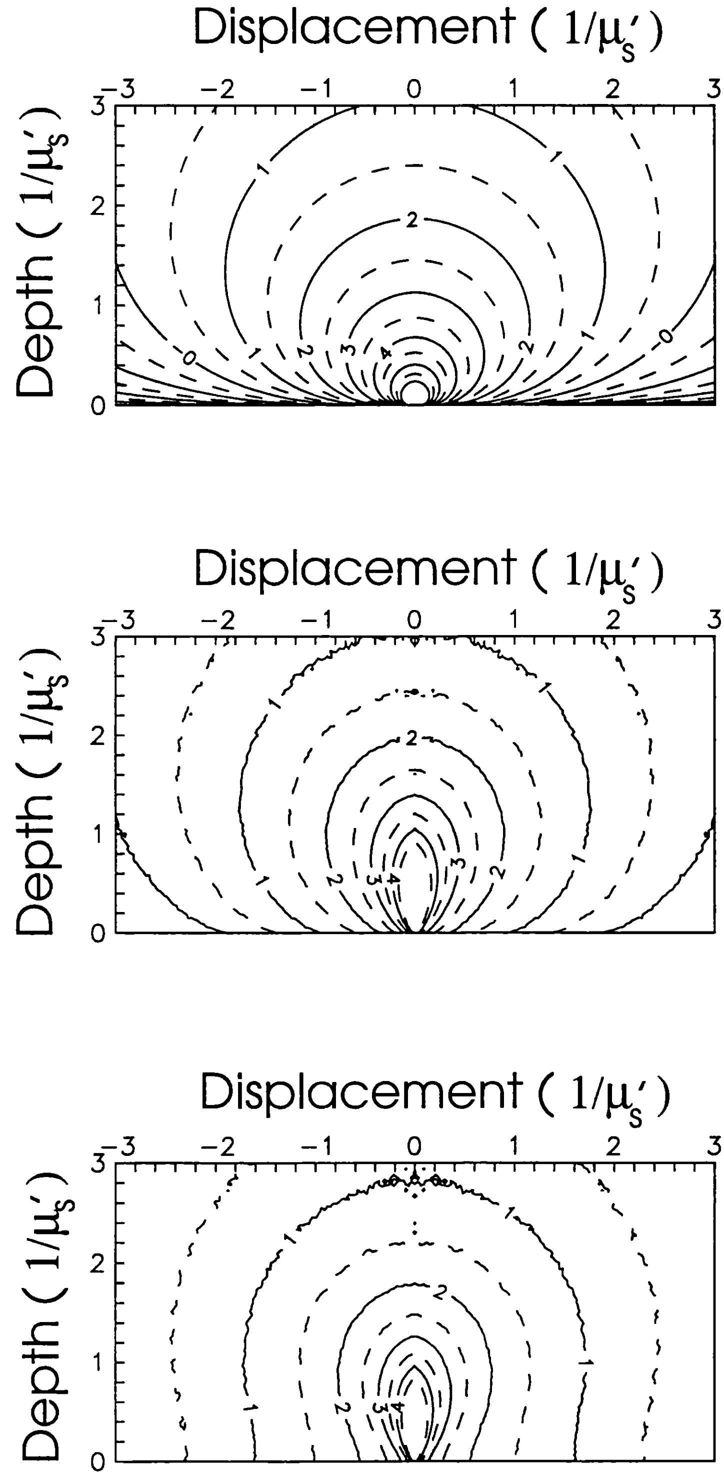

Figure 4.19 Fluence distributions for narrow beams incident on infinite half spaces. top:- Analytical solution by Cui, middle:- Monte Carlo for g=0.9 & n=1.0, bottom:- Monte Carlo for g=0.9 & n=1.42. (ln scale for contours)

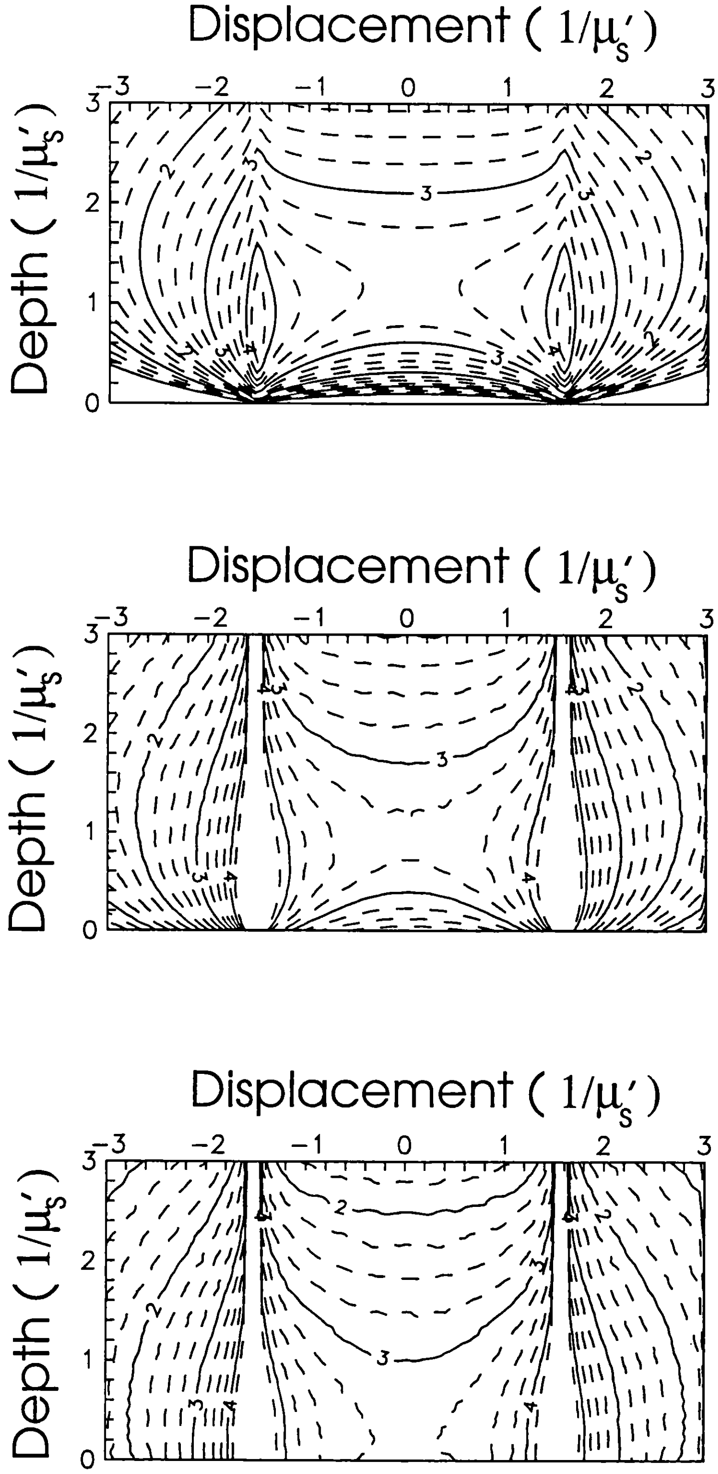

Figure **4.20** Density of scattering interactions for backscattered light. Derived from top:- Analytical solution by Eason, middle:- Monte Carlo for g=0 & n=1.0. bottom:- Monte Carlo for g=0 & n=1.42. (Ln scale for contours)

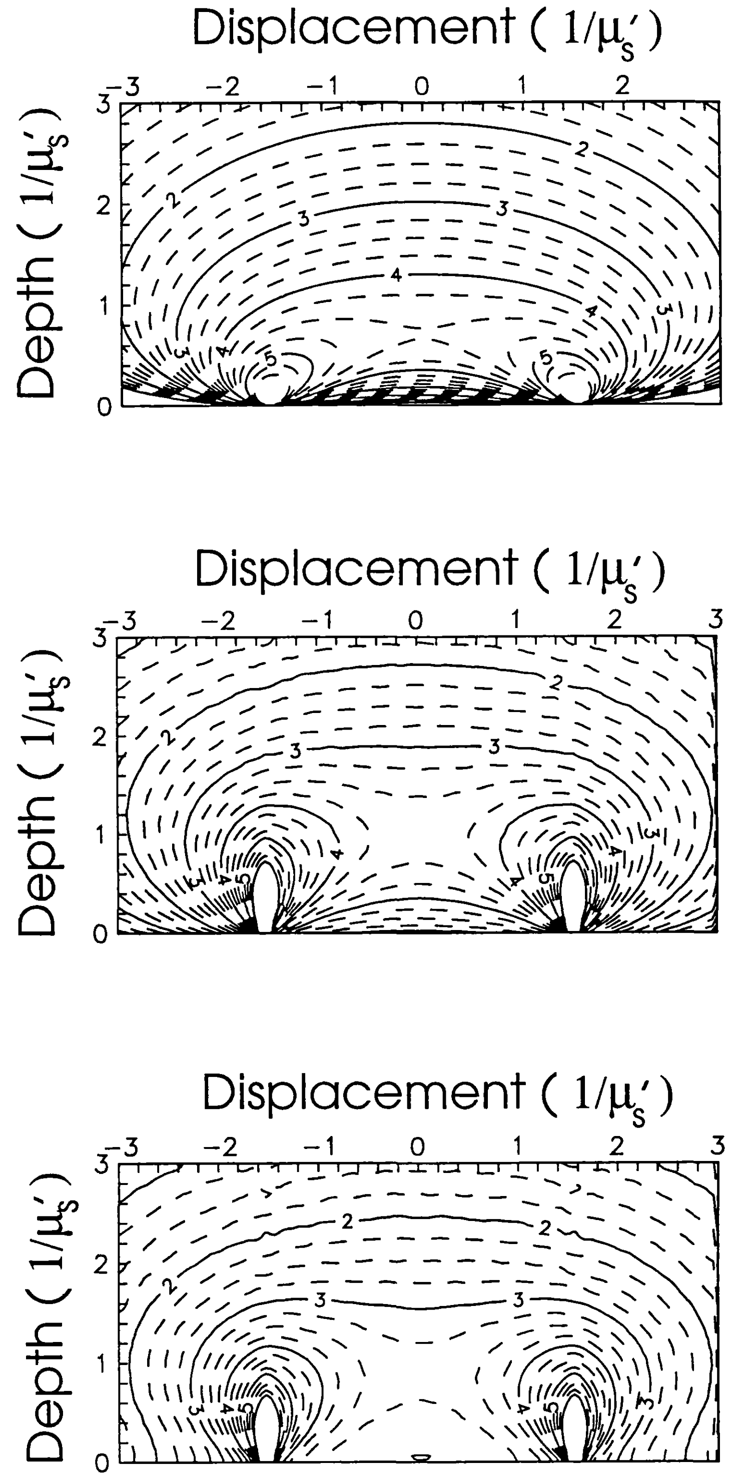

Figure **4.21** Density of scattering interactions for backscattered light. Derived from top:- Analytical solution by Cui, middle:- Monte Carlo for g=0.9 & n=1.0, bottom:- Monte Carlo for g=0.9 & n=1.42. (ln scale for contours)

4.4 CHAPTER SUMMARY.

This chapter has shown that a significant number of photons are backscattered from a biological medium before they start behaving diffusely and that their behaviour has not, as yet, been described adequately by any analytical mathematics. The indications are that most of the backscattered photons exit within a few reduced scattering mean free paths of their point of entrance and have not usually penetrated very far into the medium. This would indicate that the coherent backscattering technique samples thinner layers of tissue than the conventional techniques with what is likely to be a high resilience to the artifacts caused by inhomogeneities.

CHAPTER 5

COHERENT BACKSCATTER.

5.1 ELEMENTARY THEORY.

5.1.1 Anderson or Strong Localization.

Although this does in theory exist for photons, its main application is for electrons where their propagation through a medium may be significantly altered by changing an electric field. The Anderson localization regime is approached when the mean free path of the scattering particle between interactions is so short that the free area between them is less than the scattering cross sectional area. This combined with interference effects results in a significantly high probability of the paths becoming loops. The existence of many paths being loops of constructive interference creates self consistent random cavities which results in a zero diffusion constant and a so called ‘white hole’. This regime has been approached with the experimental observation of a small proportion of the photons being backscattered out of a medium with coincident first and last scattering positions. This phenomenon of looped type photon trajectories is known as recurrent scattering[198-200].

5.1.2 Angular-resolved backscattering with Weak Localization.

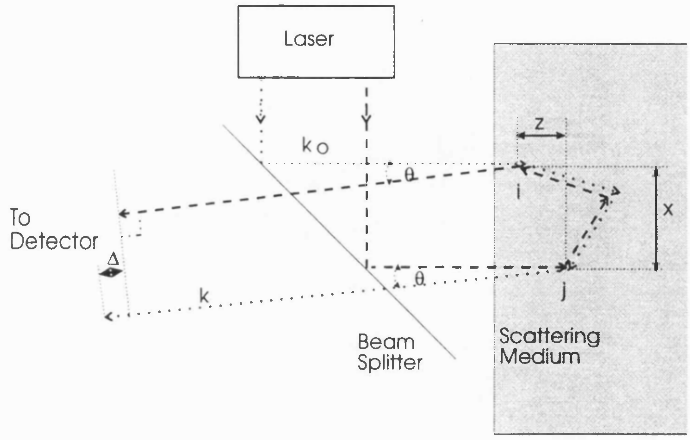

Figure **5.1** Coordinate system for backscattered light showing the phase shift responsible for the coherent backscatter effect.

If the mean free path of the photon is not short enough to create Strong Localization then we may be in the regime of Weak Localization. Referring to fig. 5.1, consider the two photon paths shown. They both follow the same series of scattering events between the scattering centres ***i*** and ***j*** but in the reverse order from each other. On emerging, the photons follow parallel paths at an angle θ to the axis of incident light until a lens placed at a focal length away from a detector brings them together at a point, the position of which is dependent on the emergent direction. The phase difference between the photons at the detector, Δ, is proportional to the difference in path length for the two routes. This is dependent on the angle between incidence and backscatter, and the relative positions of ***i*** and ***j***, but not the actual path taken between them.

The equation used to derive the steady-state angular intensity profile, α, for multiply scattered light can be expressed as;

$$\alpha = \sum_{\substack{all \\ combinations \\ of\ i,j}} \; \sum_{\substack{all \\ paths \\ i \leftrightarrow j}} A_i^2\, \delta_{ij} + A_j^2\, \delta_{ij} + 2\, A_i\, A_j\, \delta_{ij} \cos(\Delta) \qquad \textbf{(5.1)}$$

where the propagator term, δ_{ij}, is the factor by which the photon density falls along the particular path between the possible first and last scattering points ***i*** and *j*. The terms A_i and A_j represent the amplitude of the light field at the respective points, which is in turn proportional to the square root of the local photon density. The phase term, Δ, is given by the expression;

$$\Delta = (\boldsymbol{R}_i - \boldsymbol{R}_j).(\boldsymbol{k}_o + \boldsymbol{k}) = \frac{2\pi n}{\lambda}[\ x \sin\theta + z\,(1-\cos\theta)\ ] \qquad (5.2)$$

where n is the refractive index of the medium, λ is the wavelength of the light *in vacuo*, k_0 is the incident and k the emergent wave vector with angular separation θ within the medium, and $(R_i - R_j)$ is the vector between points i and j with cartesian components x and z.

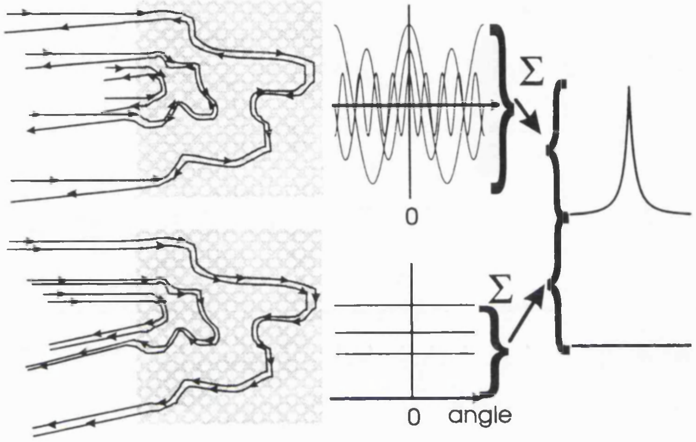

Figure **5.2** The elementary process that produces coherence peaks.

Fig. 5.2 shows diagrammatically the sequence that makes up a coherence peak from multiply scattered light. On the top left is shown the time reversal scattering which gives rise to the *cos* term shown in equation 5.1, whilst the two squared terms (the angle independent terms) describe the classical scattering situation shown at the bottom. As θ increases, the contribution of the time reversed paths oscillate giving rise to the profiles seen in the middle. Situations where the points i and j are close tend to produce angular oscillations with larger periods than when the points are more distant. If these profiles are weighted by their probability of existing, and then summed for all possible first and last scattering particle combinations, the classic coherent backscattering cone is formed as shown on the far right.

This means that the general shape of the coherence peak is such that the full-width-half-maximum is proportional to the reduced scattering coefficient whilst an increase in the absorption coefficient creates a rounding off of the peak and a slight increase in the full-width-half-maximum. The ratio of the reduced scattering coefficient to the absorption coefficient has a strong effect on the incoherent backscattered intensity relative to the input power. The aim of this work is to extract the reduced scattering and absorption coefficients by analysing the shape of the coherence peak and the backscattered power level.

In order that this scalar theory can be applied to the vectorial nature of light it is necessary to polarize the incident light in the same state as the light that is detected and preferably in a circular state[200-202]. Circularly polarized light has properties such that its helicity is reversed on a specular backreflection. This means that placing circular polarizers in the incident and emergent beams will eliminate the detection of any specular reflections from the refractive index mismatch at the surface and any single backscattering events from the scattering structure. The former would create a chaotic pattern if the surface was rough whilst the latter would manifest itself as an angular independent term which when added to the backscattering profile, would result in a maximum enhancement ratio below the ~~optimum~~ maximum factor of two.

It is important to make the distinction at this point between the interference effect described above as coherent backscatter, weak localization, or coherent enhancement, and the non interference effect known as retro-reflection which is included in the more general term of enhanced backscatter[203]. Retro-reflection arises from scattering structures that have a tendency to backscatter light in certain favourable directions e.g a car reflector made up of an array of prisms (as with many examples, it is possible in this case to additionally observe a coherent backscatter effect due to the possibility of time reverse paths but on a very much smaller scale). The intensity profile of a retro-reflectance enhanced backscattering phenomenon does not follow the same general shape as a coherence peak, normally exists over a much larger angular range, and for scattering/reflection and absorption properties that are constant across the light spectrum, is independent of the illuminating wavelength.

5.2 LITERATURE SURVEY ON COHERENT BACKSCATTERING.

The underlying phenomenon responsible for this effect was first introduced by P.W. Anderson[204] in 1958 as Localization and has been mainly investigated in the realms of Photon and Electron propagation[201,205-207] although in theory it is applicable to any wave. The electron propagation realm has received the most attention due to its implications in condensed-matter physics[208].

Restricting this survey now to photon transport only, the basis of radiative transfer theory as originally attributed to Schuster[209] in 1905, was first extended to include interference effects over multiple mean free paths and discussed by de Wolf[210] in 1971. The driving force amongst theoreticians has been to achieve complete Anderson Localization, also known as Strong Localization, which will result in a so called 'White Hole'[211] where the region experiencing strong localization will appear from the outside as a perfect reflector whereas the light inside will be totally trapped. A common approach to achieve this aim is to obtain a perfect theory for weak localization and then attribute any differences between that theory and any experimental results for very short mean free paths as being the critical effects of strong localization. The first observation of a weak localization enhancement cone, or coherence peak, was by Kuga and Ishimaru[212] in an aqueous suspension of micro Latex spheres. The shape of the enhancement cones observed in these experiments was smoothed by the limited angular resolution of the equipment used but this was later improved[213-215] and gave evidence which supported the theoretical predictions of the line shape made by Tsang and Ishimaru[216,217] in 1984 and 1985. It should be noted at this point that coherence peaks can be obtained whenever the possibility exists of time reversed paths. This includes occasions other than the backscatter from turbid media, such as multiple surface reflections[218-220] or double passages through turbulence[221].

A diffusion approximation derivation which allows a correction to be introduced to compensate for anisotropic scattering and absorption was developed by Akkermans *et al.* in 1986[202,222]. Despite the limitations of the diffusion equation to cases where there are many scattering events, hence its restriction to low absorption cases, plus its sensitivity to boundary conditions (particularly refractive index changes and complex geometries), the scalar equation has been frequently used due to its simplicity and supposedly sufficient accuracy[223]. The theoretical

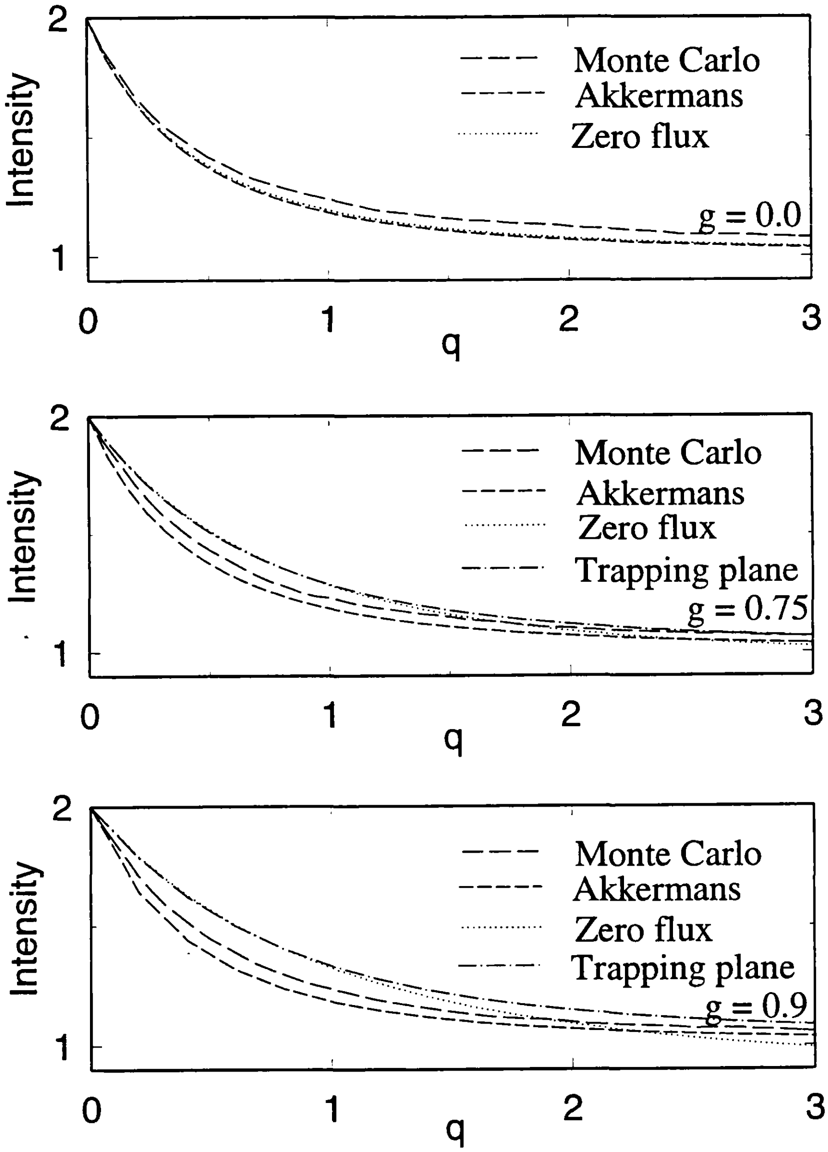

Figure 5.3 A comparison between some different predictions for the coherence peak line shape with various values of **g**. top:-isotropic, middle:-g=0.75, bottom:-g=0.9.

and experimental evidence of the importance of internal reflections has been given by Lagendijk *et al.* 1989[224] Freund and Berkovits 1990[225], Zhu *et al.* 1991[226], Saulnier and Watson 1992[227], Nieuwenhuizen and Luck 1993[228], Durian 1994[229], and den Outer 1995[203]. All show that higher values of reflectance reduce the full-width-half-maximum of the enhancement cone. Numerical studies by Ospeck and Fraden 1994[230] take this phenomenon further and simulate the effect of a thick glass window on the boundary. The results show that a kink in the backscattering profile exists at an angle inversely proportional to the wall thickness. Beyond this kink angle the cone shape behaves as though there are no internal reflections, whilst below, the cone narrows as expected[+].

Gorodnichev *et al.* 1990[231,232,++] gives an exact solution for the coherence peak line shape for an absorbing and scattering medium but only for isotropic scatterers without a refractive index mismatch at the boundaries. This overcomes the problems of the single and double scattering theory (that of Tsang and Ishimaru 1985[217]), and the diffusion approximation problem of only being applicable to highly scattered events, the latter problem manifesting itself as inaccuracies in the 'wings' of the cone. A similar treatment to Gorodnichev *et al.* but for cases with weak, linear, anisotropy was performed by Ozrin in 1992[233]. This paper confirms the diffusion approximation assumption[202,222] that the solution holds if the scattering mean free path is replaced by the reduced scattering mean free path. Recent work by Amic and Luck[234] has suggested that in the experimentally implausible limit as the anisotropy factor approaches 1, the full-width-half-maximum is in fact proportional to $\sqrt{(\mu_s \mu_s')}$. A demonstration of the dependence of several established theoretical predictions on anisotropy and boundary conditions was given by Barabanenkov and Ozrin 1991[235], with the conclusion that the effects are significant and that the different solutions are not in agreement for highly forward scattering media. Fig. 5.3 shows a similar

---

[+] It should be noted that in this study the dimensions of the glass slide, when used, are such that it will for the degree of scattering and absorption present in the experiments, behave as a one single refractive index mismatch equal to the difference between the glass and air.

[++] ref 231 contains a significant typographical error not seen in ref 232 comparison between Akkermans' diffusion approximation solution, Barabanenkov's two solutions[235] (one for the case where the boundary condition was a zero flux model and another for a trapping plane model), and finally the Monte Carlo method of this study. For the isotropic case, Gorodnichev's solution[232] and Barabanenkov's trapping plane model appear to be coincident with the Monte Carlo method and the zero flux model respectively and have therefore been omitted for clarity. The abscissa is the same normalised angle term used for the results presented later and is defined in equation 5.7.

Further experiments went on to show that some backscattered cones were in fact asymmetric which was attributed by the observers, van Albada, van der Mark and Lagendijk[236] (1987), to the low-order Rayleigh scattering that was taking place. A Monte Carlo model was then developed by the same group to validate this theory[237]. Additional work on Monte Carlo simulations within the Mie scattering regime has been carried out by van Albada *et al.*[238,239] and in order to investigate the Faraday effect by Martinez[180]. Much of the experimental work around this time[240,241] included time dependent theory using pico-second light pulses and various slab geometries to determine the limits of the diffusion equation and complements the work of Etemad *et al.* in 1987[242] who experimentally compared the similarity in the effects of absorption and limited slab thicknesses. This latter paper was the first to attempt extraction of absorption information from samples by comparing the line shape of the peak to those obtained with phantoms of identical scattering properties but with zero absorption.

The only attempt to model the effects of a finite illumination profile has been by Ospeck and Fraden 1994[230] where they numerically modelled a top hat profile. This prevents certain long scattering paths from contributing to the enhancement peak by preventing the possibility of the reverse path from being taken. The effect, like the work of this study on Gaussian profiles, was shown to be a decrease in the peak enhancement over the background intensity level.

The first use of the coherent backscatter phenomenon with biological scatterers was made by Yoo *et al.*[243,244] (1990) who used pico-second pulses to determine photon path lengths in a very similar way to his previous work on non biological diffusers[245,246]. Yoo *et al*'s work on the biological specimens made comparisons with diffusion approximation solutions for the coherence peak line shape and came up with absorption and scattering coefficients which were described as 'similar' to results from conventional techniques.

This interest in biological tissue was taken up again by Yoon *et al.*[247] (1993) who used a CW laser with a spot size of a few millimetres, and a CCD camera detection system along with diffusion approximation theory to measure the reduced scattering and absorption coefficients for several *in vitro* tissues. Comparisons were made with data derived by the adding-doubling method of extracting the coefficients from reflectance and transmission measurements made with integrating spheres[144]. The results were within likely inter-sample variations for scattering coefficients but in error by a factor of six on the absorption coefficients. It is our belief that more accurate absorption information would have been achieved if the effects of the finite size of the illuminating beam had been included rather than the inaccurate interpretation of Akkermans' formula[222,+++]. The major landmark in this paper was the attempt to use the equipment *in vivo* on a human forearm. Here it was found that there was no need to rotate the sample to obtain the ensemble or moving averaging that is necessary to remove the speckle pattern from a fixed scattering structure[248]. The *in vivo* averaging was instead obtained by the pulsatile vibrations present in all living tissues. It was suggested in the paper that a significant improvement may be obtained by using a theory other than the scalar theory of Akkermans *et al.*[202]. The improved theory would encompass the refractive index mismatches and overcome the diffusion approximation's restriction to high scattering and low absorption situations. This thesis reports the development of a Monte Carlo model that takes all of these factors into account plus the ability to simulate the effects of non uniform illumination profiles, anisotropic scattering, and if needed, can be extended to include inhomogeneities.

[+++] The equation used appears to have been derived by taking Akkermans' formula for the coherent enhancement of infinitely extending plane waves, which varies in magnitude with absorption, and then adding an incoherent intensity which corresponds to the enhancement that is obtained in exactly the backward direction but with zero absorption rather than with the absorption used to calculate the enhancement.

5.3 GENERATING COHERENCE PEAK LINE SHAPES WITH MONTE CARLO INFORMATION.

5.3.1 Theory.

The approach taken to generate a Coherence Peak line shape was to process a data base of photon histories with equations 5.1 and 5.2 for an array of angles. The data base was generated using the Monte Carlo simulation described and validated in chapter 4. Each photon history contains information for a backscattered photon such as the position of the last scattering point relative to the first, the path length taken within the medium, and the cumulative effects of reflections at the interface. As the distances were all recorded in terms of mean scattering free paths it is possible to simulate the effects of different scattering and absorption coefficients by scaling all the distances by the factor: l_s ($=1/\mu_s$), and assigning a total photon weight or the propagator term in equation 5.1, δ_{ij} as;

$$\delta_{ij} = PWR\, e^{-\mu_a d} \tag{5.3}$$

where d is the total path length of the photon having been scaled by l_s, and **PWR** is the photon weight as decreased by Fresnel reflection losses. Incorporating the nonuniform beam illumination was achieved by scanning the initial scattering position across the beam profile and calculating the amplitude terms at the entrance and exit points accordingly. The effects of a non perfect experimental system response, mainly the divergence of the laser and any focusing errors, can be achieved by numerically convoluting the output of the Monte Carlo processing program with a Gaussian profile representing the spot the experimental system records from a specular reflection off a flat plate in place of the backscattering sample.

The individual data bases created contained 40,000 photon histories for a fixed combination of refractive index mismatch and anisotropy factor, different data bases being generated for the different situations required. This allows a relatively quick computation of a set of intensities for an array of angles specified by any combination of absorption and scattering parameters, at any wavelength under the specific illumination profiles required (generating a data base took a Sun SPARK 10 computer around a week whilst the subsequent processing to obtain the line shape took about 5 minutes).

5.3.2 Results and validation.

For validation of the line shape prediction method we compared the Monte Carlo method with the exact theory of Gorodnichev *et al.*[232] for isotropic scatterers not bounded by a refractive index mismatch and modified in this study to remove the contribution of the single scatter component to the incoherent intensity. The entire coherence peak line shape, for the simplifying case of the relatively weak scattering found in biological tissues and for an illuminating beam that is near to the surface normal, is given in terms of the coordinates used in this study as;

$$\begin{aligned}\alpha(\theta) = \frac{\mu_s}{8\pi\mu_t}\Big(& \left|H\left(1,\frac{\mu_s}{\mu_t},0\right)\right|^2 - 1 \\ & + \left|H\left(\hat{\mu},\frac{\mu_s}{\mu_t},\frac{2\pi|\theta|}{\lambda}\right)\right|^2 - 1\Big)\end{aligned} \tag{5.4}$$

where

$$\frac{1}{\hat{\mu}} = 1 + \frac{\theta^2}{4} - \frac{i\,\pi\,\theta^2}{\lambda\,\mu_t} \tag{5.5}$$

and

$$H(\hat{\mu},\varpi,\upsilon) = \exp\left(-\frac{\hat{\mu}}{\pi}\int_0^{\infty}\frac{1}{1+\hat{\mu}^2\xi^2}\ln\left[1-\varpi\frac{\tan^{-1}(\xi^2+\upsilon^2)^{1/2}}{(\xi^2+\upsilon^2)^{1/2}}\right]d\xi\right) \qquad (5.6)$$

This last function can be considered as a generalisation of a Chandrasekhar *H*-function[104] derived from transport theory. The first line of the equation for the multiply backscattered intensity profile, $\alpha(\theta)$, contains the Chandrasekhar function describing the incoherent component whilst the second line gives the enhancement. The ***-1*** terms are used in both lines to account for the absence of single scattering contributions to both the incoherent intensity and the enhancement. This is as though circular polarizers were being used in the experimental set up. If the polarizers were linear then there would be a single scatter contribution to the background intensity which would necessitate removing the ***-1*** term from the first line.

The following line shapes are, unless stated otherwise, all normalised with respect to the incoherent intensity from a non absorbing medium and have the abscissa term defined as the normalised coefficient q;

$$q = \frac{2\ \pi\ \theta\ n}{\lambda\ \mu_s^{\prime}} \qquad (5.7)$$

where n is the refractive index of the medium, θ is still the angle of emergence within the medium and λ is the free space wavelength. None of them contain any contributions from single backscattering events.

The effects of absorption are clearly evident in fig. 5.4 with the rounding off of the peak, the increase in the full-width-half-maximum, and the reduction in intensity as the absorption increases. The excellent agreement in the shape of the cone can be seen in fig. 5.6 where each of the enhanced components have been normalised with respect to their maximum value at θ=0. The slight ripples seen in the Monte Carlo profiles are the result of not having an infinite number of photon histories to process. It was assumed in this study, that the generalising nature of the neural networks incorporated within the extraction routines smoothed them out sufficiently (see chapter 6). Fig. 5.5 shows the effects of reducing the number of photon histories and indicates that any moderate increase in the data base size would have a negligible effect on the ripples.

Fig. 5.7 shows the effects of a refractive index mismatch at the boundary which agrees well with the trends identified previously[203,224-230]. The effects of anisotropy are somewhat more subtle but a definite trend can be seen in fig. 5.8 displaying the differences between the Monte Carlo predictions and Gorodnichev's exact isotropic solution, which according to the work of Ozrin[233] is also valid in the anisotropic regime. Fig. 5.9 displays the simulated effects of different illumination profiles described mathematically as a Gaussian in accordance with the theoretical profile of a laser operating in the transverse TEM_{00} mode (the mode with the minimum divergence but unfortunately the minimum spot size). Modelling alternative laser mode structures could be achieved but requires incorporation into the model of the phase shifts present across the beam, data that is difficult to obtain experimentally. The reduction in the peak enhancement relative to the incoherent intensity can be understood from equation 5.1; the non-uniformity across the beam profile results in differences between the amplitudes at the extremities of the scattering sequences, the terms $\boldsymbol{A}_{ij}$ and $\boldsymbol{A}_{ji}$. This will affect

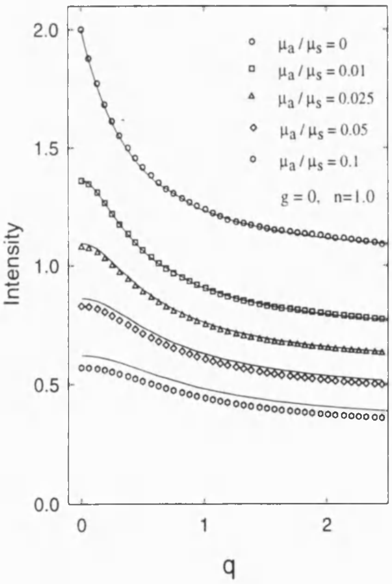

Figure **5.4** The effect of absorption on the absolute intensity profile of a coherence peak. Exact solution is shown by the lines, the Monte Carlo method by the symbols.

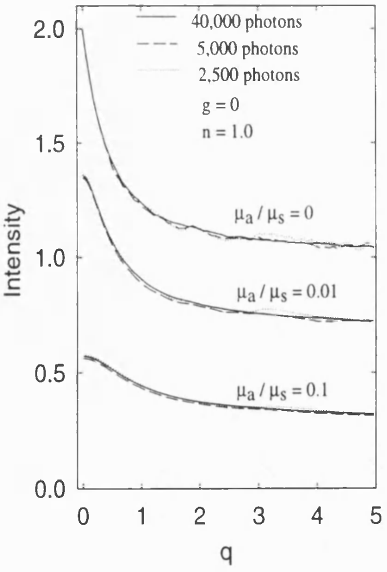

Figure **5.5** The effect of reducing the number of photon histories used in generating the line shapes with the Monte Carlo method for various levels of absorption.

the incoherent term to a larger extent than the coherent term and thus produce the drop in the peak enhancement ratio which becomes more and more significant as the scattering coefficient, the absorption coefficient, or the spot size drops. This effect should not be confused with the smoothing that results from the non ideal system response although it gives similar trends for changes in the scattering and absorption coefficients. This latter effect was modeled by convoluting the Gaussian system response with the predicted line shape in the two angular dimensions; the results are as shown in fig. 5.10.

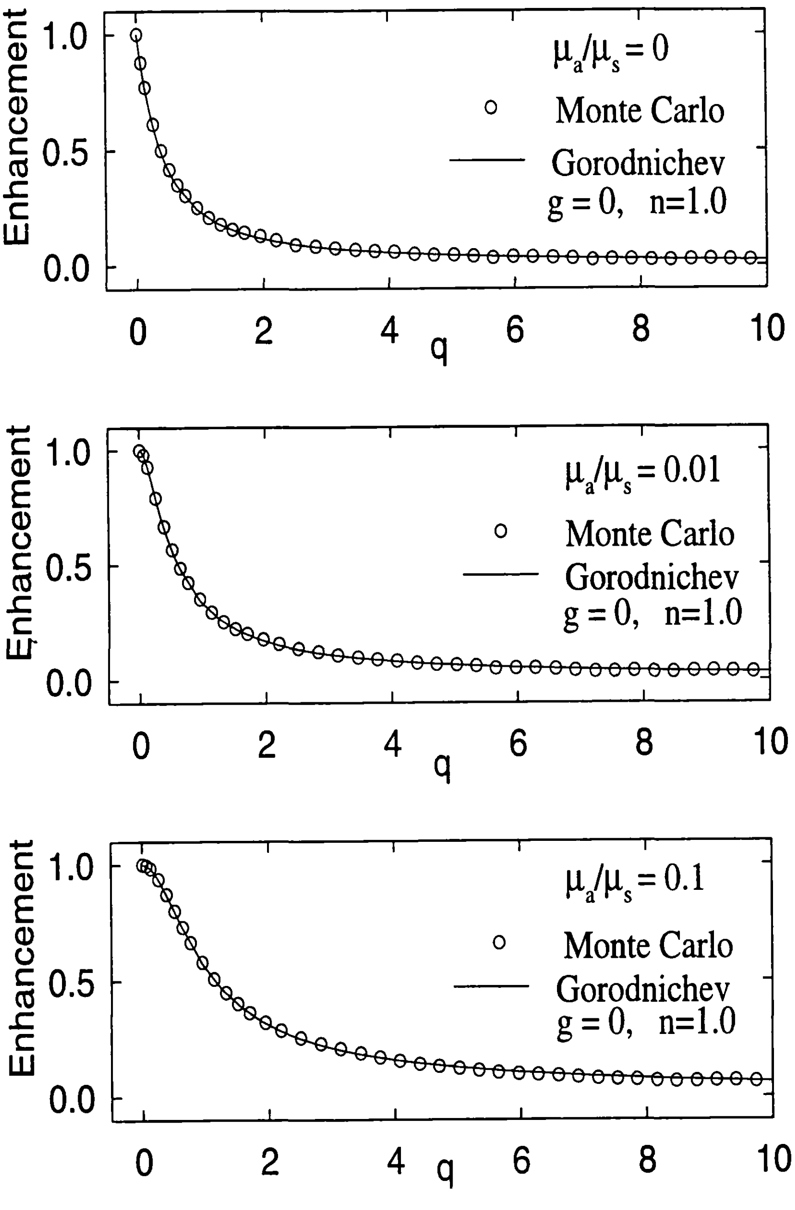

Figure 5.6 The effect of absorption on the enhanced component with respect to the incoherent value of each curve. Exact solution shown by lines, Monte Carlo method by symbols.

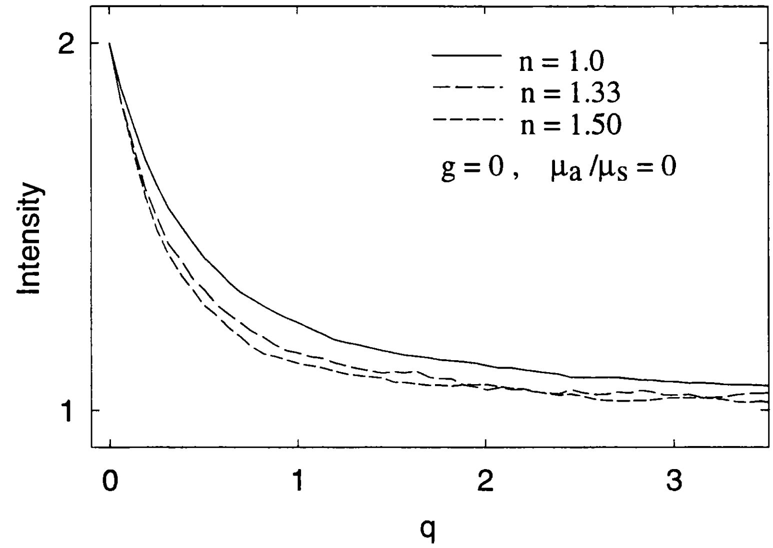

Figure 5.7 The effects of different refractive index mismatches on the Monte Carlo generated coherence peaks.

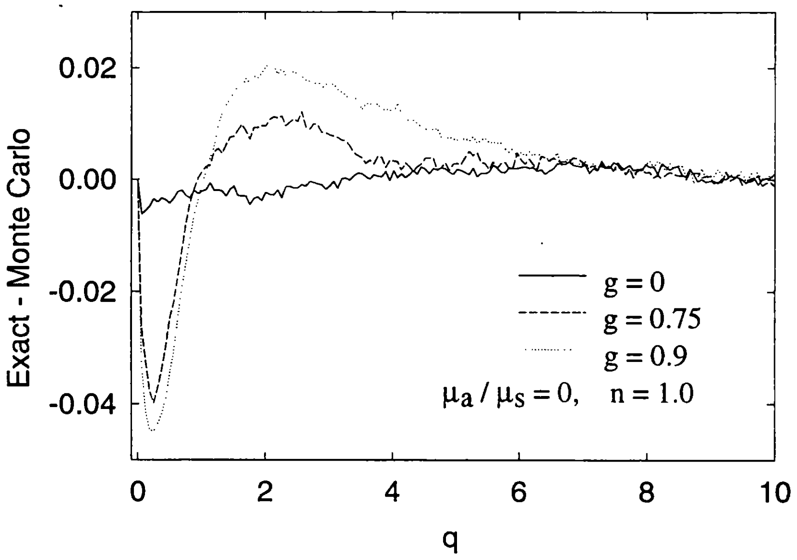

Figure 5.8 The effects of anisotropy on the coherence peaks shown as differences between the exact solution and the Monte Carlo method; μ'_s kept constant.

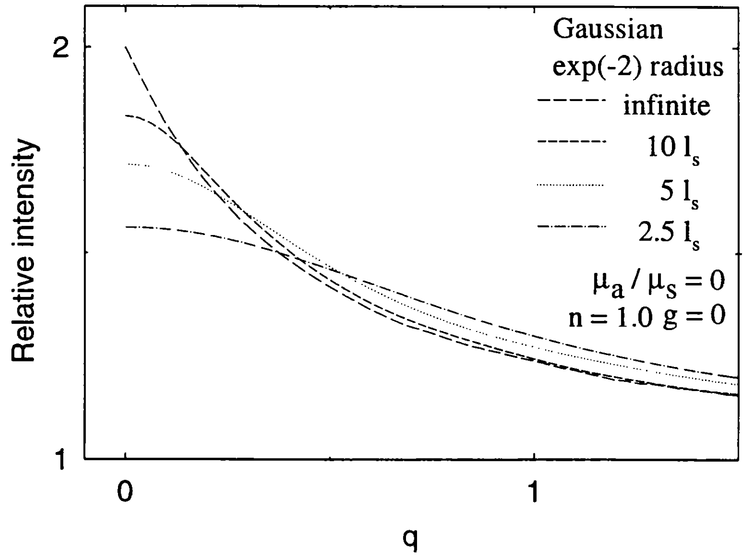

Figure **5.9** The effects of a finite spot size on the coherence peak line shape, normalised in each case to the incoherent intensity level.

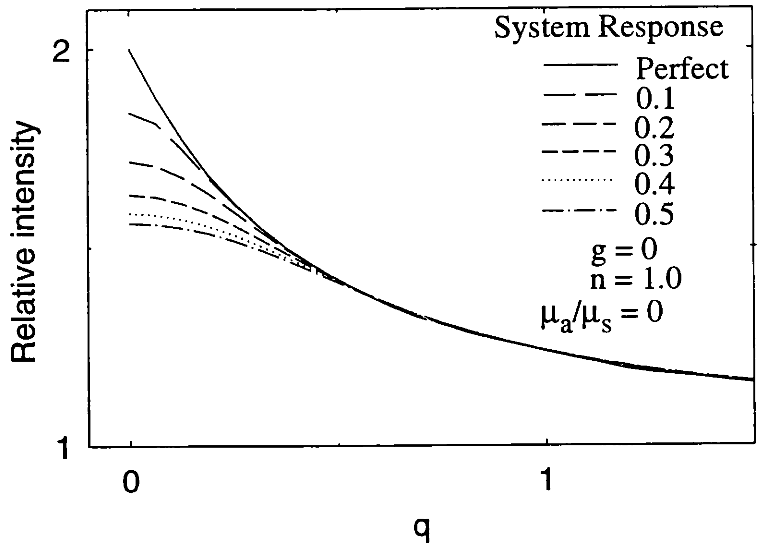

Figure **5.10** The effects of a poor system response on the coherence peaks. System response specified by the $1/e^2$ width of the Gaussian function (units:- q).

5.4 CHAPTER SUMMARY.

This chapter has outlined the history and theory behind coherent backscatter. Previous experiments that have tried to extract optical coefficients from biological media have been discussed and several limitations identified. A new experimental approach that uses information on both the shape and relative intensity of a coherence peak is developed. A Monte Carlo method is used to predict the shape of a coherent backscattering cone as no suitable, exact, analytical solution exists. The Monte Carlo method, when restricted to isotropic scattering in a half space that is unbounded by a refractive index mismatch, gave an extremely good agreement with one possible exact solution. Adding a refractive index mismatch, and scattering anisotropy to the model, gave trends that follow the behaviour predicted by other analytical, but not exact, solutions. It is therefore concluded that the Monte Carlo model is the best possible predictor of the coherence peak profiles that are obtained from biological media. The model has been extended to include the effects of different sized beam profiles and to model the effects caused by a non-ideal experimental systems. Further modifications to the model are possible if the effects caused by inhomogeneities are required.

CHAPTER 6

NEURAL NETWORKS.

"The 1960's saw a great deal of research in neural networks, much of it characterised by a lack of rigor, sometimes bordering on alchemy, as well as excessive claims for the capability and near-term potential of the technology."[249]

The history of artificial networks dates back to the 1940's and has since endured many swings in favour although several land mark progressions, most noticeably the backpropagation learning algorithm, have brought the technology out of the hands of Artificial Intelligence studies and into practice. The quantity and quality[249-252] of recent review articles suggest that the technology has finally passed the necessary acceptance tests and in the hands of the wary can indeed deal with problems that could not be previously addressed. Their usefulness lies in the fact that neural networks have advantages (and limitations) that are often complementary to the conventional computing techniques set down by Babbage, Turin, and von Neumann. Their applicability can be considered in cases where[249];

1) There is ample data suitable for training (examples of inputs and what the output should be).
2) An adequate mathematical model of the function does not already exist.

3) There is a high computation speed requirement.
4) The model produced should be robust to modest levels of noise on the inputs.

The desire in this study was to create a forward function approximator which can learn the inverse function of the Monte Carlo based coherent backscatter line shape prediction program described in chapter 5, section 3.1. It would then be possible to present the experimentally measured coherence peak profile as inputs, and obtain the reduced scattering coefficient and absorption coefficient at the outputs of the neural network. The main advantages of this method include its speed and generalising behaviour. This latter effect means that the small amounts of noise seen in the training data tends not to be learnt, thereby leaving only the overall trends to be incorporated into the mathematical function that the network simulates. This makes it possible for the training data to be obtained from the Monte Carlo processing program without using an infinite number of modelled photons, or by a series of experimentally obtained profiles.

6.1 LITERATURE SURVEY.

The sometimes over-stressed analogy of the simple artificial neuron to its biological namesake lies in the belief that immense computing power can be derived from the networking of a large number of very simple processors, each of which forms a function that imitates the mathematically simple biological neuron. This was first suggested by McCulloch and Pitts in 1943[253] as a possible general purpose computing machine. The first attempts at creating a learning method was devised by Hebb in 1949[254] but the first real successful machine, the Perceptron, is credited to Rosenblatt[255,256]. This machine was made up of a set of photoreceptors linked to an array of potentiometers which in its training phase were driven by motors controlled by the Perceptron Learning Algorithm[256] (PLA).

The successful function implemented was to interpret the pixeled image from the photoreceptors as different characters. Rosenblatt also showed that if the Perceptron could indeed learn a particular function, then the PLA will teach it to do so to within a defined accuracy within a finite number of steps. From here the scientific debate on the usefulness of neural networks continued through to the 1980's when the Error Backpropagation Learning Algorithm[257] (EBLA) was discovered and overcame some of the limitations shown by the PLA.

The role of neural networks within medical physics starts with the radiological image classification work of Boone *et al.*[258] in 1990 which contained as an appendix, a summary of the relevant equations needed to implement a neural network. These equations were referenced by Farrell *et al.*[259,260] in their work on mapping spatially resolved diffuse reflectance measurements into optical coefficients. Similar studies were undertaken with spatially resolved diffuse transmission measurements by Kienle *et al.*[261,262] which was then extended to diffuse reflection measurements on *in vivo* tissues and most importantly with multi layered media[164]. In this last study, the neural network was trained with the results from Monte Carlo simulations of light propagating through a two layered medium with fixed geometric dimensions but various combinations of optical parameters. The technique was shown to work up to the limitations imposed by the equipment sensitivity and inhomogeneites other than those associated with the layered structure. It is hoped that the coherent backscatter approach will overcome these restrictions by its use of light that has not penetrated very deeply and the fact that its sensitivity increases with the scattering coefficient.

6.2 NEURAL NETWORK THEORY.

The neural network implemented in this study was based on the equations from Boon *et al.*[258] with further 'inspiration' from Masters[263]. As with many challenging neural network problems, the final technique used is a hybrid of several basic techniques with a development that although logical may not seem scientific, and is not intended to be necessarily the optimal. The task of choosing the best network structure can only be achieved via a trial and error approach which should be abandoned when any further developments in the learning procedure, or changes in the actual architecture, are found to give negligible amounts of improvement. The final method described below was derived with few justifications for each developmental step other than that the method chosen made an improvement in the performance that was better than any of the others tried. Accounts of the many blind alleys taken are omitted for conciseness. The following sections describe the actual equations implemented and differ in parts to those found in the references. The full details of the conventional techniques are available in the texts already referenced.

6.2.1 Feed forward structure of a Neural Network.

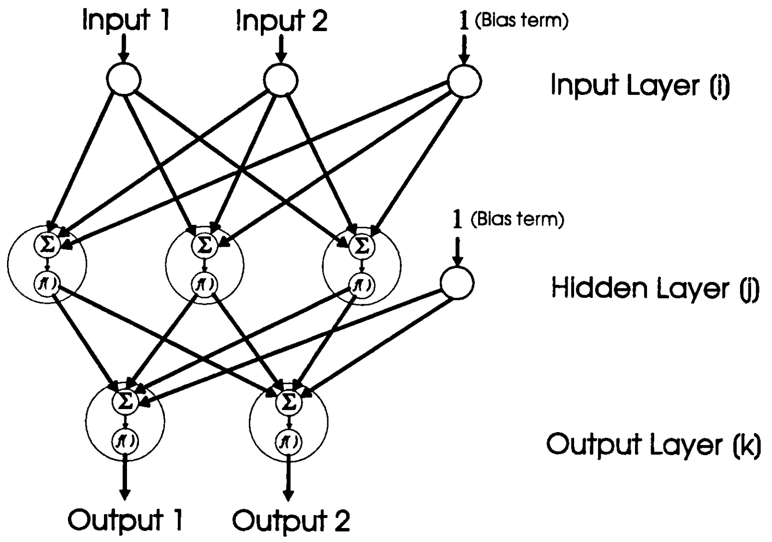

Figure **6.1** Schematic diagram of a three layer neural network.

The general schematic shown in fig. 6.1 shows the architecture of a three layer neural network consisting of the input layer, one hidden layer, and then the final output layer. The hidden layer is made up of a series of processing nodes which are individually connected to all the other nodes in the input and output layers by a web of interconnecting lines. Each of these connections have associated weights which are denoted by ω^{a}_{ji} where the subscript i refers to the position of the respective node in the previous layer, j corresponds to the node in the current layer, and the superscript denotes the position of the web in the structure. The output of each node is equal to a transform, $f(x)$, of the sum of all the inputs to the layer which in turn corresponds to the weighted outputs of the previous layer. The transform often takes the sigmoidal form;

$$f(x)=\frac{1}{1+e^{-x}} \tag{6.1}$$

The p number of inputs form the input vector $I^{(0)}=\{I_1^{(0)}, I_2^{(0)}...I_p^{(0)},I_{p+1}^{(0)}\}$ applied to the first layer where $I_{p+1}^{(0)}\equiv +1$ is the input bias term. These values are mapped directly onto the outputs of the input layer nodes via a pass through operator such that the nodal output is equal to the input; $I^{(0)}\equiv O^{(0)}$.

These nodal outputs from the input layer are multiplied by their respective weights and passed onto the next layer; the hidden layer containing q nodes. These weighted values are summated to form the input vector, $I^{(1)}$, for this hidden layer;

$$I_j^{(1)}=\sum_{i=1}^{p+1} \omega_{ji}^{(1)}O_i^{(0)} \tag{6.2}$$

which is then mapped onto the output vector by equation 6.1; $O^{(1)}=\{f(I_1^{(1)}),f(I_2^{(1)})...f(I_q^{(1)})\}$.

This output vector is weighted along with the bias node, $I_{q+1}^{(1)}\equiv +1$, and summated in a similar way to the outputs of the input layer to form the inputs to the output layer containing r nodes;

$$I_j^{(2)}=\sum_{i=1}^{q+1} \omega_{ji}^{(2)} O_i^{(1)} \tag{6.3}$$

which is likewise transformed to the output vector $O^{(2)}=\{f(I_1^{(2)}),f(I_2^{(2)})...f(I_{\underset{r}{q}}^{(2)})\}$ using an output transform function. When using the neural network for classification tasks, this function generally takes the same form as equation 6.1, yet for interpolation tasks, it tends to take the same pass through operator form used on the input layer. For this study the best results were obtained by using output nodes which contain the output function used normally in classification tasks, followed by an extra function of the form;

$$f(x) = A + Be^{-Cx} \tag{6.4}$$

where the constants A, B, and C are chosen so the total range of desired output vectors are mapped by an input range 0 to 1. All the training vector outputs are mapped backwards through this function and the learning procedure started in the conventional way.

6.2.2 Learning rule.

The entire training routine was based on the Error Backpropagation Learning Algorithm which adjusts the internodal weights of the neural network in order to minimise the error between what the neural network in its untrained, or semi-trained, state thinks the output should be, and what the trainer knows it should be. The training experience is specified by the training set made up of a collection of training vectors. These training vectors are comprised of pairs of input and target vectors where the target vector is the desired output vector for the respective input vector.

6.2.2.1 *Backpropagation.*

If the target vector is denoted as $T^{(n)}=\{T^{(n)}{}_1,T^{(n)}{}_2 \ldots T^{(n)}{}_t\}$ where n is its position in the training set, then the error term for an individual training vector can be specified as;

$$E=\frac{1}{2}\sum_{m=1}^{t}(T_m^{(n)}-O_m^{(2)})^2 \qquad \textbf{(6.5)}$$

This means that;

$$\frac{\partial E}{\partial \omega_{ji}^{(2)}}=\frac{\partial E}{\partial O_j^{(2)}}\frac{\partial O_j^{(2)}}{\partial \omega_{ji}^{(2)}} \qquad \textbf{(6.6)}$$

$$\frac{\partial E}{\partial \omega_{ji}^{(2)}}=-(T_j-O_j^{(2)})\frac{\partial O_j^{(2)}}{\partial \omega_{ji}^{(2)}} \qquad \textbf{(6.7)}$$

$$\frac{\partial E}{\partial \omega_{ji}^{(2)}}=-(T_j-O_j^{(2)})f'(I_j^{(2)})O_i^{(1)} \qquad \textbf{(6.8)}$$

If the transform function, $f(x)$, has the form shown in equation 6.1 then its derivative has the form $f'(\underset{x}{\cancel{t}}) = f(x)\ [\ 1 - f(x)\ ]$. In this case it is possible to write the partial derivative of the error term with respect to each individual weight between the hidden layer and the output layer as;

$$\frac{\partial E}{\partial \omega_{ji}^{(2)}} = -(T_j^{(n)} - O_j^{(2)})O_j^{(2)}(1 - O_j^{(2)})O_i^{(1)} \tag{6.9}$$

thus allowing a delta term to be defined for this particular layer as;

$$\delta_j^{(2)} = -(T_j - O_j^{(2)})O_j^{(2)}(1 - O_j^{(2)}) \tag{6.10}$$

Backpropagating the errors through the network allows the web between the hidden layer and the input layer to be considered. Here the minimisation task involves the partial derivative;

$$\frac{\partial E}{\partial \omega_{ji}^{(1)}} = -\sum_{m=1}^{r} (T_m - O_m^{(2)})\frac{\partial O_m^{(2)}}{\partial \omega_{ji}^{(1)}} \tag{6.11}$$

which gives in a similar way to the last web, a delta term in the form;

$$\delta_j^{(1)} = -O_j^{(1)}(1 - O_j^{(1)})\sum_{m=1}^{r} \delta_m^{(2)}\omega_{mj}^{(2)} \tag{6.12}$$

The learning process took place with two distinct phases, the first of which was based on the generalised delta rule with inspiration from simulated annealing, and the second on conjugate gradients[263].

6.2.2.2 *Training Phase 1.*

In this phase the training set has the order of all the training vectors randomised and each vector presented sequentially to the network. This allows each of the delta terms to be calculated in turn, after which the weights are updated according to the equations;

$$\omega_{ji}^{(2)}(n+1) = \omega_{ji}^{(2)}(n)+\eta\,\delta_j^{(2)}(n+1)O_i^{(1)}+\Delta\omega_{ji}^{(2)}(n) \qquad (6.13)$$

$$\omega_{ji}^{(1)}(n+1) = \omega_{ji}^{(1)}(n)+\eta\,\delta_j^{(1)}(n+1)O_i^{(0)}+\Delta\omega_{ji}^{(1)}(n) \qquad (6.14)$$

where

$$\Delta\omega_{ji}^{(m)}(n) = \alpha[\Delta\omega_{ji}^{(m)}(n-1)+\eta\,\delta_j^{(m)}(n)O_i^{(m-1)}] \qquad (6.15)$$

and the terms α and η are the momentum and learning rate terms respectively. Once all the terms in the training set have been presented (one epoch) the entire contents of the set was randomly resequenced and the set represented. This resequencing was undertaken to prevent the network from learning in oscillation, two or more different behaviours that may be prevalent in different regions of the set and are not necessarily the overall trend. A true generalised delta-rule learning algorithm would have its learning rate chosen to be small enough to prevent any overshoot of a minimum on the error plane with respect to the nodal weights. Escape from a local minimum on the error surface would be achieved by using the momentum term to create an overshooting effect which in the case of a global minimum would simply cause a damped oscillation that eventually settles. In this study the error surface appeared to have so many local minima that with a learning rate fixed at a value such that the local minimum was not missed, the convergence to a global minimum was prohibitively slow if at all possible.

Simulated annealing[263] takes its name from an analogy to the heat treatment of metals and is normally applied to the conjugate gradient method described in the second learning phase. The fundamental idea is to introduce an additional stage between each update where random noise is used to corrupt the nodal weights. If the error term after a corruption and a subsequent minimisation is less than the values before, the minimised values of the corrupted weights are taken on as the new set, if this is not the case then the corruption procedure is repeated until either a better solution is found or the number of unsuccessful corruptions exceed a limit. The learning procedure is repeated and the amount of noise used in the corruption decreased with the number of epochs made. The effect of this is a tendency to avoid the local minima by 'kicking the ball out of a rut' and is meant to resemble the way in metallic heat treatments, a gentle reduction in the temperature of a metal prevents the crystal lattice from trapping the discontinuities that cause hardness. The idea of not having to miss the nearest minimum was implemented in the above equations by selecting a relatively large value of learning rate which was used if its effect reduced the error for that particular training vector. If it did not, then another random value was chosen. After several attempted modifications it was found that simply keeping the learning rate at a fixed value, and updating regardless of whether it caused an increase or a decrease in the error, had a tendency to produce a trend that did reduce the overall error for the entire training set and gave results that clearly showed that the function was being learnt. Unfortunately the convergence became slower and slower thus necessitating phase two.

6.2.2.3 *Training Phase 2.*

The method of conjugate gradients[263] is renown for quickly propelling the neural network into the nearest minima. The method implemented involves calculating the delta terms in equations 6.10-6.12 for each individual training vector and then summating for all the vectors within the training set (the sum of the derivatives for a set of functions is the same as the derivative of the sum of the functions). The summated delta terms were then used to update the nodal weights at the end of each epoch according to the same equations used in phase 1 (equations 6.12-6.14), but with the momentum weight set at zero. The learning rate was carefully chosen to make the optimum step by using an iterative parabolic searching method[263]. The method was found to converge about ten times faster than the method used in phase 1 but was not able to escape any local minima. For this reason it was only implemented when phase one had started to produce negligible reductions. Its use gave a typical 20% improvement in the error values.

6.2.3 Selecting the optimum neural network.

Masters[263] provides a theoretical argument that there is never any need to use more than two hidden layers in the structure and that the majority of applications need only one hidden layer. Cases where 2 hidden layers are required tend to be situations where there are discontinuities in the function, or the number of inputs is low compared to the number of degrees of freedom needed to create a generalising function. A general rule of thumb[263] is that the initial structure to be tried should have a geometric pyramidal shape. From there the selection can only be achieved using a trial and error method until either the optimum structure is found, or the performance obtained is satisfactory, whichever of the two comes first.

The process involves keeping track of the error terms associated with a trial set as well as the training set. The trial set is composed in exactly the same way as the training set but contains input vectors which have never been seen by the neural network in its training mode. The error for either kind of set is given by;

$$E=\sqrt{\sum_{n=1}^{N_t}\sum_{m=1}^{t}(T_m^{(n)}-O_m^{(2)})^2} \qquad \textbf{(6.16)}$$

where N_t is the number of input-target vector pairs in the set. The tendency is for the training error to decrease towards a minimum as the training process progresses. The actual value of this minimum gets smaller as the number of nodes increases. A network with too few nodes will show similar decreases for both errors over the first few epochs but thereafter the trial error starts to level off while the training error continues to get smaller. The final level of the trial error tends to decrease with additional levels of network complexity until the optimum architecture is found. If the network is too complicated then it can lose its generalising ability. This situation is termed overtraining and causes the trial error to reach a global minimum before increasing again whilst the training error continues to decrease with the number of training epochs. This is because the network starts to learn traits seen in the training set, such as noise, which are not present in exactly the same form in the trial set. The complicating factor in the architecture selection procedure is that there is no guarantee that the network has settled at the global minimum. A selection of identical structures with different initialised settings should be trained to find out whether the minima found are consistently low. If they are, it can be assumed that there are negligible differences between those minima and the optimum. It should also be realised that there is a major computation time cost associated with the training and use of the larger networks which may have to be offset against the gain in reduced error when considering a more complicated network.

The searching procedure adopted was to start off with a very low number of nodes in the hidden layer and to increase one by one until either a satisfactory performance had been obtained or the network started to show signs of being overtrained.

6.3 NETWORK IMPLEMENTATION.

The network was trained with Monte Carlo generated coherence peak line shapes which had been smoothed to model the finite system response of the apparatus. The complete implementation procedure is outlined in the flow diagram shown in fig 6.2.

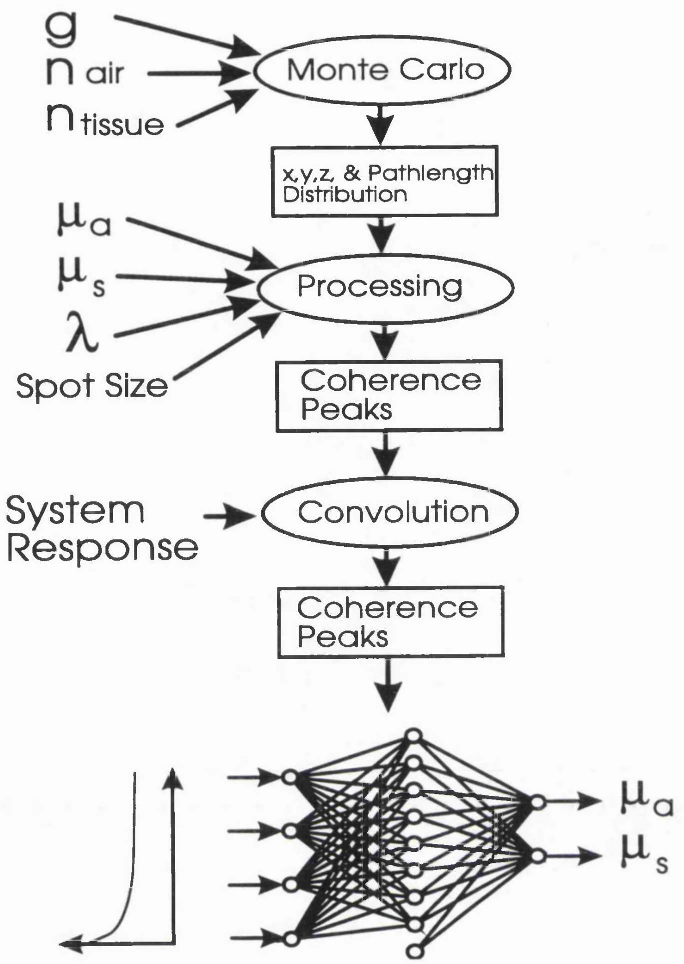

Figure **6.2** Flow diagram showing the stages that go into generating a neural network that can be used to extract the optical coefficients from a coherent backscatter line shape.

The input vector contains the predicted intensity at a spread of angles:-

0, 0.025, 0.05, 0.075, 0.1, 0.15, 0.2, 0.25, 0.3, 0.35, 0.4, 0.45, 0.5, 0.6, 0.7, 0.8, 0.9, 1.0, 1.25, 1.5, 1.75, and 2 mrad,

whilst the output vector contains the reduced scattering and absorption coefficients over the ranges 0.2 to 2.2 mm^{-1} and 0.01 to 0.6 mm^{-1} respectively.

The other fixed parameters required are;

1) The refractive index mismatches (n_{glass}=1.5 & n_{tissue}=1.4).
2) The illuminating spot profile (that measured experimentally).
3) The wavelength of the light (1064 nm *in vacuo*).
4) The anisotropy factor (g = 0.9).
5) The system response (0.15 mrad).

The training set was generated according to these fixed parameters and several networks with differing numbers of nodes in the hidden layer made to learn what the outputs should be. An associated trial set was also generated with target vectors that were spread across the mid range of the training set (see fig.6.5).

The data in fig. 6.3 shows the final trial and training errors that were obtained from this series of networks as a function of the different number of nodes in the hidden layer. The trend shows that there is little advantage in performance when using a network that has more than ten nodes in the hidden layer. Any further benefit in performance that might exist should be offset against the large increase in the computational cost that is associated with the larger

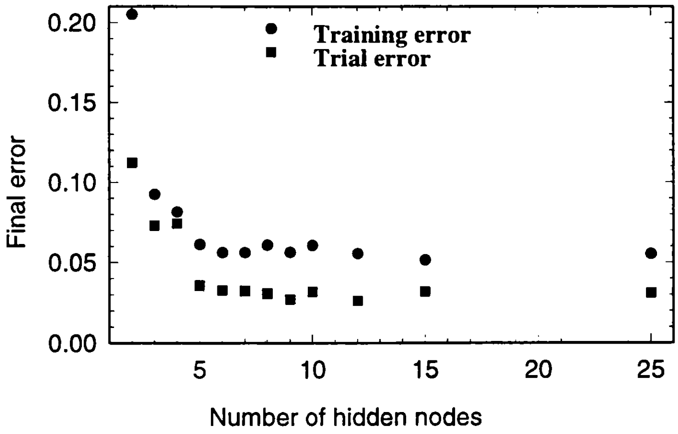

Figure **6.3** The final training and trial errors as a function of the number of nodes in the hidden layer.

networks. Repeating the same training routine on identical structures but with different starting values for the nodal weights, showed variations in the initial error reduction behaviour but this eventually settled down towards the end in a manner that was consistent between the different training runs. The final resting values showed only minor variations which were of the order of the ripple behaviour seen between the larger numbers of nodes in fig. 6.3. With these facts in mind, the optimum architecture for this study was chosen to be the one with 9 nodes in the hidden layer. The way in which the error was reduced for this case with the progression of the training routine is shown in fig. 6.4. The kink present in the errors towards the end corresponds to the superior performance that was obtained by switching between the training phases 1 and 2. An indication of the final overall performance can seen in fig. 6.5 which displays the coefficients used as targets in the trial set along with the respective outputs from the network (nearest circles). Calculation for this trial set of the mean percentage error and its standard deviation for the reduced scattering and absorption coefficient separately gives the respective values 0.5 ± 3.6 and -0.2 ± 6.9. These errors are relatively small and are likely to be a consequence of the ripples present in the target vectors that arise from the limited number of modelled photons.

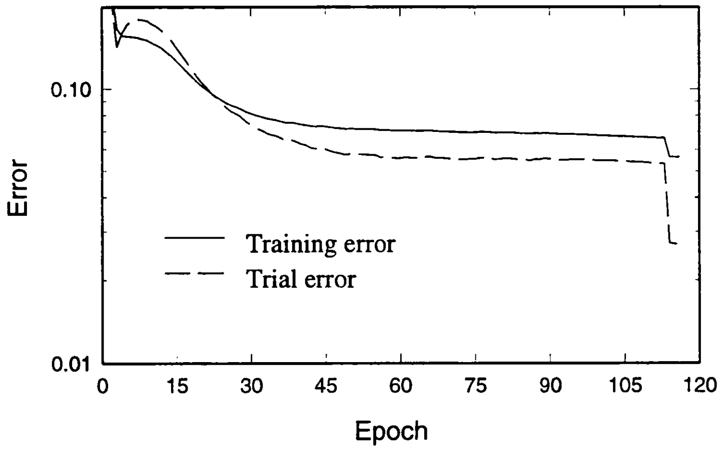

Figure **6.4** The reduction in trial and training errors that were obtained during the training of a neural network with 9 nodes in the hidden layer.

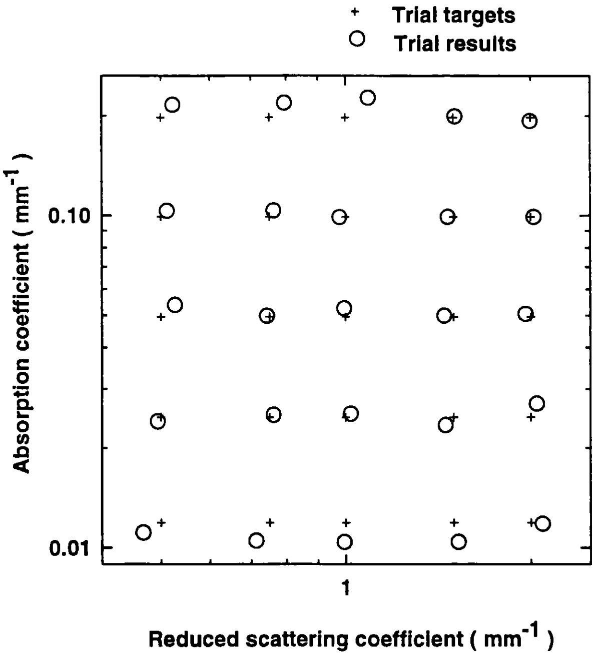

Figure 6.5 Target vectors from the trial set along with the outputs from the trained neural network.

6.4 CHAPTER SUMMARY.

This chapter has reviewed the history and implementation of neural networks. The application of using a Multi Layered Perceptron to solve inverse problems when only the forward model can be simulated has been considered. A customised training method has been developed and shown to provide an adequate level of performance when trying to interpret the expected line shape of a coherence peak profile from specific kinds of biological media. The particular network to be used in chapter 7 was selected to provide a suitable performance as far as both speed and accuracy are concerned.

CHAPTER 7

COHERENT BACKSCATTER EXPERIMENTS.

This chapter gives an overview of the experiments performed to measure the reduced scattering and absorption coefficients of biological tissues. Experiments on phantom media were used to validate the technique and a detailed discussion is presented on the possible limitations. Several experiments were performed on *in vitro* tissues in order to shed light on the effects caused by the different possible states of polarization in the interrogating beam, and the in the case of muscular tissue, the orientations of the fibres. A demonstration was performed of the technique on *in vivo* specimens.

7.1 EXPERIMENTAL APPARATUS AND METHOD.

The experimental apparatus is outlined in fig. 7.1. The illuminating source was a CW Nd:YAG laser operating at 1064 nm with around 1 W of output power in single transverse mode operation; TEM_{00} (YAG Max II Model 212 CVI Laser Corp. Albuquerque, New Mexico, USA). The detector system consisted of a

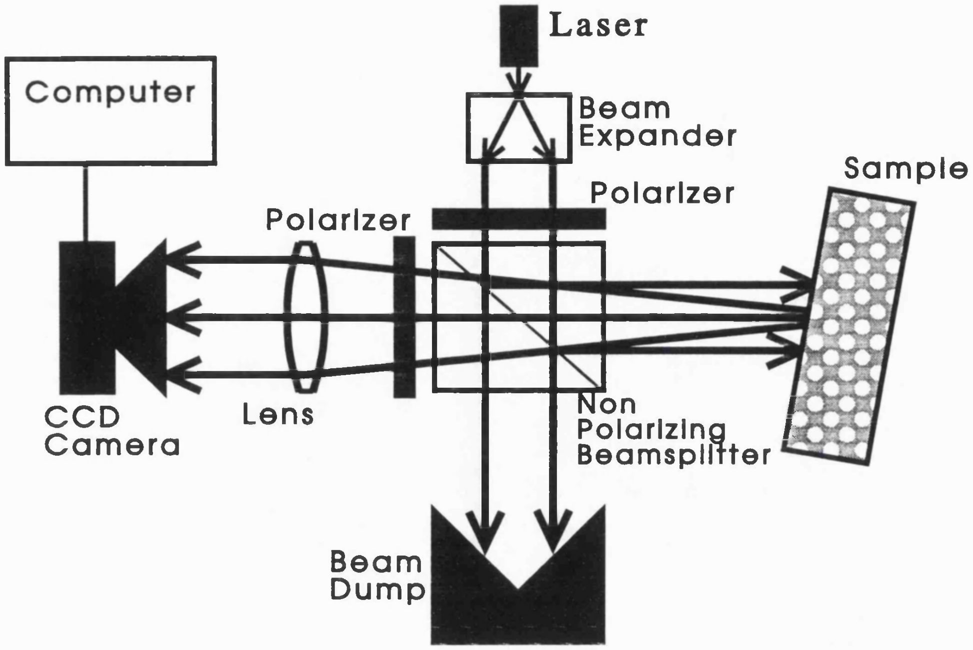

Figure **7.1** Schematic outline of the experimental apparatus.

positive ~~negative~~ lens placed at the focal length (50 cm) away from the surface of a room temperature CCD camera (4980 series CCIR Cohu Inc. San Diego California USA) connected to a frame grabber unit (ADVICE, Brian Reece Scientific Limited, Berkshire, UK) with IBM compatible 386 personal computer. The camera resolution was 752 by 582 with pixel dimensions of 8.3 by 8.6 μm which gives in this set up, an angular resolution of 16.6 by 17.2 μrad over the total range 13 by 10 mrad. The output of the frame grabber was set for an image in a TIF format that represented the integral of the incident light over a period lasting 32 video frames (1.28 seconds). These images were subsequently processed with custom written programmes to correct for the spatial variations in response and the non uniform pixel dimensions. The polarizers used in the illumination and detection path were linear Glan-Thomson prisms with the option of adding quarter wave plates to produce circular states of polarization. The size of the optical bench used restricted the possible distance between the laser and the beam expander to 1.5 m with a further optical path distance of 30 cm to the sample via the beam splitter. The beam expander was composed of a positive and a negative lens such that the expansion was by a factor of four. The 10 mm cube beam splitter was a non polarizing variety with a broad band anti-reflection coating. The laser beam incident on the surface of the beam splitter was a few degrees off the surface normal to prevent any residual reflections from finding their way onto the camera.

For experiments on liquid media, the sample cuvette was comprised of a tank with dimensions 45 mm deep, and at least 20 by 20 mm on the illuminated surface. The laser beam was incident on a window formed by a 100 μm thick cover slip (refractive index of the borosilicate glass used at 1064 nm is equal to 1.50), also tilted to prevent any specular reflections from being directed into the camera. This thickness is less than the expected reduced scattering mean free path of any biological tissue and is thus unlikely to be in the regime were the kinks are present in the coherence peaks as simulated by Ospeck and Fraden[230]. The boundary condition as far as internal reflections are concerned can be approximated to that of a single refractive index mismatch equal to that between glass and air, and as far as the effects of Snell's law and refraction is concerned, to that of a tissue-air boundary. For solid samples, the specimens were placed in isotonic saline and pressed up against a similar window to replicate the same boundary conditions as found in the fluid experiments. This has the advantages that the boundary can be considered to appear flat and the results processed with the same refractive index assumptions as were made with the fluid experiments. The importance of having a flat sample is that a heavily grooved surface gives the possibility of multiple surface reflections which can lead to coherence peaks[218-220]. Other problems associated with rough surfaces include retro-reflections[203] and the increase in the total amount of surface reflections over those obtained from flat perpendicular planes.

For liquid samples, the ensemble averaging needed to remove the speckle pattern is performed by the Brownian motion of the suspended scattering particles. For the solid samples, the material was gently wobbled to ensure that the total surface area interrogated was kept to a minimum, yet moved sufficiently to average out the speckle. This is similar, in principle, to rotating the sample with a motor which was found to be awkward[248] with tissue samples and prohibitive if the orientation of fibres was to be kept constant. As with the work of Yoon *et* *al.*[247], it was found that this necessary movement was achieved by the natural pulsations present in living tissue.

The alignment procedure was performed with care to ensure that all the passages through the optical components were on axis and did not corrupt the planar wave-front. The telescope was adjusted to give as near perfect collimation as possible and the attenuated back reflection from a flat neutral density filter recorded on the CCD camera. The resulting picture was analyzed by fitting a Gaussian curve to the profile. The detector to lens separation was adjusted until the minimum $1/e^2$ width was found in the profile at around 0.15 ±0.01 mrad. This picture profile is termed the system response and describes the non ideal performance of the set up arising from the unavoidable beam divergence and focusing errors. The spatial beam profile on the sample was measured by taking the camera and imaging the illuminated spot through the beam splitter on a rotating plastic phantom with high values for both the scattering and absorption coefficients. It is assumed that under these conditions, the image, although comprised of backscattered light, is representative of the incident flux. Analysis of this image showed that the profile was Gaussian which indicates that the laser was operating in a single transverse mode. The recorded data and the curve fitted results of the spatial profile showing a $1/e^2$ width of 4.6 mm are displayed in fig. 7.2.

In this particular set up, it was not possible to easily include a monitor for the power output from the laser (an earlier design using a one dimensional array allowed an optical fibre to be connected from within the beam dump to just a few of the pixels in the array). It is therefore necessary to assume that the laser is relatively stable and to check for laser drift by recording images off a reference standard before and after the interrogation of each sample. This rather unsatisfactory method showed fluctuations of up to 10% at times in the laser power. This is one major source of uncertainty in the measurements.

Once an image is obtained and the adjustments made to compensate for a non flat response from all the pixels in the picture, plus removal of the background thermal noise and ambient light levels, it is necessary to extract the profile by first finding the centre of the peak and then performing a radial

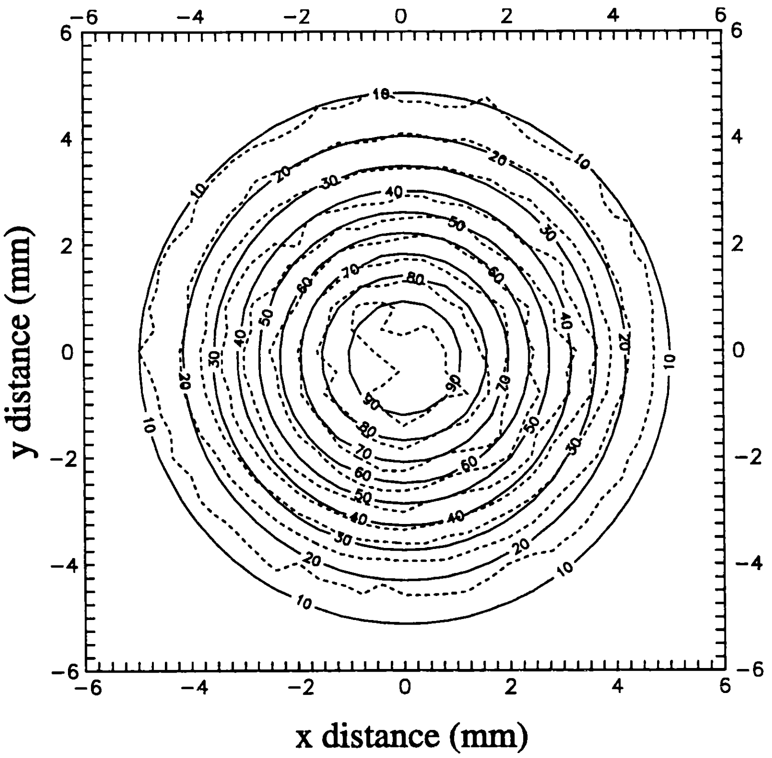

Figure 7.2 Contour map of incident intensity profile with the raw data shown by the dashed lines and the fitted results by continuous lines (contour labels correspond to percentage of maximum).

average. Finding the centre was achieved by initially identifying the largest pixel value in the picture and then for a square region around this centre point, summating all the pixel values in each row and then in each column. These two one-dimensional profiles represent the projections of the peak which for a symmetric cone shape will be in the form of a parabola. A triangular function is fitted to each of these projections in turn with the centre variable of the triangular function as one of the fitting parameters. The final curve-fitted result for this parameter in each projection is taken as the corrected coordinate for the centre. This method was found to be extremely robust, even in the presence of a large amount of noise. The radial average was then obtained by taking each pixel value in turn, working out its radial distance from the centre point and placing its value in the nearest representative radial bin. The summated values in each radial bin were finally divided by the number of pixels that went in to making up the sum, thus giving the radial average. If the cone shapes were initially symmetric, then the improvement in the signal to noise ratios was considerable compared to taking simple line sections. It should however be realised that with this method, the statistical noise increases as the radial coordinate decreases.

The *in vitro* tissue samples used were obtained from a local wholefood butcher with assurance that the free range samples were fresh and had never been frozen. All the experiments were conducted within what was believed to have been 24 hours of death, on samples that were freshly excised from as deep within the tissue mass as possible. A number of the experiments were performed on coagulated tissue samples where the method used to denature the protein resembles that used in the experiments of Roggan *et al.*[148]. The tissue samples were wetted with saline and wrapped in 5μm polyvinyl chloride film which was then immersed in recently boiled water for a couple of minutes. For the sizes of tissue specimens used here, between 10 and 20 mm thick, this is sufficient to produce a thorough cooking effect without excessive dehydration. The surface of these tissues is therefore representative of the deep coagulation zones found after laser photocoagulation.

Two methods are used to process experimentally obtained coherence peaks involving either interpolation within a look-up array, or alternatively, by using a neural network. The interpolation method is an implementation of the standard Levenberg-Marquardt method of least squares fitting for non-linear functions[264]. The interpolation array is three dimensional with an exponential distribution of absorption coefficients in one direction, an exponential distribution of scattering coefficients in another, and an exponential distribution of angles in the third. The array was produced by considering a tissue refractive index of 1.4 up against an infinitesimally thin glass layer with a refractive index of 1.5 which was then open to the air. All angles were corrected for by Snell's law of refraction and the system response set at 0.15 mrad. The anisotropy factor was set at 0.9 and all single scatter events ignored to account for the use of circular polarizers. The illumination spot profile used was that measured experimentally which when fitted to a Gaussian curve gave the $1/e^2$ width as 4.6 mm. All the curves were normalised with respect to the incoherent intensity level. The total intensity profile of the coherence peak was obtained by multiplying the curve shape with the scalar intensity obtained from the graph of the backscattered intensity as a function of the reduced scattering to absorption coefficient ratio (fig. 4.12). This method was found to work reasonably well as indicated by the good agreement between the fitted and raw data. For fig. 7.5, which shows a selection of coherence peak profiles obtained from phantom media that can be considered to be representative of a range of biological media, the mean estimated standard deviations of all the probable percentage curve fitted uncertainties[264] are equal to 0.9% and 1.3% for the reduced scattering and absorption coefficients respectively. This is lower than the corresponding 7% and 28% uncertainties that arose from the 10% instability of the laser output power level. These latter uncertainties are those displayed in all the results and are derived by averaging the magnitude of the percentage differences found in the extracted coefficients after separately scaling the original profiles by a factor of 1.1 and 0.9.

This interpolation technique is relatively slow compared to that of a neural network which although not showing any indication of its fitting confidence, tends to be more robust than the former. This major advantage is derived from its generalising nature which ignores the statistical noise ripples seen in the Monte Carlo generated data that in turn produces the false local minima in the curve fitting error surface. The training set used for the neural network was derived by calling the interpolation routine described above for random combinations of angle, reduced scattering, and absorption coefficients. In the following data sets, the fitted profiles displayed were calculated with the interpolation method whose fitting parameters were all very close to the output of the neural network. Cases where the results from the two techniques did not match corresponded to poor confidence parameters from the curve fitting routines. When this occurred in the phantom experiments, the results from the interpolation method were, unlike the neural network results, a deviation away from the expected trend. It can therefore be concluded that the neural network is forming a more robust method which avoids local minima.

7.2 EXPERIMENTAL RESULTS

7.2.1 Phantom media with discussion on the validity of the results.

Experiments on phantoms were used to validate the accuracy of the technique for low absorbing variations in the scattering coefficient, and for a fixed, relatively high scattering coefficient, the variation in absorption. Fig. 7.3 shows contour plots of the experimentally obtained data on a diluted fat emulsion (around 1 part Intralipid$^{TM}{}_{10\%}$ to 4 parts water, Intralipid from Pharmacia Ltd. Milton Keynes, U.K.) normalised with respect to the background level to give comparisons of the actual cone shapes. The plots show on the left, the profiles seen with circularly polarized light, and to the right, the profiles seen with linear polarizers. The plots at the bottom are for the same situations as the top but with added ink (370 p.p.m black China Ink; rotring^{TM}, Hamburg, Germany). The respective radial averaged profiles are displayed in fig. 7.4. All the intensity scales on these and subsequent radially averaged profiles are normalised with respect to the incoherent intensity recorded off a solid scattering phantom[187] with a reduced scattering coefficient of 4 mm^{-1} and an absorption coefficient of 0.01 mm^{-1}. The anisotropy of the cone shape with the linear polarizers links in directly with the previous observations and simulations[230,236,237]. These references attribute such effects to the presence of low order scattering events. It should be noticed that in the rest of the experimental data obtained during this study, no biological media ever showed this phenomenon. A similar non-appearance in any tissue sample is of the coherence peak seen in the depolarized light that is interrogated by having the polarizers in the incident and detected beams in crossed states. The only time it was ever seen was with either circularly or linearly polarized light incident on relatively high concentrations of fat emulsion which had not been mixed with any ink.

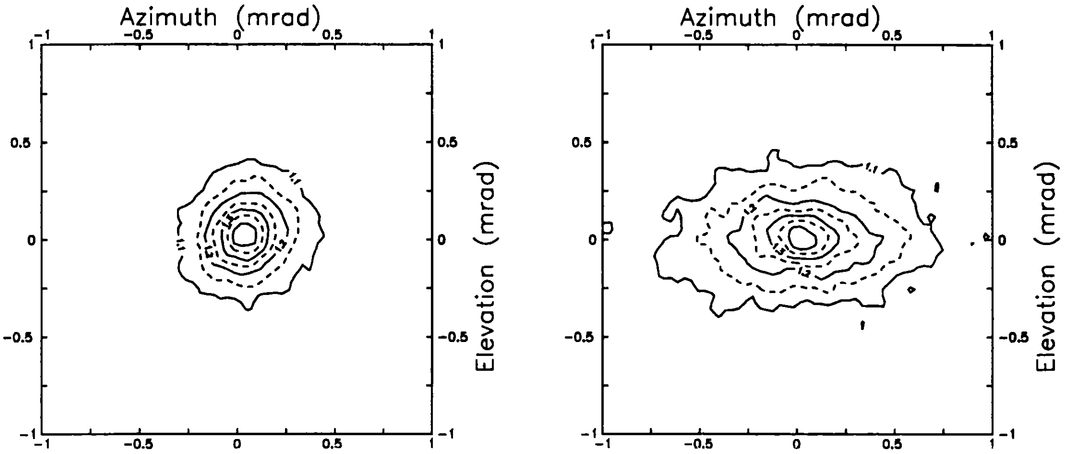

Circular polarizers
diluted Intralipid

Linear polarizers
diluted Intralipid

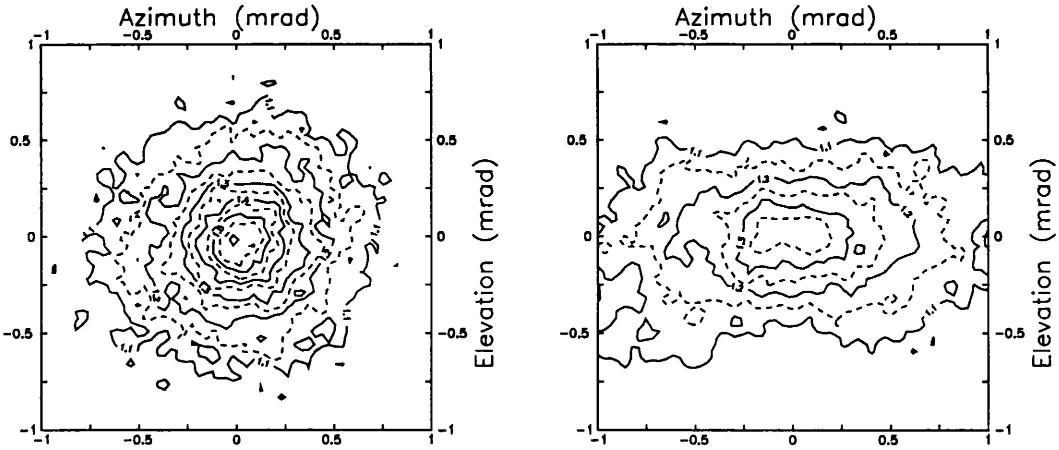

Circular polarizers
diluted Intralipid and ink

Linear polarizers
diluted Intralipid and ink

Figure 7.3 Contours of coherence peaks from diluted fat emulsion with and without ink for both circular and linear polarizations. Intensity is normalised with respect to the incoherent intensity.

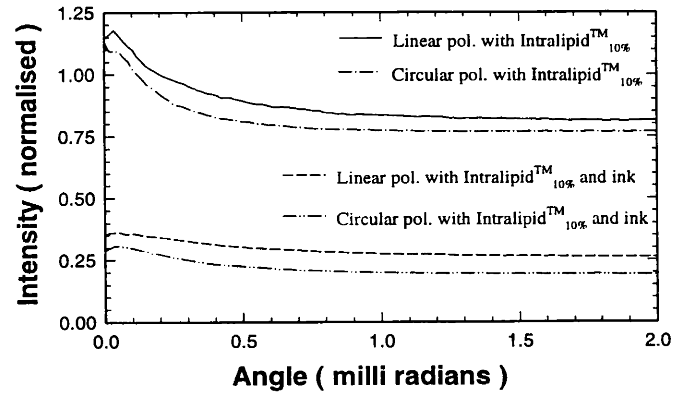

Figure 7.4 Radial average profiles of coherence peaks from diluted fat emulsion with and without added ink for circular and linear polarizations, normalised to reference level.

Fig. 7.5 shows a selection of the fitted profiles of experimentally obtained coherence peaks from the phantom samples with circularly polarized light. As with the other fitted profiles in this report, the symbols represent the experimentally obtained data and the lines show the curve fitted profiles. Analysis of the profiles obtained with linear states of polarization has been omitted due to the difficulties associated with the unpredictability of the single backscatter component. This is because the scattering particles found in biological media are not perfect spheres. If they were, then the method of den Outer[203] could be used to extract the anisotropy factor by analysing the differences seen in the enhancement ratios when using linearly and then circularly polarized light.

Fig. 7.6 and 7.7 shows the parameters that have been extracted from the profiles with the use of the neural network for the added ink and dilution experiments respectively. A clearly visible linear trend can be seen in the data showing the addition of ink. The reduced scattering coefficient remains constant at around the 1.4 mm^{-1} that the level of dilution predicted, whilst the absorption coefficient rises linearly at a rate comparable to that expected from the collimated experiments described in chapter 3, section 3. These graphs include the results from when the experiment was repeated five times when the level of added ink was at around 0, 175, and 275 p.p.m. The consistency seen in the results indicate a satisfactory level of reproducibility that is within the errors caused by the unstable laser power level. The actual difference in slope between that obtained (0.0008 mm^{-1} v^{-1}) and that expected (0.0005 mm^{-1} v^{-1}) can be accounted for by the uncertainties in the collimated transmission technique and the variability that may be expected from sample to sample (v is the volume fraction of added ink expressed in parts per million). The deviation away from the linear trend in scattering coefficient and constant absorption for the dilution experiment is of more concern and is discussed in greater detail below. The absorption coefficient should have remained at that of water (0.0118 mm^{-1}) whilst the slope of the reduced scattering coefficient should have been 7 mm^{-1} v^{-1} (v in this case is the absolute volume fraction of Intralipid$^{\mathrm{TM}}{}_{10\%}$ solution added to the water).

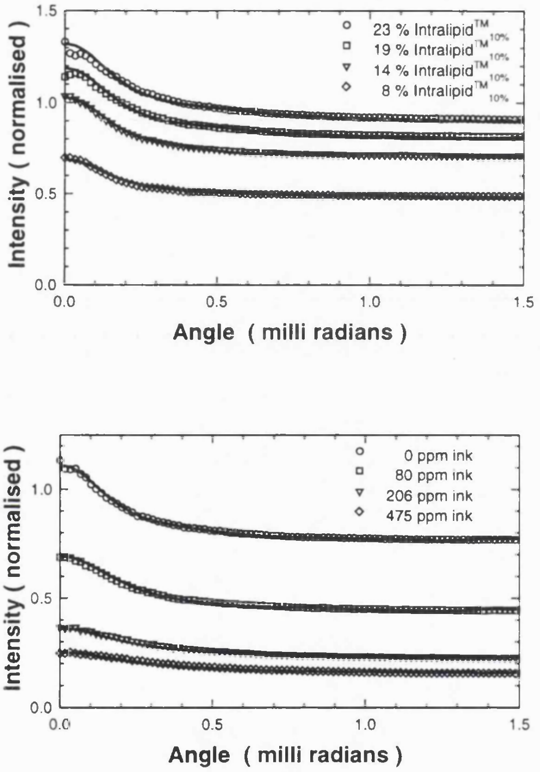

Figure **7.5** Fitted profiles for coherence peaks with circular polarized light from various samples of diluted fat emulsion with added ink, normalised to reference.

The overall trend is for an over estimation of the absorption coefficient at high dilutions where the scattering coefficient is very low. At the higher volume fractions the reduced scattering and absorption coefficients are in good agreement with those expected. Repetition of the experiment 5 times with the dilution held at around 7, 14, 19, and 25 % as displayed on the graphs, shows a high degree of consistency across the dilution range (less than the errors predicted by the 10% instability in laser output power). The simplest account of the errors would be a discrepancy between the roll-off of the intensity with the ratio of absorption to scattering as predicted by the Monte Carlo model, and the experimental situation. This is feasible as the polarization of a photon in a scattering medium is known to be scrambled during its propagation and the fact that here, the experimental apparatus will only record the intensity of photons whose polarization has either not been altered, or if scrambled, then scrambled back into the original state. Chapter 3, section 2.3 discussed references on the way in which polarization is preserved during scattering within biological tissues with the conclusion that there are few quantitative trends that can be reliably interpreted in the general sense needed here. The scattering coefficient measured with this technique is polarization dependent which means they may have a slightly different nature to those measured conventionally which are ambiguous in the sense that their polarization characteristics are ignored. It has always been assumed from the early experiments in coherent backscatter that a scalar theory is appropriate for the vectorial nature of light transport[200-202,223,230,232,237,242-244,247] in such a context.

Other causes of errors in the method include uncertainties in the reference power level, the beam profile, the system response, the assumed refractive index mismatches, and scattering anisotropy factors. All these factors were investigated and the conclusion was drawn that the effects were slight and could not correct for the trends of error. Experimental limitations such as the finite sample cell dimensions and possible non-linearities in the camera are consistent with the trends seen at low dilutions in this set up, but not for the magnitude or the behaviour at high levels. Restrictions in the numerical model such as the finite length and total number of the modeled photon paths are possible causes of concern but the large limits that have been chosen are considered to be sufficient. Numerical inaccuracies in the data processing and fitting routines have been kept to a minimum and along with the inaccuracies of the neural network are all considered to be negligible. The consistency with which the curve fitting routines managed to find the centre of the peak suggests that the subsequent uncertainties caused by such an error is small. A final cause of error is the possibility of a lack of a planar wave-front but this is not thought to be a significant problem and is not a trivial matter to assess in detail.

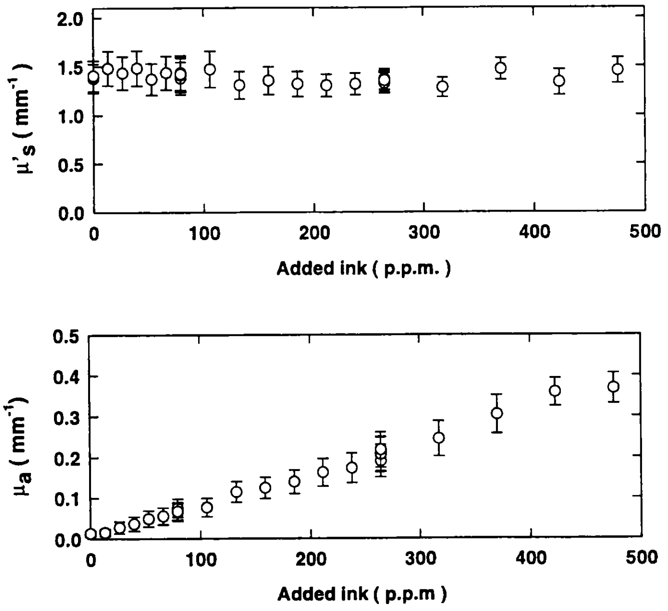

Figure 7.6 Reduced scattering and absorption coefficients extracted from coherence peak profiles with the neural network for the added ink experiment.

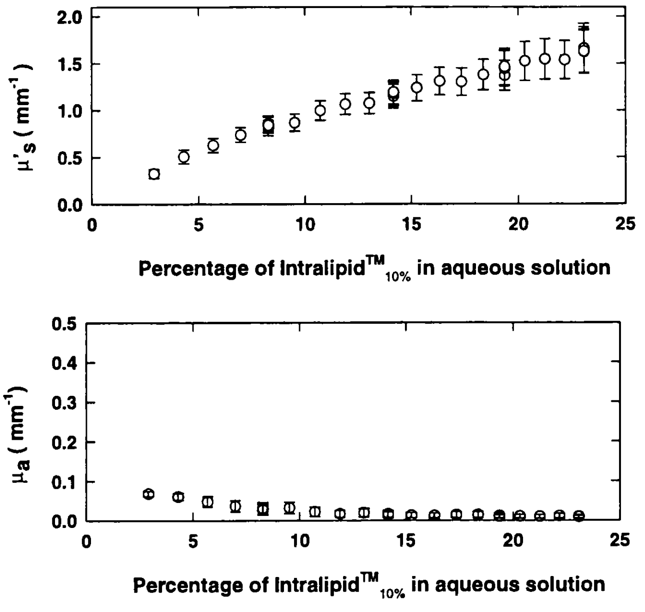

Figure 7.7 Reduced scattering and absorption coefficients extracted from coherence peak profiles with the neural network for the dilution experiment.

7.2.2 Biological media.

Fig. 7.8 shows a collection of the fitted profiles obtained with circular polarizations from various samples of *in vitro* tissue and from an *in vivo* human hand. To show the differences between circularly and linearly polarized light, contour plots are displayed in fig. 7.9 for parts of a human hand with the respective profile graphs in fig. 7.12. The effect of fibre orientation is displayed with contour plots in fig. 7.10 and with profile graphs in fig. 7.13 for circularly polarized light on coagulated and native porcine muscle. This is repeated for linearly polarized light with the contour plots in fig. 7.11 and the profile graphs in fig. 7.14. These profiles show that for certain tissues, there are slight differences in both the shape and absolute backscattered intensity indicating that the orientation is important. It is possible however, that some of these discrepancies may be artifacts that arise from the laser output power instability or the sample to sample variation.

Table VII.1 and Table VII.2 show a listing of the extracted reduced scattering and absorption coefficients for the selection of biological media examined. Each medium was represented by one sample and was measured three times in different areas. Two types of errors are quoted, the first is the sample standard deviation and the second is the system uncertainty that arises from the uncertainty in the laser power. This latter error was estimated by averaging the differences seen in the curve fitted results when the profile was scaled by 0.9 and then 1.1. For fibrous media the results are displayed for both end-on and lateral orientations of the fibres.

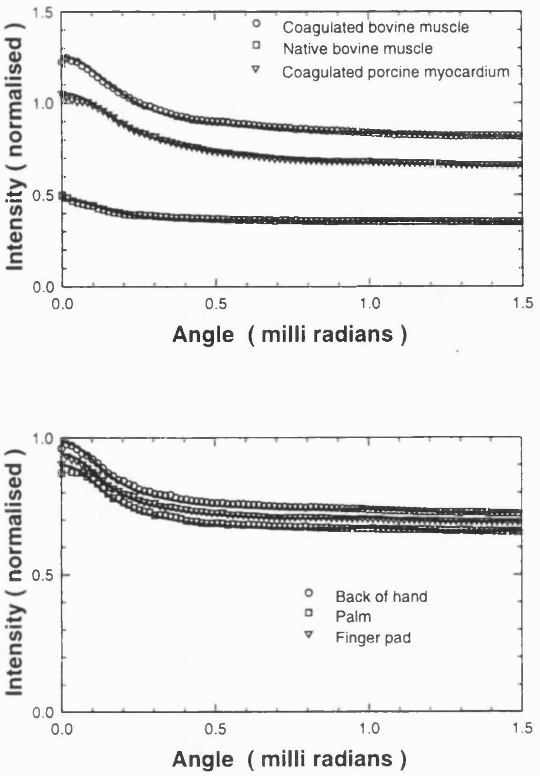

Figure **7.8** Coherence peak profiles obtained with circularly polarized light on various samples of meat.

Table VII.1 *In vivo* optical coefficients from human hand extracted using a neural network.

Part of human hand	$< \mu'_s >$ (mm^{-1})	$\sigma(\mu'_s)$ (mm^{-1})	System Error of μ'_s (mm^{-1})	$< \mu_a >$ (mm^{-1})	$\sigma(\mu_a)$ (mm^{-1})	System Error of μ_a (mm^{-1})
Back	**1.11**	0.04	0.08	**0.014**	0.005	0.002
Palm	**0.94**	0.07	0.06	**0.016**	0.0002	0.004
Wrist	**1.10**	0.11	0.08	**0.016**	0.003	0.005
Finger	**0.94**	0.06	0.12	**0.013**	0.001	0.003

Table VII.2 Optical coefficients from various *in vitro* biological media extracted using a neural network.

Medium		Fibre Orientation	$< \mu'_s >$ (mm^{-1})	$\sigma(\mu'_s)$ (mm^{-1})	System Error of μ'_s (mm^{-1})	$< \mu_a >$ (mm^{-1})	$\sigma(\mu_a)$ (mm^{-1})	System Error of μ_a (mm^{-1})
Bovine muscle	Native	End on	**0.63**	0.04	0.04	**0.057**	0.001	0.006
		Lateral	**0.58**	0.05	0.03	**0.058**	0.004	0.006
	Coagulated	End on	**2.34**	0.11	0.16	**0.031**	0.008	0.008
		Lateral	**1.82**	0.08	0.12	**0.023**	0.003	0.007
Porcine muscle	Native	End on	**0.45**	0.06	0.03	**0.055**	0.006	0.003
		Lateral	**0.47**	0.03	0.03	**0.065**	0.001	0.003
	Coagulated	End on	**1.20**	0.02	0.06	**0.017**	0.005	0.003
		Lateral	**1.25**	0.10	0.07	**0.039**	0.004	0.008
Porcine myocardium	Native	End on	**0.63**	0.01	0.04	**0.060**	0.004	0.006
		Lateral	**0.61**	0.06	0.03	**0.065**	0.007	0.005
	Coagulated	End on	**2.04**	0.009	0.15	**0.037**	0.010	0.010
		Lateral	**1.99**	0.21	0.13	**0.040**	0.004	0.009
Porcine liver	Native	None	**0.57**	0.04	0.03	**0.051**	0.005	0.006
	Coagulated	None	**2.33**	0.15	0.16	**0.016**	0.003	0.005

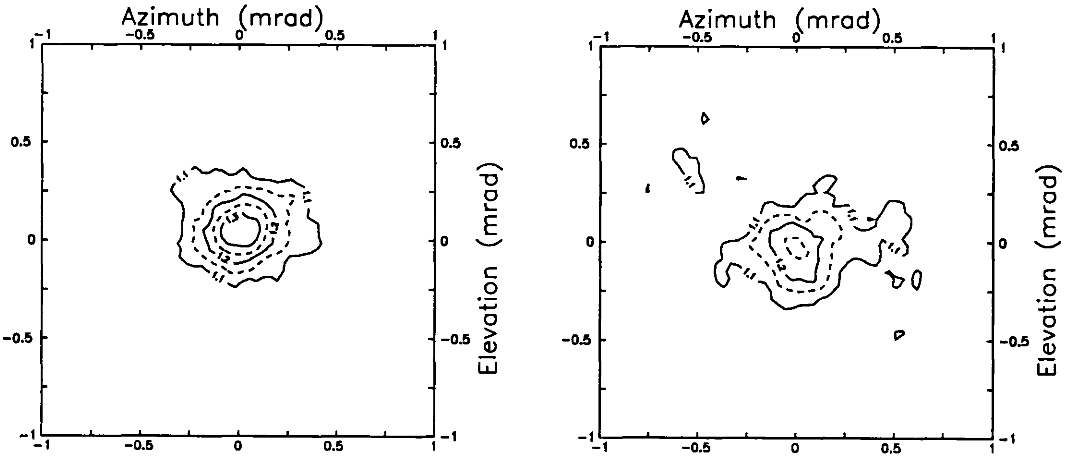

Circular polarizers
Human palm

Linear polarizers
Human palm

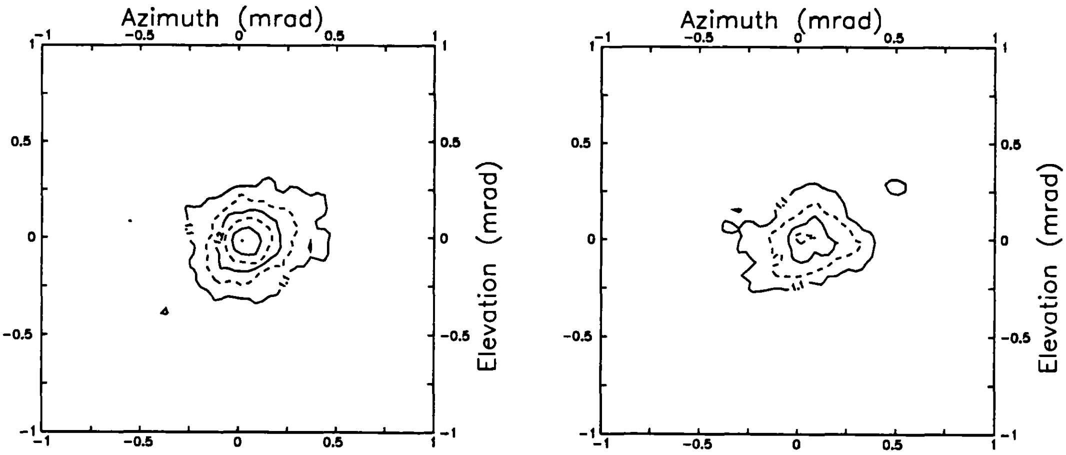

Circular polarizers
Human finger

Linear polarizers
Human finger

Figure 7.9 Contour plots of coherence peaks from human hand with different states of light polarization. Each plot is normalised with respect to background level.

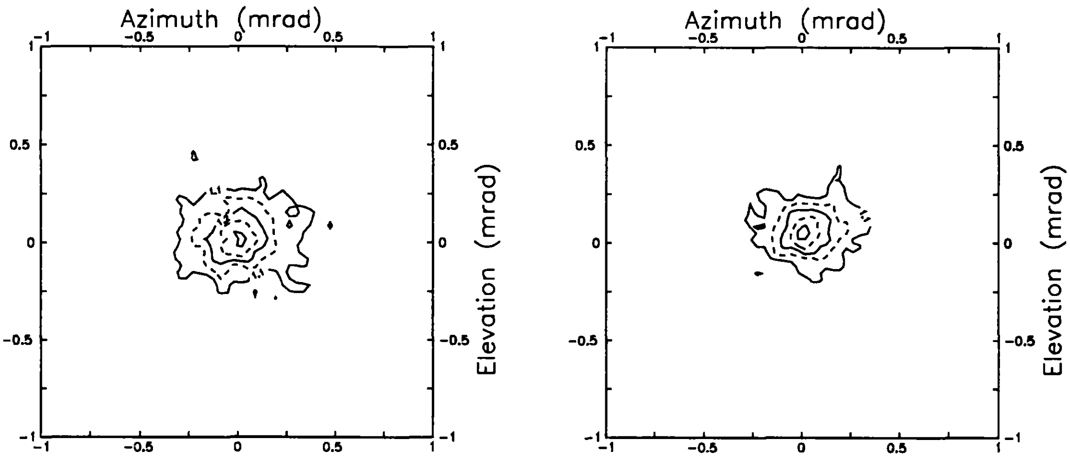

Circular polarizers
Native porcine muscle
Fibres lateral

Circular polarizers
Native porcine muscle
Fibres end on

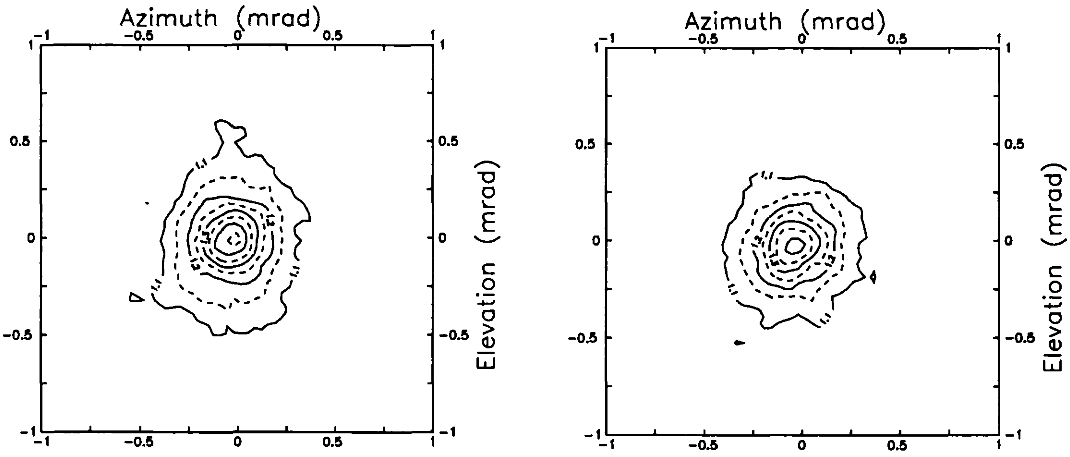

Circular polarizers
Coagulated porcine muscle
Fibres lateral

Circular polarizers
Coagulated porcine muscle
Fibres end on

Figure **7.10** Contour plots showing the coherence peaks obtained with porcine muscle and circularly polarized light with various orientations of the fibres.

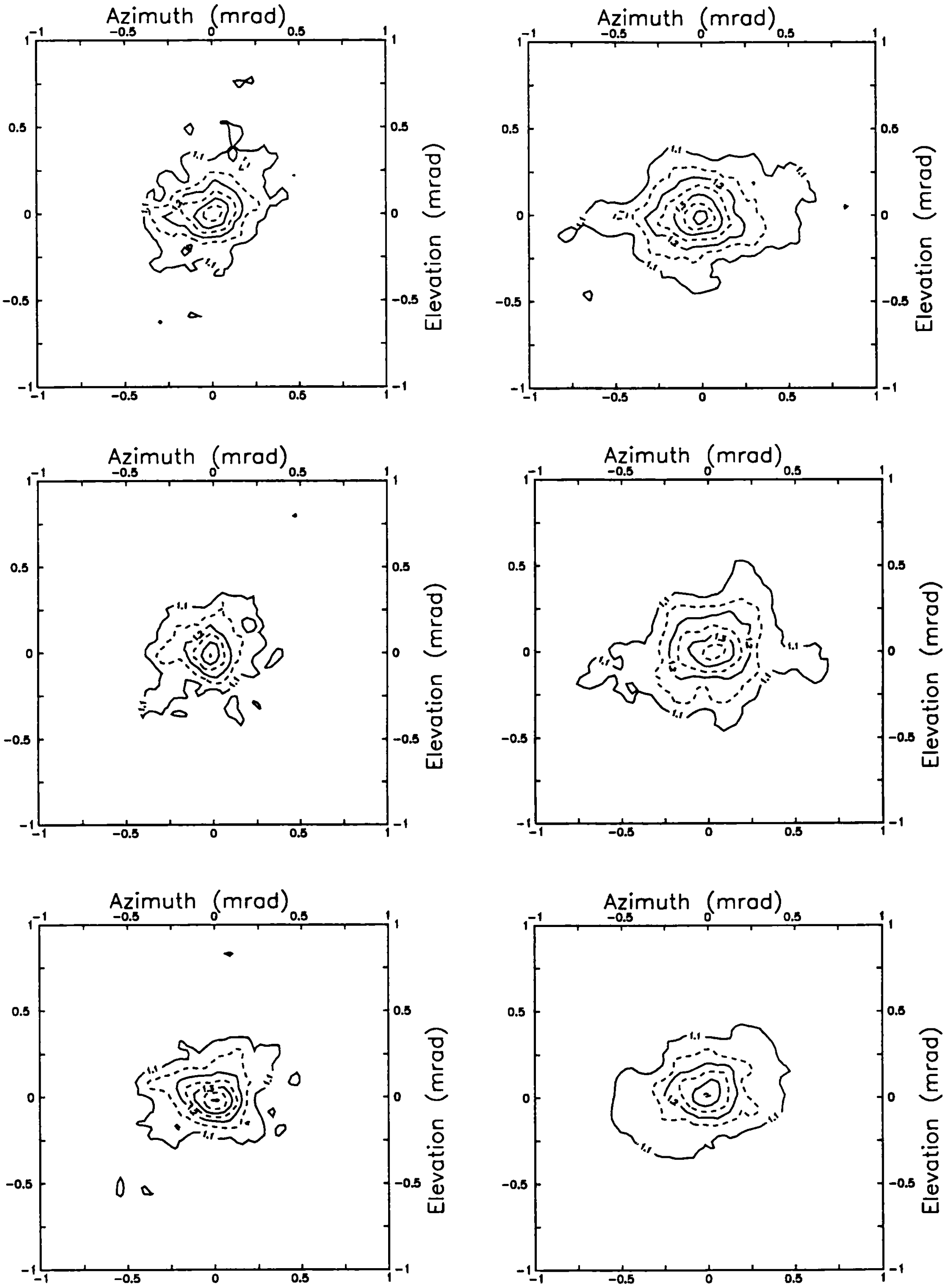

All on porcine muscle with vertical linear polarizers
Native samples on left, coagulated on right
Top:- Fibres vertical. Middle:- Fibres horizontal. Bottom:- Fibres end on

Figure **7.11** Contour plots of coherence peaks from porcine muscle with vertical linearly polarized light and various fibre orientations.

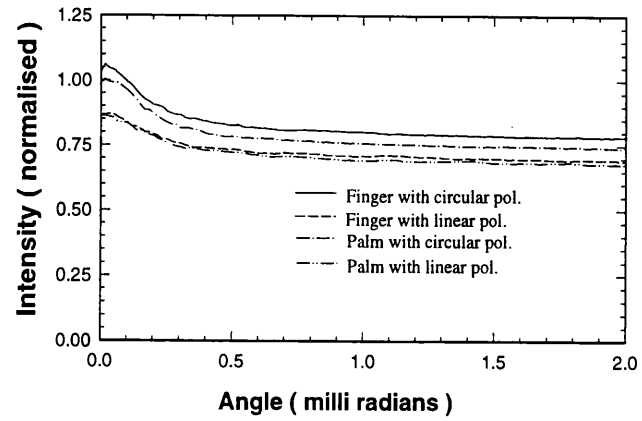

Figure 7.12 Radially averaged coherence peak profiles obtained from an *in vivo* human hand.

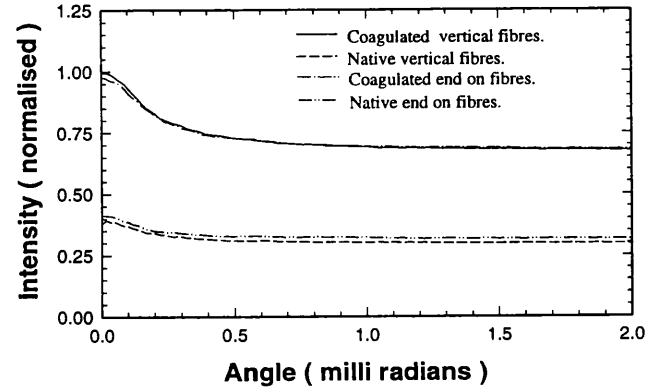

Figure 7.13 Radially averaged coherence peaks for circularly polarized light incident on porcine muscle with various fibre orientations.

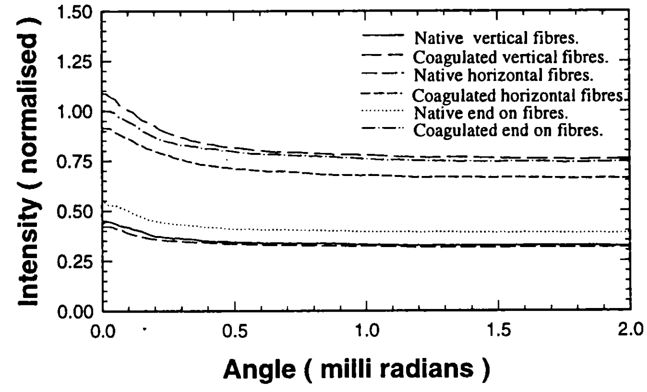

Figure 7.14 Radially averaged coherence peaks for vertical linearly polarized light incident on porcine muscle with various fibre orientations.

7.3 CHAPTER SUMMARY.

The experiments have shown that for 1064 nm light it is possible to extract coherence peaks from a wide variety of biological tissues including those that are in an *in vivo* state. The time for the camera exposure is of the order of a second and once the radial profile is extracted, the processing with a neural network to obtain the optical properties is both fast and robust. The major experimental limitation in these experiments has been a possible drift in the laser power level that was not monitored during the exposure period of the camera. The consequence of this is an experimental uncertainty that is far greater than that possible with more sophisticated equipment. Improvements to the experimental set up are likely to be relatively inexpensive compared to the cost associated with alternative techniques such as photon time of flight measurements.

Experiments on phantom samples have shown that there is currently a problem in extracting the absorption coefficient when both the scattering and absorption effects are low. It is possible that this is a result of photon interactions that for polarized light, do not behave in a scalar manner. Additional work is needed to evaluate such possibilities.

Extraction of the optical coefficients from experimental data that were taken with circularly polarized light gives results that are consistent with previously published data (see chapter 3, section 2.1). The symmetry of the coherence peaks taken with linearly polarized light indicates that low order scattering is not prevalent in the biological tissues examined, a fact that correlates well with the high values of anisotropy factor that the goniometric experiments of previous studies reported. The effect of fibre orientation has been shown to have a possible effect on the optical properties of some biological media.

CONCLUDING REMARKS.

The context of this work has been to continue an ongoing study aimed at producing safer and more reliable methods of laser surgery through the prediction of thermal damage. Although this problem can be split into various sections which can be dealt with separately, the underlying accuracy of any final prediction will be sensitive to the accuracy with which the fundamental optical properties are known. These properties are also of interest to the development and understanding of certain optical diagnostic techniques as well as other therapeutic effects such as Photodynamic Therapy. This thesis addresses this basic problem with a phenomenon that has only been truly evaluated over the last decade and has, as yet, found few applications. Although the idea of using Coherent Backscatter to measure the optical coefficients of biological tissue is not original to this thesis, the method implemented here includes, for the first time, using the absolute backscattered intensity as well as the line shape. The approach taken also overcomes some of the constraints and misinterpretations found in the theory used for the earlier work.

Having assessed the alternative technologies, the method of Coherent Backscattering was evaluated from the point of view of the probing depth and the applicability of diffusion approximation theory. The conclusions are that for the degree of scattering and absorption found in most turbid biological tissues, the probing depth can be considered to be around 5 reduced scattering mean free paths and that diffusion approximation theory is not applicable for a significant portion of the total backscattered light.

A numerical prediction method based on a Monte Carlo model for the light transport was used to predict the effects on a coherence peak of refractive index mismatches, the degree of scattering anisotropy, and the confined illumination geometry. The first of these effects can only be described by approximate analytical mathematics, whilst the last has not, as yet, been addressed by any method other than numerical simulations, and even then only for a top hat profile. The problem of scattering anisotropy has previously been dealt with in an exact manner by certain analytical methods but only in the regime where the scattering anisotropy is weak or is tending towards being totally forward. Although the Monte Carlo method is slow, it is able to predict the line shapes likely to be measured experimentally from biological media.

Two methods were developed and evaluated to extract information from experimentally obtained profiles. One used a non-linear curve fitting routine via interpolation within a large array of Monte Carlo predicted data, whilst the other used an inverse problem solving neural network that had been trained with Monte Carlo predicted data. The network training routine used was a customised hybrid with the network architecture carefully chosen to provide a reasonable level of performance. The advantages of the neural network, namely its speed, robustness, and generalising ability, was proved and the technique used to process experimentally measured data. The neural network was found to be around 4% in error for the scattering coefficient and around 7% for the absorption coefficient when tested on some additional Monte Carlo generated data. It should be realised that some of this error is produced by the statistical ripple noise seen on the Monte Carlo predicted line shape that the neural network is capable of generalising. It is therefore likely that these performance figures are undervaluing the real performance. An interesting alternative would be to measure a large number of calibrated tissues and train the neural network with the experimental results, thus avoiding any experimental artifacts.

The experimental apparatus demonstrated the ability to measure Coherence Peaks in biological media with equipment that was relatively cheap compared to certain alternative methods (e.g. time of flight) and provides a fast acquisition time that coupled with the neural network tool, offers the ability of real time optical coefficient measurement on a timescale only marginally longer than the time exposure of the camera; around one second. The sophistication of the apparatus used was constrained by cost considerations and does not represent the optimal performance that technology can provide. Improvements would include more stable laser output power levels that can be monitored over the time period of the camera exposure, more sensitive cameras with reduced levels of output noise, and superior optics that would enable the system performance to approach the optimal. The data presented covers a series of performance evaluation experiments and those from a set of measurements made on *in vivo* and *in vitro* specimens. The tissue experiments gave results that are comparable to those measured with alternative techniques with the actual level of disagreement being of the same order as between the results from different published studies that use different techniques. The calibration experiments showed an unfortunate trend of disagreement at low levels of scattering. This may be the result of using of scalar model for the vectorial nature light concerning the way in which the total backscattered intensity falls off, in this particular experimental situation, with a drop in the scattering to absorption ratio. This problem could be accounted for if the polarization properties of the biological tissues could be evaluated. This is a problem that has been addressed previously but only with indications that a general behaviour does not exist. The other experimental errors found include the surmountable problem of laser instability and the general inter sample variations. Experiments performed with different states of light polarizations and possible fibre orientations have indicated that they may be able to influence the extracted optical coefficients. True quantitative analysis for this was impossible amongst the levels of uncertainties.

PUBLICATIONS ARISING DURING THE PROGRESS OF THIS THESIS.

Papers;

M. H. Eddowes, T. N. Mills, D. T. Delpy "Monte Carlo simulations of coherent backscatter for identification of the optical coefficients of biological tissues in vivo." Applied Optics **34**. p.2261-2267 (1995).

M. H. Eddowes, T. N. Mills, D. T. Delpy "Determination of the optical coefficients of in vivo biological tissues by analysis of the coherent backscattering lineshape." Proceedings of SPIE. **2323**. (1994).

K. Anson, G. Buonaccorsi, M. Eddowes, A. MacRobert, T. N. Mills, G. Watson "A comparative analysis of laser side-firing devices: a guide to treatment." British Journal of Urology **75**. pp. 328-334 (1995).

M. Essenpreis, P. S. Jones, M. H. Eddowes, G. A. Buonaccorsi, T. N. Mills "A finite element model for laser ablation of tissue." Proceedings of SPIE. **1882**. (1993).

M. Essenpreis, M. H. Eddowes, G. Buonaccorsi, T. N. Mills. "Optical Properties of human prostate and light distributions resulting from a cylindrical illumination geometry." in *Lasers in Medicine* pp. 135-138 (Springer-Verlag, Berlin, 1994).

Aspects of this work have also been personally presented at;

Optical Localization and Slow Waves;

Rank Prize Funds Symposium, Grasmere U.K. 20-23 September 1993

Optical Techniques in Medicine;

Meeting of The Institute of Physical Sciences in Medicine, York U.K. 13-14 April 1994

Waves and Heterogeneous Media;

Workshop, Les Houches France, 21-32 March 1995.

REFERENCES.

1 J. A. S. Carruth, A. L. McKenzie *Medical Lasers*. (Hilger, Bristol, 1986).

2 J. L. Boulnois "Photophysical processes in recent medical laser developments: a review." Lasers in Medical Science. **1**. pp. 47-66 (1986).

3 J. A. Parrish, B. C. Wilson "Current and future trends in laser medicine." Photochemistry and Photobiology. **53**. pp. 731-738 (1991).

4 A. J. Welch, M. Motamedi, S. Rastegar, G. L. LeCarpentier, D. Jansen "Laser thermal ablation." Photochemistry and Photobiology. **53**. pp. 815-823 (1991).

5 S. Krishnamurthy, S. K. Powers "Lasers in Neurosurgery." Lasers in Surgery and Medicine. **15**. pp. 126-167 (1994).

6 R. H. Ossoff, J. A. Coleman, M. S. Courey, J. A. Duncavage, J. A. Werkhaven, L. Reinisch "Clinical applications of lasers in Otolaryngology-Head and neck surgery." Lasers in Surgery and Medicine. **15**. pp. 217-248 (1994).

7 L. I. Deckelbaum "Cardiovascular applications of laser technology." Lasers in Surgery and Medicine. **15**. pp. 315-341 (1994).

8 R. G. Wheeland "Clinical uses of lasers in Dermatology." Lasers in Surgery and Medicine. **16**. pp. 2-23 (1995).

9 H. A. Wigdor, J. T. Walsh, J. D. B. Featherstone, S. R. Visuri, D. Fried, J. L. Waldvogel "Lasers in Dentistry." Lasers in Surgery and Medicine. **16**. pp. 103-133 (1995).

10 B. C. Wilson, M. S. Patterson "The physics of photodynamic therapy." Physics in Medicine and Biology. **31**. pp. 327-360 (1986).

11 B. W. Henderson, T. J. Dougherty "How does photodynamic therapy work?" Photochemistry and Photobiology. **55**. pp. 145-157 (1992).

12 J. Moan "On the diffusion length of singlet oxygen in cells and tissues." Journal of Photochemistry and Photobiology B. **6**. pp. 343-344 (1990).

13 J. T. Allardice, A. M. Abulafi, R. Dean, A. C. Rowland, N. S. Williams "Light delivery systems for adjunctive intraoperative photodynamic therapy." Lasers in Medical Science. **8**. pp. 1-14 (1993).

14 H. J. van Staveren, J. H. Beek, M. Keijzer, W. M. Star "Integrating sphere effect in whole bladder wall photodynamic therapy at violet, green, and red wavelengths." Proceedings of SPIE. **2323**. pp. 13-20 (1994).

15 L. Goldman, J. Rockwell *Lasers in medicine*. (Gordin and Breach, New York, 1971).

16 J. T. Walsh, T. J. Flotte, R. R. Anderson, T. F. Deutsch "Pulsed CO2 laser tissue ablation: Effect of tissue type and pulse duration on thermal damage." Lasers in Surgery and Medicine. **8**. pp. 108-118 (1988).

17 J. T. Walsh, T. F. Deutsch "Pulsed CO2 laser tissue ablation: measurement of the ablation rate." Lasers in Surgery and Medicine. **8**. pp. 264-275 (1988).

18 N. Nishioka S, Y. Domankevitz, V. Venugopalan, D. Bua P "Tissue ablation with a pulsed Nd:YAG laser operating at 1.44μm wavelength." Lasers in Surgery and Medicine. **Suppl 4**. p. 7 (1992).

19 N. S. Nishioka, Y. Domankevitz "Reflectance during pulsed Holmium laser irradiation of tissue." Lasers in Surgery and Medicine. **9**. pp. 375-381 (1989).

20 A. L. McKenzie. "Theoretical limits to soft tissue damage by Er:YAG and Ho:Yag lasers." in *Safety and laser tissue interaction*, eds. H. P. Berlien, G. J. Müller, H. Ringelhan, B. Schaldach (Landsberg, 1989).

21 P. S. Jones. "Development and Characterisation of Holmium and Erbium lasers for the ablation of biological tissue." (Ph.D. Dissertation, University of London, London U.K. 1993).

22 J. T. Walsh, T. J. Flotte, T. F. Deutsch "Er:YAG laser ablation of tissue: Effect of pulse duration and tissue type on thermal damage." Lasers in Surgery and Medicine. **9**. pp. 314-326 (1989).

23 J. T. Walsh, T. J. Flotte, T. F. Deutsch "Er:YAG Laser ablation of tissue: Measurement of ablation rates." Lasers in Surgery and Medicine. **9**. pp. 327-337 (1989).

24 A. L. McKenzie "An extension of the three-zone model to predict depth of tissue damage beneath Er:YAG and Ho:YAG laser excisions." Physics in Medicine and Biology. **34**. pp. 107-114 (1989).

25 V. Artjushenko "Fibre optical delivery systems for surgery, diagnostics and phototherapy." Proceedings of SPIE. **1524**. pp. 249-263 (1991).

26 D. L. Singleton, G. Paraskevopoulous, G. S. Jolly, R. S. Irwin, D. J. McKenney, W. S. Nip, E. M. Farrell, A. J. Higginson "Excimer lasers in cardiovascular surgery: Ablation products and photoacoustic spectrum of arterial wall." Applied Physics Letters. **48**. pp. 878-880 (1986).

27 G. Barbeau, G. S. Abela, T. Tomaru, D. Franzini, J. Seeger "Laser-thermal coagulation of vascular collagen reduces platelet adhesion following balloon angioplasty." Lasers in Surgery and Medicine. **Suppl 3**. p. 14 (1991).

28 I. Nyamekye, J. McEwan, A. MacRobert, C. Bishop, S. Bown "Photodynamic therapy of contractile arterial smooth muscle cells in vitro using aluminium disulphonated phthalocyanine: implications for angioplasty induced intimal hyperplasia." Proceedings of SPIE. **2327**. pp. 332-338 (1994).

29 I. Nyamekye, J. McEwan, A. MacRobert, C. Bishop, S. Bown "Adjunctive arterial injury and photodynamic therapy with aluminium disulphonated phthalocyanine inhibits intimal hyperplasia." Proceedings of SPIE. **2327**. pp. 347-353 (1994).

30 P. Kiefhaber, G. Nath, K. Moritz "Endoscopic control of massive haemorrhage by irradiation with a high powered Nd:YAG laser." Prog. Surg. **15**. pp. 140-155 (1977).

31 M. R. Hetzel, C. Nixon, W. M. Edmonstone "Laser therapy in 100 tracheobronchial tumours." Thorax. **40**. pp. 341-345 (1985).

32 C. P. Swain, S. G. Bown, D. A. W. Edwards, J. S. Kirkham, P. R. Salmon, C. G. Clark "Laser recanalisation of obstructing foregut cancer." British Journal of Surgery. **71**. pp. 112-115 (1984).

33 S. G. Bown, H. Barr, K. Matthewson "Endoscopic treatment of inoperable colorectal cancers with the Nd:YAG laser." British Journal of Surgery. **73**. pp. 949-952 (1986).

34 A. D. Meyers "Laser reimbursement: Who pays for progress?" Lasers in Surgery and Medicine. **10**. pp. 396-400 (1990).

35 A. C. Steger, S. G. Bown, C. G. Clark "Interstitial laser hyperthermia: studies in the normal liver." British Journal of Surgery. **75**. p. 598 (1988).

36 A. C. Steger, W. R. Lees, P. Shorvon, K. Walmsley, S. G. Bown "Multiple-fibre low-power interstitial laser hyperthermia studies in the normal liver." British Journal of Surgery. **79**. pp. 139-145 (1992).

37 A. C. Steger, W. R. Lees, K. Walmsley, S. G. Bown "Interstitial laser hyperthermia: a new approach to local destruction of tumours." British Medical Journal. **299**. pp. 362-365 (1989).

38 A. Masters, A. C. Steger, W. R. Lees, K. M. Walmsley, S. G. Bown "Interstitial laser hyperthermia: a new approach for treating liver metastases." British Journal of Cancer. **66**. pp. 518-522 (1992).

39 K. Anson, K. Seenivasagam, R. Miller, G. Watson "The role of lasers in urology." British Journal of Urology. **73**. pp. 225-230 (1994).

40 K. Matthewson, P. Coleridge-Smith, J. P. O'Sullivan, T. C. Northfield, S. G. Bown "Biological effects of intrahepatic Neodymium:Yttrium-Aluminum-Garnet laser photocoagulation in rats." Gastroenterology. **93**. pp. 550-557 (1987).

41 G. R. E. Meyer-Schwickerath "The history of photocoagulation." Australian and New Zealand Journal of Ophthalmology. **17**. pp. 427-434 (1989).

42 F. A. L'Esperance *Ophthalmic Lasers.* (The C. V. Mosby Co., St. Louis, 1989).

43 J. Hecht "Hedging bets on laser refractive surgery." Laser Focus World. **31**. pp. 55-57 (1995).

44 D. S. Gartry "Treating myopia with the excimer laser: the present position." British Medical Journal. **310**. pp. 979-985 (1995).

45 M. S. Kitai, V. L. Popkov, V. A. Semchishen, A. A. Kharizov "The physics of UV laser cornea ablation." IEEE Journal of Quantum Electronics. **27**. pp. 302-307 (1991).

46 M. Moretti "Surface irregularities puzzle PRK researchers." Biomedical Optics. **2**. p. 10 (1993).

47 S. L. Trokel, R. Srinivasen, B. Braven "Excimer laser surgery of the cornea." American Journal of Ophthalmology. **96**. pp. 710-715 (1983).

48 C. A. Puliafito, R. R. Steinert, T. F. Deutsch "Excimer laser ablation of the cornea and lens: Experimental studies." Ophthalmology. **92**. pp. 742-748 (1985).

49 M. Gordon, S. F. Brint, D. S. Durrie, T. Seiler, M. D. Friedman, N. F. Johnson, M. C. King, D. F. Muller "Photorefractive Keratectomy a 193 nm using an erodible mask." Proceedings of SPIE. **1644**. pp. 11-19 (1992).

50 D. D. Kuck, R. F. Menefore, A. Abarca, M. J. Berry "Corneal shaping by Holmium:YAG laser thermal keratoplasty (LTK)." Biomedical Optics '93 Abstracts. (1993).

51 R. R. Anderson, J. A. Parrish "Microvascular can be selectively damaged using pulsed dye lasers: a basic theory and experimental evidence in human skin." Lasers in Surgery and Medicine. **1**. pp. 263-276 (1981).

52 M. J. C. van Gemert, S. L. Jacques, H. J. C. M. Sterenborg, W. M. Star "Skin Optics." IEEE Transactions on Biomedical Engineering. **36**. pp. 1146-1154 (1989).

53 M. J. C. van Gemert, A. J. Welch, A. P. Amin "Is there an optimal laser treatment for port wine stains?" Lasers in Surgery and Medicine. **6**. pp. 76-83 (1986).

54 M. J. C. van Gemert, J. P. Hulsbergen-Henning "A model approach to laser coagulation of dermal vascular lesions." Archives of Dermatological Research. **270**. pp. 429-439 (1981).

55 M. J. C. van Gemert, W. J. A. de Kleijn, J. P. Hulsbergen-Henning "Temperature behaviour of a port-wine stain during argon laser coagulation." Physics in Medicine and Biology. **27**. pp. 1089-1104 (1982).

56 O. T. Tan, P. Morrison, A. K. Kurban "585 nm for treatment of port wine stains." Plastic Reconstructive Surgery. **86**. pp. 1112-1117 (1990).

57 L. O. Svaasand, T. E. Milner, B. Anvari, L. T. Norvang, B. S. Tanenbaum, S. Kimel, M. W. Berns, J. S. Nelson "Epidermal heating during Laser Induced Photothermolysis of Port Wine Stains; Modelling Melanosomal heating after dynamic cooling the skin surface." Proceedings of SPIE. **2323**. pp. 366-377 (1994).

58 M. Keijzer, J. W. Pickering, M. J. C. van Gemert "Laser beam diameter for port wine stain treatment." Lasers in Surgery and Medicine. **11**. pp. 601-605 (1991).

59 J. W. Pickering "585 nm for the laser treatment of port wine stains: A possible mechanism." Lasers in Surgery and Medicine. **11**. pp. 616-618 (1991).

60 R. Schober, F. Ulrich, T. Sander "Laser induced alteration of collagen substructure allows microsurgical tissue welding." Science. **232**. pp. 1421-1422 (1986).

61 M. Bentz, B. Parva, C. Dickson, J. W. Futrell, P. Johnson "Laser-assisted microvascular anastomoses of human fetal artery, and expanded polytraflouroethylene microconduit." Lasers in Surgery and Medicine. **Suppl. 4**. p. 19 (1992).

62 W. H. Reis, I. D. Miller, M. J. Murphy, J. P. Paul, J. H. Evans "Q-switched ruby laser treatment of tattoos: a 9-year experience." British Journal of Plastic Surgery. **43**. pp. 663-669 (1990).

63 G. M. Watson, S. Murray, S. P. Dretler, J. A. Parrish "The pulsed dye laser for fragmenting urinary calculi." Journal of Urology. **138**. pp. 195-198 (1987).

64 P. Teng, N. S. Nishioka, R. R. Anderson, T. F. Deutsch "Optical studies of pulsed laser fragmentation of biliary calculi." Applied Physics B .**42**. pp. 73-78 (1987).

65 E. Reichel, G. Paltauf, H. Schmidt-Kloiber, K. Groke "A special irrigation liquid to increase the reliability of laser-induced shockwave lithotripsy." Lasers in Surgery and Medicine. **12**. pp. 204-209 (1992).

66 E. Reichel, H. Schmidt-Kloiber "Laser-induced Shock wave Lithotripsy with a regenerative Energy Converter." Lasers in Medical Science. **7**. pp. 423-425 (1992).

67 H. Schmidt-Kloiber, G. Paltauf, E. Reichel "Investigation of the probalistic behaviour of laser induced breakdown in pure water and in aqueous solutions of different concentrations." Journal of Applied Physics. **66**. pp. 4149-4153 (1989).

68 M. D. Stern "In Vivo evaluation of microcirculation by coherent light scattering." Nature. **254**. pp. 57-58 (1975).

69 P. C. Jackson, P. H. Stevens, F. H. Smith, D. Kean, H. Key, P. N. T. Wells "The development of a system for transillumination computed tomography." British Journal of Radiology. **60**. pp. 375-380 (1987).

70 B. Chance, J. S. Leigh, H. Miyake, D. S. Smith, S. Nioka, R. Greenfield, M. Finander, W. Levy, M. Young, P. Cohne, H. Yoshioka, R. Boretsky "Comparison of time resolved and unresolved measurements of deoxyhemoglobin in brain." Procedings of SPIE. **1641**. (1988).

71 R. L. Barbour, H. L. Graber, J. Lubowsky "Imaging of diffusive media by a progressive iterative backprojection method using time-domain data." Proceedings of SPIE. **1641**. (1992).

72 M. Schweiger. "Application of finite element modelling in infrared image reconstruction of scattering media." (Ph.D. Dissertation, University of London. London U.K. 1994).

73 R. A. Elliott, T. Duracz, N. J. McCormick, D. R. Emmons "Experimental test of a time-dependent inverse radiative transfer algorithm for estimating scattering parameters." Journal of the Optical Society of America A. **5**. pp. 366-373 (1988).

74 R. A. Elliott, T. Duracz, N. J. McCormick, D. J. Bossert "Experimental test of a time-dependent inverse radiative transfer algorithm for estimating scattering parameters: addendum." Journal of the Optical Society of America A. **6**. pp. 603-606 (1989).

75 J. P. Payne, J. W. Severinghaus *Pulse Oximetry*. (Springer, Heidelberg, 1986).

76 S. Nakajima, Y. Hirai, H. Tatase, A. Kuse, S. Aoyagi, M. Kishe, K. Yamaguchi "New pulsed type earpiece oximeter." Kokyu To Junkan. **23**. pp. 709-713 (1975).

77 M. Cope, D. T. Delpy "System for long term measurement of cerebral blood and tissue oxygenation on newborn infants by near infrared transillumination." Medical and Biological Engineering and Computing. **26**. pp. 289-294 (1988).

78 M. Cope. "The development of a near infrared spectroscopy system and its application for non invasive monitoring of cerebral blood and tissue oxygenation in the new born infant." (Ph.D. Dissertation, University College London, London U.K. 1991).

79 D. T. Delpy, M. Cope, P. van der Zee, S. Arridge, S. Wray, J. Wyatt "Estimation of optical pathlength through tissue from direct time of flight measurement." Physics in Medicine and Biology. **33**. pp. 1433-1442 (1988).

80 J. S. Wyatt, M. Cope, D. T. Delpy, C. E. Richardson, A. D. Edwards, S. Wray, E. O. R. Reynolds "Quantisation of cerebral blood volume in human infants by near-infrared spectroscopy." Journal of Applied Physiology. **68**. pp. 1089-1091 (1990).

81 A. D. Edwards, J. S. Wyatt, C. Richardson, D. T. Delpy, M. Cope, E. O. R. Reynolds "Cotside measurement of cerebral blood flow in ill pretern infants by near infrared spectroscopy." Lancet. **2**. pp. 770-771 (1988).

82 T. N. Mills, S. M. L. Andrew, M. Essenpreis "Pulsed laser generation and optical detection of thermoelastic waves in arterial tissues." Lasers in Surgery and Medicine. **Suppl 3**. p. 4 (1991).

83 P. C. Beard, R. J. Cornforth, M. Essenpreis, T. N. Mills. "Photoacoustic response of post mortem human aorta to 10 ns laser pulses." in *Lasers in Meidcine. Proceedings of the 11th International congress, Munich* eds. W. Waidelich, R. Waidelich, A. Hofstetter pp. 148-151 (Springer-Verlag, Berlin, 1993).

84 K. M. Quan, G. B. Christison, H. A. MacKenzie, P. Hodgson "Glucose determination by a pulsed photoacoustic technique, an experimental study using gelatin-based tissue phantoms." Physics in Medicine and Biology. **38**. p. 1922 (1993).

85 G. B. Christison, H. A. MacKenzie "Laser photo acoustic determination of physiological glucose concentrations in human whole blood." Medical and Biological Engineering and Computing. pp. 284-290 (May 1993).

86 H. A. MacKenzie, G. B. Christison, P. Hodgson, D. Blanc "A laser photoacoustic sensor for analyte detection in aqueous systems." Sensors and Actuators B. **11**. pp. 213-220 (1993).

87 A. J. Welch "The thermal response of laser irradiated tissue." IEEE Journal of Quantum Electronics. **20**. pp. 1471-1481 (1984).

88 A. J. Welch, E. H. Wissler, L. A. Priebe "Significance of blood flow in calculations of temperature in laser irradiated tissue." IEEE Transactions on Biomedical Engineering. **27**. pp. 164-166 (1980).

89 A. Shitzer *General analysis of the bioheat equation.* Heat Transfer in Medicine and Biology eds. R. Eberhart C, A. Shitzer (Plenum Press, New York, 1985).

90 M. J. C. van Gemert, A. J. Welch "Time constants in thermal laser medicine." Lasers in Surgery and Medicine. **9**. pp. 405-421 (1989).

91 M. J. P. Brugmans, J. Kemper, G. H. M. Gijsbers, F. W. van der Meulen, M. J. C. van Gemert "Temperature response of biological materials to pulsed non-ablative CO2 laser irradiation." Lasers in Surgery and Medicine. **11**. pp. 587-594 (1991).

92 M. Essenpreis. "Thermally induced changes in optical properties of Biological Tissues." (Ph.D. Dissertation, University of London, London U.K. 1992).

93 A. Roggan, G. Müller "2 D computer simulations for real time irradiation planning of laser induced interstitial thermotherapy (LITT)." Proceddings of SPIE. **2327**. (1994).

94 A. E. Profio "Fluorescence bronchoscopy for location of carcinoma in situ." Medical Physics. **10**. pp. 35-39 (1983).

95 A. E. Profio, J. Sarnaik. "Florescence of HPD for tumour detection and dosimetry in photoradiation therapy." in *Porphyrin localization and treatment of tumours* eds. Doiron, Gomer pp. 163-175 (Liss, New York, 1989).

96 A. E. Profio, M. J. Carvlin, J. Sarnaik, L. R. Wudl. "Fluorecence in hematoporphyrin-derivative for detection and characterisation of tumours." in *Porphyrins in Tumour Phototherapy* eds. A. Andreoni, Cubeddu. pp. 321-337 (1984).

97 C. F. Bohren, D. R. Huffman *Absorption and scattering by small particles.* (John Wiley and Sons, New York, 1983).

98 L. G. Henyey, J. L. Greenstein "Diffuse radiation in the galaxy." Journal of Astrophysics. **86**. pp. 70-83 (1937).

99 A. Ishimaru *Wave propagation and the scattering in random media.* Vols. 1 & 2 (Academic Press, New York, 1978).

100 M. Kerker *The scattering of light and other electromagnetic radiation.* (Academic Press, New York, 1969).

101 P. Latimer, A. Brunsting, B. E. Pyle, C. Moore "Effects of asphericity on single particle scattering." Applied Optics. **17**. pp. 3152-3158 (1978).

102 P. Koepke, M. Hess "Scattering functions of tropospheric aerosols: the effects of non spherical particles." Applied Optics. **27**. pp. 2422-2430 (1988).

103 M. S. Patterson, B. C. Wilson, D. R. Wyman "The propagation of optical radiation in tissue I. Models of radiation transport and their application." Lasers in Medical Science. **6**. p. 155 (1991).

104 S. Chandrasekhar *Radiative transfer.* (Dover, New York, 1960).

105 H. C. van der Hulst *Light scattering by small particles.* (Dover, New York, 1957).

106 B. R. Barkstrom "Some effects of multiple scattering on the distribution of solar radiation in snow and ice." Journal of Glaciology **63**. pp. 357-368 (1972).

107 J. Canosa, H. R. Penafiel "A direct solution of the radiative transfer equation: Application to Rayleigh and Mie atmospheres." Journal of Quantum Spectroscopy and Radiative Transfer. **13**. pp. 21-39 (1972).

108 W. M. Star, J. P. A. Marijnissen, M. J. C. van Gemert "Light dosimetry in optical phantoms and in tissues: I. Multiple flux and transport theory." Physics in Medicine and Biology. **33**. pp. 437-454 (1988).

109 A. Zardecki, S. A. W. Gerstl, R. E. DeKinder Jr. "Two- and three-dimensional radiative transfer in the diffusion approximation." Applied Optics **25**. pp. 3508-3515 (1986).

110 K. Furutsu "Diffusion equation derived from space time transport equation." Journal of the Optical Society of America. **70**. pp. 360-366 (1980).

111 G. Yoon, S. A. Prahl, A. J. Welch "Accuracies of the diffusion approximation and its similarity relations for laser irradiated biological media." Applied Optics. **28**. pp. 2250-2255 (1989).

112 V. Allen, A. L. McKenzie "The modified diffusion dipole model." Physics in Medicine and Biology. **36**. pp. 1621-1638 (1991).

113 M. R. Arnfield, J. Tulip, M.S. McPhee "Optical propagation in tissue with anisotropic scattering." IEEE Transactions on Biomedical Engineering. **35**. pp. 372-381 (1988).

114 W. M. Star "Comparing the P3-approximation with diffusion theory and with Monte Carlo calculations of light propagation in a slab geometry." SPIE series. **5**. pp. 146-154 (1989).

115 M. Keijzer, W. M. Star, P. R. M. Storchi "Optical diffusion in layered media." Applied Optics. **27**. pp. 1820-1824 (1988).

116 S. R. Arridge, M. Schweiger, M. Hiraoka, D. T. Delpy "A finite element approach for modelling photon transport in tissue." Medical Physics. **20**. pp. 299-309 (1993).

117 N. Metropolis, S. Ulam "The Monte Carlo Method." Journal of the American Statistical Association. **44**. 247 pp. 335-341 (1949).

118 D. E. Raeside "Monte Carlo principles and applications." Physics in Medicine and Biology. **21**. pp. 181-197 (1976).

119 I. Lux, L. Koblinger *Monte Carlo particle transport methods: Neutron and photon calculations."* (CRC press, Boca Raton, Florida, 1991).

120 M. H. Wachter, W. H. Ellett, G. L. Brownell "Absorption of Gamma Radiation in NaI Well Crystals." The Review of Scientific Instruments. **31**. 6 pp. 626-630 (1960).

121 W. H. Ellett, A. B. Callahan, G. L. Brownell "Gamma-ray dosimetry of internal emitters. Monte Carlo calculations of absorbed dose from point sources." British Journal of Radiology. **37**. 451 pp. 45-52 (1964).

122 W. H. Ellett, A. B. Callahan, G. L. Brownell "Gamma-ray Dosimetry of internal emitters II: Monte Carlo calculations of absorbed dose from uniform sources." British Journal of Radiology. **38**. 451 pp. 541-544 (1965).

123 J. J. DePalma, J. Gasper "Determining the optical properties of photographic emulsions by the Monte Carlo method." Photographic Science and Engineering. **16**. pp. 181-191 (1972).

124 R. M. Lerner, J. D. Summers "Monte Carlo description of time- and -space-resolved multiple forward scatter in natural water." Applied Optics. **21. No.5**. pp. 861-869 (1981).

125 B. C. Wilson, G. Adam "A Monte Carlo model for the absorption and flux distributions of light in tissue." Medical Physics. **10**. pp. 824-830 (1983).

126 S. A. Prahl, M. Keijzer, S. L. Jacques, A. J. Welch "A Monte Carlo model of light propagation in tissue." SPIE Institute Series. **IS 5**. pp. 102-111 (1989).

127 J. D. Hardy, H. T. Hammel, D. Murgatroyd "Spectral transmittance and reflectance from excised human skin." Journal of Applied Physiology. **9**. pp. 231-242 (1984).

128 W. A. G. Bruls, J. C. Leun "Forward scattering properties of human epidermal layers." Photochemistry and Photobiology. **40**. pp. 231-242 (1984).

129 S. L. Jacques, C. A. Alter, S. A. Prahl "Angular dependence of HeNe laser light scattering by human dermis." Lasers in the Life Sciences. **1**. pp. 309-333 (1987).

130 S. T. Flock, B. C. Wilson, M. S. Patterson "Optical attenuation coefficients and scattering phase functions of tissues and phantom materials at 633 nm." Medical Physics. **14**. pp. 835-841 (1987).

131 R. Marchesini, A. Bertoni, S. Andreola, E. Melloni, A. E. Sichirollo "Extinction and absorption coefficients and scattering phase functions of human tissues in vitro." Applied Optics. **28**. pp. 2318-2324 (1989).

132 H. Key, E. R. Davies, P. C. Jackson, P. N. T. Wells "Optical attenuation characteristics of breast tissues at visible and near-infrared wavelengths." Physics in Medicine and Biology. **36**. pp. 579-590 (1991).

133 P. van der Zee. "Measurement and modelling of the optical properties of human tissue in the near infra red." (Ph.D. Dissertation, University of London, London U.K. 1993).

134 F. P. Bolin, L. E. Preuss, R. C. Taylor, R. J. Ference "Refractive index of some mammalian tissues using a fiber optic cladding method." Applied Optics. **28**. pp. 2297-2302 (1989).

135 B. C. Wilson, M. S. Patterson, S. T. Flock "Indirect versus direct techniques for the measurement of the optical properties of tissues." Photochemistry and Photobiology. **46**. pp. 601-698 (1987).

136 B. C. Wilson, S. L. Jacques "Optical reflectance and transmittance of tissues: Principles and applications." IEEE Journal of Quantum Electronics **26**. pp. 2186-2199 (1990).

137 J. W. Pickering, S. A. Prahl, N. van Wieringen, J. F. Beek, H. J. C. M. Sterenborg, M. J. C. van Gemert "Double-integrating-sphere system for measuring the optical properties of tissue." Applied Optics. **32**. 4 pp. 399-410 (1993).

138 J. W. Pickering, C. J. M. Moes, H. J. C. M. Sterenborg, S. A. Prahl, M. J. C. van Gemert "Two integrating spheres with an intervening scattering sample." Journal of the Optical Society of America A. **9**. pp. 621-631 (1992).

139 W. F. Cheong, S. A. Prahl, A. J. Welch "A review of the optical properties of biological tissues." IEEE Journal of Quantum Electronics. **26**. 12 pp. 2166-2185 (1990).

140 P. Kubelka "New contributions to the optics of intensely light- scattering materials. Part I." Journal of the Optical Society of America. **38**. pp. 448-457 (1948).

141 P. Kubelka "New contributions to the optics of intensely light-scattering materials. Part II." Journal of the Optical Society of America. **44**. pp. 330-335 (1954).

142 M. J. C. van Gemert, A. J. Welch, W. M. Star, M. Motamedi, W. F. Cheong "Tissue Optics for a slab geometry in the diffusion approximation." Lasers in Medical Science. **2**. pp. 295-302 (1987).

143 M. J. C. van Gemert, W. M. Star "Relations between the Kubelka- Munk and the transport equation models for anisotropic scattering." Lasers in the Life Sciences. **1**. pp. 287-298 (1987).

144 S. A. Prahl, M. C. van Gemert, A. J. Welch "Determining the optical properties of turbid media by using the adding-doubling method." Applied Optics. **32**. 4 pp. 559-568 (1993).

145 W. J. Wiscombe "On initialization, error and flux conservation in the doubling method." Journal of Quantum Spectroscopy and Radiation Transfer. **16**. pp. 637-658 (1976).

146 W. J. Wiscombe "Doubling initialization revisited." Journal of Quantum Spectroscopic Radiative Transfer. **18**. pp. 245-248 (1977).

147 P. van der Zee, M. Essenpreis, D. T. Delpy, M. Cope "Accurate determination of the optical properties of biological tissues using a Monte Carlo inversion technique." Proceedings ICO Florence Italy. pp. 125-128 (1991).

148 A. Roggan, H. Albrecht, K. Dörschel, O. Minet, G. Müller "Experimental set-up and Monte Carlo model for the determination of optical tissue properties in the wavelength range 330-1100 nm." Proceedings of SPIE. **2323**. (1994).

149 V. V. Tuchin, E. R. Utz, I. V. Yaroslavsky "Tissue optics, light distribution, and spectroscopy." Optical Engineering **33**. pp. 3178-3188 (1994).

150 B. C. Wilson, M. S. Patterson, D. M. Burns "Effect of photosensitiser concentration in tissue on the penetration depth of photoactivation light." Lasers in Medical Science. **1**. pp. 235-244 (1986).

151 M. S. Patterson, B. C. Wilson, J. W. Feather, D. M. Burns, W. Pushka "The measurement of dihematoporphyrin ether concentration in tissue by reflectance spectrophotometry." Photochemistry and Photobiology. **46**. pp. 337-344 (1987).

152 H. Vijverberg, S. Thomsen, S. Jacques, A. Oraevsky "Evaluation of a time-resolved stress detection method to determine tissue optical properties." Proceedings of SPIE. **2323**. pp. 312-316 (1994).

153 J. M. Schmitt, A. Knüttel, R. F. Bonner "Measurement of optical properties of biological tissues by low-coherence reflectometry." Applied Optics. **32**. 30 pp. 6032-6042 (1993).

154 J. H. Torres, A. J. Welch, I. Çilesiz, M. Motamedi "Tissue optical property measurements: Overestimation of absorption coefficient with spectrophotometric techniques." Lasers in Surgery and Medicine. **14**. pp. 249-257 (1994).

155 D. R. Doiron, L. R. Svaasand, A. E. Profio. "Light dosimetry in tissue: application to photoradiation therapy." in *Porphyrin Photosensitization* ed. Kessel pp. 63-76 (Plenum, New York, 1983).

156 L. O. Svaasand, R. Ellingsen "Optical properties of human brain." Photochemistry and Photobiology. **38**. pp. 293-299 (1983).

157 L. O. Svaasand, R. Ellingsen "Optical penetration in human intracranial tumours." Photochemistry and Photobiology. **41**. pp. 73-76 (1985).

158 B. C. Wilson, W. P. Jeeves, D. M. Lowe "In vivo and post mortem measurements of the attenuation spectra of light in mammalian tissues." Photochemistry and Photobiology. **42**. pp. 153-162 (1985).

159 P. J. Muller, B. C. Wilson "An update on the penetration depth of 630 nm light in normal an malignant brain tissues in vivo." Physics in Medicine and Biology. **31**. pp. 1295-1297 (1986).

160 M. S. Patterson, E. Schwartz, B. C. Wilson "Quantitative reflectance spectrophotometry for the noninvasive measurement of photosensitiser concentration in tissue during photodynamic therapy." Proceedings of SPIE. **1065**. pp. 115-122 (1989).

161 B. Chance "Comparison of time resolved and unresolved measurements of deoxyhemoglobin in brain." Proceedings of the National Academy of Science USA. **85**. pp. 4971-4975 (1988).

162 M. S. Patterson, B. Chance, B. C. Wilson "Time resolved reflectance and transmittance for the non-invasive measurement of tissue optical properties." Applied Optics. **28**. pp. 2331-2336 (1989).

163 J. R. Lakowicz, K. Berndt, M. L. Johnson "Frequency and time domain measurements of photon migration in tissues." Photochemistry and Photobiology. **49**. p. 825 (1989).

164 A. Kienle, L. Lilge, M. S. Patterson, B. C. Wilson, R. Hibst, R. Steiner "Investigation of multi-layered tissue with in-vivo reflectance measurements." Proceedings of SPIE. **2326**. (1994).

165 G. M. Hale, M. R. Querry "Influence of temperature on the spectrum of water." Journal of the Optical Society of America. **62**. pp. 1103-1108 (1972).

166 P. Parsa, S. L. Jacques, N. S. Nishioka "Optical properties of rat liver between 350 and 2200 nm." Applied Optics. **28**. pp. 2325-2330 (1989).

167 J. L. Karagiannes, Z. Zhang, B. Grossweiner, L. I. Grossweiner "Applications of the 1-D diffusion approximation to the optics of tissues and tissue phantoms." Applied Optics. **28**. pp. 2311-2317 (1989).

168 G. J. Derbyshire, D. K. Bogen, M. Unger "Thermally induced optical property changes in myocardium at 1.06 µm." Lasers in Surgery and Medicine. **10**. pp. 28-34 (1990).

169 M. Essenpreis, P. van der Zee, T. N. Mills "Monte Carlo modelling of light transport in tissue: The effect of laser coagulation on light distributions." Proceedings of SPIE. **1524**. pp. 122-137 (1991).

170 M. Essenpreis, P. van der Zee, T. N. Mills. "Changes of optical coefficients of rat liver in vitro during pulsed Nd:YAG laser irradiation." in *Proceedings of Optics in the Life Sciences* ed. G. von Bally (1992).

171 R. Agah, M. Motamedi, P. Dalmia, J. R. Spears "Changes in the optical constants of thermally damaged arterial tissue as a function of wavelength." Lasers in Surgery and Medicine. **Suppl. 2**. pp. 15-16 (1990).

172 R. van Hillegersberg, J. W. Pickering, M. Aalders, J. F. Beek "Optical properties of rat liver and tumour at 633 nm and 1064 nm: Photofrin enhances scattering." Lasers in Surgery and Medicine. **13**. pp. 31-39 (1993).

173 R. Splinter, R. H. Svenson, L. Littmann "In vitro optical properties of myocardium at 1064 nm before and after Nd:YAG laser irradiation." Lasers in Surgery and Medicine. **Suppl. 2**. p. 63 (1990).

174 R. Splinter, R. H. Svenson, L. Littmann, J. R. Tuntelder, C. H. Chuang, G. P. Tatsis, M. Thompson "Optical properties of normal, diseased, and laser photocoagulated myocardium at the Nd:YAG wavelength." Lasers in Surgery and Medicine. **11**. pp. 117-124 (1991).

175 J. W. Pickering, P. Posthumus, J. C. van Gemert "Continuous measurement of the heat-induced changes in the optical properties (at 1064 nm) of Rat liver." Lasers in Surgery and Medicine. **15**. pp. 200-205 (1994).

176 J. Reichman "Determination of absorption and scattering coefficients for nonhomogeneous media 1: Theory." Applied Optics. **12**. pp. 1811-1815 (1973).

177 W. G. Egan, T. Hilgeman, J. Reichman "Determination of absorption and scattering coefficients for nonhomogeneous media 2: Experiment." Applied Optics. **12**. pp. 1816-1823 (1973).

178 G. M. Hale, M. R. Querry "Optical constants of water in the 200 nm to 200 µm wavelength region." Applied Optics. **12**. pp. 555-563 (1973).

179 K. F. A. Ross *Phase contrast and interference microscopy for cell biologists.* (Arnold, London, 1967).

180 A. S. Martinez. "Statstique de polarisation et effet Faraday en diffusion multiple de la lumiere." (PhD. Thesis, Université Joseph Fourier, Grenoble France, 1992).

181 A. S. Martinez, R. Maynard. "Polarization statistics in multiple scattering of light: a Monte Carlo approach." in *Localization and propagation of classical waves in random and periodic structures* ed. C. M. Soukoulis (Plenum Publishing Corporation, New York, 1994).

182 G. Jarry, O. Schlee, O. Duhamel, J. Virmont, L. Poupinet, B. Clairac, M. Derrien, D. Yeddou "Coherent transmission of polarized light through mammalian tissue." Proceedings of SPIE. **2326**. (1994).

183 J. P. A. Marijnissen, W. M. Star "Quantitative light dosimetry in vitro and in vivo." Lasers in Medical Science. **2**. pp. 235-242 (1987).

184 H. J. van Staveren, C. J. M. Moes, J. van Marle, S. A. Prahl, M. J. C. van Gemert "Light scattering in Intralipid-10% in the wavelength range of 400 - 1100 nm." Applied Optics. **30**. pp. 4507-4514 (1991).

185 S. T. Flock, S. L. Jacques, B. C. Wilson, W. Star, M. J. C. van Gemert "Optical Properties of Intralipid: A Phantom Medium for Light Propagation Studies." Lasers in Surgery and Medicine. **12**. pp. 510-519 (1992).

186 S. J. Madsen, M. S. Patterson, B. C. Wilson "The use of india ink as an optical absorber in tissue-simulation phantoms." Physics in Medicine and Biology. **37**. pp. 985-993 (1992).

187 M. Firbank. "The design, calibration and usage of a solid scattering and absorbing phantom for near infra red spectroscopy." (Ph.D. Dissertation, University of London, London U.K. 1994).

188 M. Firbank, D. T. Delpy "A design for a stable and reproducible phantom for use in near infra red imaging and spectroscopy." Physics in Medicine and Biology. **38**. pp. 847-853 (1993).

189 M. Firbank, D. T. Delpy "A phantom for the testing and calibration of near infra-red spectrometers." Physics in Medicine and Biology. **39**. pp. 1509-1513 (1994).

190 J. M. Hammersley, D. C. Handscomb *Monte Carlo Methods.* (Methuen, London, 1964).

191 M. Essenpreis, T. N. Mills, P. van der Zee "Modelling of Laser coagulation: Light distributions in Nd:YAG laser treated biological tissue."

in *Laser in Medicine* ed. W. Waidelich pp. 351-354 (Springer, Berlin, 1992).

192 G. Eason, A. R. Veitch, R. M. Nisbet, F. W. Turnbull "The theory of the back-scattering of light by blood." Journal of Physics D: Applied Physics. **11**. pp. 1463-1479 (1978).

193 R. F. Bonner, R. Nossal, S. Havlin, G. H. Weiss "Model for photon migration in turbid biological media." Journal of the Optical Society of America A. **4**. pp. 423-432 (1987).

194 G. H. Weiss, R. Nossal, R. F. Bonner "Statistics of penetration depth of photons re-emitted from irradiated tissue." Journal of Modern Optics. **36**. pp. 349-359 (1989).

195 S. R. Arridge, M. Cope, D. T. Delpy "The theoretical basis for the determination of optical pathlengths in tissues: temporal and frequency analysis." Physics in Medicine and Biology. **37**. pp. 1531-1650 (1992).

196 S. Feng, F. Zeng, B. Chance "Monte Carlo simulations of photon migration path distributions in multiple scattering media." Proceedings of SPIE. **1888**. pp. 78-89 (1993).

197 W. Cui, L. E. Ostrander "The relationship of surface reflectance measurements to optical properties of layered biological media." IEEE Transactions on Biomedical Engineering. **39**. pp. 194-201 (1992).

198 M. P. van Albada, D. S. Wiersma, A. Lagendijk. "Experimental Evidence for Loop-type photon trajectories in random media with strong disorder." in *Advances in optical imaging and photon migration, Technical digest* pp. 74-77 (Optical Society of America, Washington DC, 1994).

199 B. A. van Tiggelen, A. Lagendijk. "Recurrent scattering between dielectric spheres." in *Advances in optical imaging and photon migration, Technical digest* pp. 80-81 (Optical Society of America, Washington DC, 1994).

200 D. S. Wiersma, M. P. van Albada, A. Lagendijk. "Accurate analysis of coherent backscattering revealing recurrent scattering of light in disordered media." in *Advances in optical imaging and photon migration, Technical digest* p. 165-168 (Optical Society of America, Washington DC, 1994).

201 M. B. van der Mark. "Propagation of light in disordered media: A search for Anderson Localization." (Ph.D. Dissertation, Universiteit van Amsterdam. 1990).

202 E. Akkermans, P. E. Wolf, R. Maynard, G. Maret "Theoretical study of the coherent backscattering of light by disordered media." Journal of Physics France. **49**. pp. 77-98 (1988).

203 P. den Outer. "Multiple light scattering in random media: Coherent backscattering and imaging." (Ph.D. Dissertation, Universiteit van Amsterdam, Amsterdam. 1995).

204 P. W. Anderson "Absence of diffusion in certain random lattices." Physical Review. **109**. pp. 1492-1505 (1953).

205 P. Sheng *Scattering and localization of classical waves in random media.* (World Scientific, Singapore, 1990).

206 T. Ando, H. Fukuyama *Anderson localization.* (Springer, Berlin, 1988).

207 M. B. van der Mark, M. P. van Albada, A. Lagendijk "Light scattering in strongly scattering media: Multiple scattering and weak localization." Physical Review B. **37**. pp. 3575-3592 (1988).

208 W. van Hearingen, D. Lenstra *Analogies in optics and micro electronics.* (Kluwer, Dordrecht, 1990).

209 A. Schuster "Radiation through a foggy atmosphere." The Astrophysical Journal. **21**. pp. 1-22 (1905).

210 D. A. De Wolf "Electromagnetic reflection from an extended Turbulent Medium: Cumulative forward-scatter single-backscatter approximation." IEEE transactions on Antennas and propagation. **AP-19**. 2 pp. 254-262 (1971).

211 A. Lagendijk, M. P. van Albada, M. B. van der Mark "Localization of light: the quest for the White Hole." Physica. **140A**. pp. 183-190 (1986).

212 Y. Kuga, A. Ishimaru "Retroreflectance from a dense distribution of spherical particles." Journal of the Optical Society of America A. **1**. pp. 831-835 (1984).

213 P. E. Wolf, G. Maret "Weak localisation and coherent backscattering of photons in disordered Media." Physics Review Letters. **55**. pp. 2696-2699 (1985).

214 Y. Kuga, L. Tsang, A. Ishimaru "Depolarization effects of the enhanced retroreflectance from a dense distribution of spherical particles." Journal of the Optical Society of America A. **2**. pp. 616-618 (1985).

215 M. P. van Albada, A. Lagendijk "Observation of weak localization of light in a random medium." Physics Review Letters. **55**. pp. 2692-2695 (1985).

216 L. Tsang, A. Ishimaru "Backscattering enhancement of random discrete scatterers." Journal of the Optical Society of America A. **1**. pp. 836-839 (1984).

217 L. Tsang, A. Ishimaru "Theory of backscattered enhancement of random discrete isotropic scatterers based on the summation of all ladder and cyclical terms." Journal of the Optical Society of America A. **2**. pp. 1331-1338 (1985).

218 N. C. Bruce, J. C. Dainty "Multiple scattering from rough surfaces using the Kirchoff approximation." Journal of Modern Optics. **38**. pp. 579-590 (1991).

219 J. C. Dainty. "The opposition effect in Volume and surface scattering." in *International trends in optics* pp. 207-218 (Academic Press, London, 1991).

220 M.-J. Kim, J. C. Dainty, A. T. Friberg, A. J. Sant "Experimental study of enhanced backscattering from one- and two- dimensional random rough surfaces." Journal of the Optical Society of America A. **7**. pp. 569-577 (1990).

221 A. N. Bogaturov, A. A. D. Canas, J. C. Dainty, A. S. Gurvich, V. A. Myakinin, C. J. Solomon, N. J. Wooder "Observation of the enhancement of coherence by backscattering through turbulence." Optics Communications. **87**. pp. 1-4 (1992).

222 E. Akkermans, P. E. Wolf, R. Maynard "Coherent Backscattering of light by disordered media: Analysis of the peak line shape." Physics Review Letters. **56**. 14 pp. 1471-1474 (1986).

223 P. E. Wolf, G. Maret, E. Akkermans, R. Maynard "Optical coherent backscattering by random media: an experimental study." Journal of Physics France. **49**. pp. 63-75 (1988).

224 A. Lagendijk, R. Vreeker, P. De Vries "Influence of internal reflections on diffusive transport in strongly scattering media." Physics Letters A. **136**. 1 pp. 81-88 (1989).

225 I. Freund, R. Berkovits "Surface reflections and optical transport through random media: Coherent backscattering, optical memory effect, frequency, and dynamical correlations." Physical Review B. **41**. pp. 496-503 (1990).

226 J. X. Zhu, D. J. Pine, D. A. Weitz "Internal reflection of diffusive light in random media." Physical Review A. **44**. pp. 3948-3959 (1991).

227 P. M. Saulnier, G. H. Watson "Role of surface reflectivity in coherent backscattering measurements." Optics Letters. **17**. pp. 946-948 (1992).

228 T. M. Nieuwenhuizen, J. M. Luck "Skin layer of diffusive media." Physical Review E. **48**. pp. 569-588 (1993).

229 D. J. Durian "Influence of boundary reflection and refraction on diffusive photon transport." Physical Review E. **50**. pp. 857-866 (1994).

230 M. Ospeck, S. Fraden "Influence of reflecting boundaries and finite interfacial thickness on the coherent backscattering cone." Physical Review E. **49**. pp. 4578-4589 (1994).

231 E. E. Gorodnichev, S. L. Dudarev, D. B. Rogozkin "Coherent Backscattering enhancement under conditions of weak wave localization in disordered 3D and 2D systems." Sov. Phys. JETP. **69**. 3 pp. 481-490 (1990).

232 E. Gorodnichev E, S. Dudarev L, D. Rogozkin B "Coherent wave backscattering by random medium. Exact solution of the albedo problem." Physics Letters A. **144**. pp. 48-54 (1990).

233 V. D. Ozrin "Exact solution for coherent backscatter from a semi-infinite random medium of anisotropic scatterers." Physics Letters A. **162**. pp. 341-345 (1992).

234 E. Amic, J. M. Luck "Anisotropic multiple scattering in diffusive media." Physical Review E. Submitted for publication. (1995).

235 Y. N. Barabanenkov, V. D. Ozrin "Diffusion approximation in the theory of weak localization of radiation in a discrete random medium." Radio Science. **26**. pp. 747-750 (1991).

236 M. P. van Albada, M. B. van der Mark, A. Lagendijk "Observation of weak localisation of light in a finite slab: Anisotropy effects and light-path Classification." Physics Review Letters. **58**. pp. 361-364 (1987).

237 R. Eisma. "Computersimulaties van lichtverstrooiing aan random media." (M.Sc Thesis, Universiteit van Amsterdam. 1990).

238 M. P. van Albada, M. B. van der Mark, A. Lagendijk "Polarisation effects in weak localization of light." Journal of Physics D: Applied Physics. **21**. pp. S28-S31 (1988).

239 M. P. van Albada, A. Lagendijk "Vector character of light in weak localization: Spatial anisotropy in coherent backscattering from a random medium." Physical Review B. **36**. 4 pp. 2353-2356 (1987).

240 R. Vreeker, M. P. van Albada, R. Sprik, A. Lagendijk "Femtosecond time-resolved measurements of weak localization of light." Physics Letters A. **132**. pp. 51-54 (1988).

241 J. M. Drake, A. Z. Genack "Observation of Nonclassical Optical Diffusion." Physics Review Letters. **63**. pp. 259-262 (1989).

242 S. Etemad, R. Thompson, M. J. Andrejco "Weak localization of photons: Termination of coherent random walks by Absorption and confined Geometry." Physics Review Letters. **59**. pp. 1420-1423 (1987).

243 K. M. Yoo, F. Liu, R. R. Alfano "Biological materials probed by the temporal and angular profiles of the backscattered ultrafast laser pulses." Journal of the Optical Society of America B. **7**. pp. 1685-1693 (1990).

244 K. M. Yoo, G. C. Tang, R. R. Alfano "Coherent backscattering of light from biological tissues." Applied Optics. **29**. pp. 3237-3239 (1990).

245 K. M. Yoo, K. Arya, G. C. Tang, J. L. Birman, R. R. Alfano "Coherent backscattering of a pico-second pulse from a disordered medium: Analysis of the pulse shape in the time domain." Physical Review A. **39**. pp. 3728-3731 (1989).

246 K. M. Yoo, Y. Takiguchi, R. R. Alfano "Dynamic effect of weak localization on the light scattering from random media using ultrafast laser technology." Applied Optics. **28**. pp. 2343-2349 (1989).

247 G. Yoon, D. N. Ghosh Roy, R. C. Straight "Coherent backscattering in biological media: Measurement and estimation of optical properties." Applied Optics. **32**. pp. 580-585 (1993).

248 M. Kaveh, M. Rosenbluh, I. Edrei, I. Freund "Weak localization and light scattering from disordered solids." Physics Review Letters. **57**. 16 pp. 2049-2052 (1986).

249 C. M. Bishop "Neural networks and their applications." Review of Scientific Instruments. **65**. pp. 1803-1833 (1994).

250 J. W. Clark "Neural network modelling." Physics in Medicine and Biology. **36**. pp. 1259-1317 (1991).

251 J. A. Anderson, E. Rosenfield *Neurocomputing: Foundations of research.* (MIT Press, Cambridge, 1988).

252 J. A. Anderson, E. Rosenfield *Neurocomputing 2.* (MIT Press, Cambridge, 1990).

253 W. S. McCulloch, W. Pitts "A logical calculus of the ideas immanent in nervous activity." Biophysics Journal. **5**. pp. 115-137 (1943).

254 D. O. Hebb *The organization of behaviour: A neuropsychological theory.* (Wiley, New York, 1949).

255 F. Rosenblatt "The Perceptron: a probalistic model for information storage and organisation in the brain." Psychological Review. **65**. pp. 386-408 (1958).

256 F. Rosenblatt *Principles of Neurodynamics: Perceptrons and the theory of brain mechanisms.* (Spartan Books, Washington, DC, 1962).

257 D. E. Rumelhart, G. E. Hinton, R. J. Williams "Learning representations by back-propagating errors." Nature. **323**. pp. 533-536 (1986).

258 J. M. Boone, V. G. Sigillito, G. S. Shaber "Neural networks in radiology: An introduction and evaluation in a signal detection task." Medical Physics. **17**. pp. 234-241 (1990).

259 T. J. Farrell, M. S. Patterson, J. E. Hayward, B. C. Wilson, E. R. Beck "A CCD and neural network based instrument for the non-invasive determination of tissue optical properties in-vivo." Proceedings of SPIE. **2135**. pp. 117-128 (1992).

260 T. J. Farrell, B. C. Wilson, M. S. Patterson "The use of a neural network to determine tissue optical properties from spatially resolved diffuse reflectance measurements." Physics in Medicine and Biology. **37**. pp. 2281-2286 (1992).

261 A. Kienle, R. Steiner "Determination of the optical properties of tissue by spatially resolved transmission measurements and Monte Carlo simulations." Proceedings of SPIE. **2077**. pp. 142-152 (1993).

262 A. Kienle, R. Hibst, R. Steiner "The use of a neural network and Monte Carlo simulations to determine the optical coefficients with spatially resolved transmission measurements." Proceedings of SPIE. **2134**. (1994).

263 T. Masters *Practical neural network recipes in C++.* (Academic Press Inc, London, 1993).

264 W. H. Press, B. P. Flannery, S. A. Teukolsky, W. T. Vetterling *Numerical Recipes: The Art of Scientific Computing.* (Cambridge University Press, Cambridge UK, 1986).